

AUTONOMOUS VEHICLE CONTROL
AT THE LIMITS OF HANDLING

A DISSERTATION
SUBMITTED TO THE DEPARTMENT OF MECHANICAL
ENGINEERING
AND THE COMMITTEE ON GRADUATE STUDIES
OF STANFORD UNIVERSITY
IN PARTIAL FULFILLMENT OF THE REQUIREMENTS
FOR THE DEGREE OF
DOCTOR OF PHILOSOPHY

Krisada (Mick) Kritayakirana
June 2012

Abstract

Many road accidents are caused by the inability of drivers to control a vehicle at its friction limits, yet racecar drivers routinely operate a vehicle at the limits of handling without losing control. If autonomous vehicles or driver assistance systems had capabilities similar to those of racecar drivers, many fatal accidents could be avoided. To advance this goal, an autonomous racing controller was designed and tested to understand how to track a path at the friction limits.

The controller structure was inspired by how racecar drivers break down their task into (i) finding a desired path, and (ii) tracking this desired path at the limits. Separating the problem in this way instead of integrating both path planning and path tracking into one problem results in an intuitive structure that is easy to analyze. Assuming that a desired path is known, the racing controller in this dissertation focuses on tracking this path at the friction limits. The controller is separated into steering and longitudinal modules, each module consisting of feedforward and feedback controller submodules. From the desired path, the longitudinal feedforward submodule uses the path geometry and friction information derived from a “ g - g ” diagram to execute trail-braking and throttle-on-exit driving techniques. These techniques maximize tire forces during cornering by using a combination of steering and brake/throttle inputs. To calculate the steering input, the feedforward steering submodule employs a nonlinear bicycle model. These feedforward submodules can adjust their commands in real-time to respond to any changes in the environment, such as changes in friction due to rain or changes in the desired path to avoid an obstacle.

To add path tracking ability and stability to the system, a fixed-gain full-state steering feedback submodule was combined with a longitudinal feedback submodule

that regulates vehicle speed and minimizes tire slip through a slip circle feedback controller. For consistency in the steering controller, the same reference point at the center of percussion (COP) was used for both feedforward and feedback steering submodules. The COP was chosen because it simplifies the feedforward design process by eliminating the nonlinear and changing rear axle force from the lateral dynamics equation. Using the set of steering gains derived from lanekeeping steering with yaw damping feedback, the system was proven to be Lyapunov stable even when the rear tires are highly saturated.

The simulation and experimental results on various surfaces on oval tracks demonstrate that the submodules work collectively to robustly track a desired path at the friction limits. The experimental results highlight the challenges of trail-braking during a corner-entry phase, where a correct corner entry-speed and accurate model of longitudinal weight transfer are required. Thus, longitudinal weight transfer was incorporated into the feedforward longitudinal submodule to minimize oversteer caused by reduction in the rear normal load. In addition to performing well on oval tracks, the racing controller also showed its ability to operate in a challenging environment by driving 12.4 miles up Pikes Peak autonomously, where the path consists of both dirt and paved surfaces with significant bank and grade. The complex path at Pikes Peak also demonstrated the controller's ability to plan the vehicle speed several corners in advance.

The racing controller's ability to drive a vehicle at the friction limits can be applied to drive an autonomous vehicle while ensuring stability and tracking ability even in extreme conditions, such as driving on icy road. Alternatively, the submodules in the racing controller can be adapted to create driver assistance systems that work in conjunction with the driver, assisting the driver during emergency maneuvers.

Dedicated to my family, especially Cat, who took her leap of faith to join my PhD journey.

Acknowledgements

Looking back through my PhD, it has been a truly amazing intellectual journey. I came to Stanford without realizing how this journey would inspire my entrepreneurial spirit, which greatly impacts my personal development and career goals. The journey was full of challenges, and I owe great acknowledgement to many of you who helped me overcome these difficulties.

First and foremost, I would like to thank Chris for his guidance throughout my PhD. Not only did Chris provide excellent academic advice, but he also showed me how to be creative in doing research. He taught me how to push the research boundary while mitigating risks, how to start from a difficult challenge¹ and break it down to manageable steps, how to develop prototypes and how to handle failures. I greatly appreciated what Chris has taught me academically, but more importantly, he taught me how to be innovative and creative.

I would also like to thank the professors on my reading committee, Dr. Cole and Prof. Rock, who provided me with stimulating comments and challenging questions, which helped me think through my research. Dr. Cole was my academic advisor at Cambridge and has been my great mentor since. He encouraged me to apply to a PhD program and provided great guidance, such as recommending me to consider Stanford! I also greatly appreciate his willingness to travel all the way from Cambridge to attend my PhD defense at Stanford. Prof. Rock has been a great control guru and has been involved with my PhD research since my qualifying exam. He always provides me with thorough answers to my research questions and always ask questions that are

¹First time I heard about the idea of making an autonomous racing car driving up Pikes Peak, I thought Chris was joking and laughed...

challenging and interesting.

Chris said that a defense should be a great celebration to the end of a PhD journey, and I was lucky to have such a great defense committee. I was fortunate that Prof. Powell could be a part of my defense committee. I took my first control class with Prof. Powell, and it has laid a great foundation for me since. Although we are in a different department, Prof. Deierlein has helped both Cat and I since our early days at Stanford, from allowing me to use his shaker rig in my first year to becoming my PhD defense chair. I would also like to thank Prof. Okamura for showing her great interest in my research and participating in my defense.

I would also like to thank Fulbright Science and Technology for giving me this wonderful opportunity to do my PhD at Stanford. My Fulbright scholarship from the U.S. and Thai governments has allowed me to truly appreciate American culture and the entrepreneurial spirit of this nation. I also hope that I have been a decent ambassador for Thailand. Being awarded this Fulbright scholarship would not have been possible without encouragement and support from many of my professors at Chulalongkorn University, especially Ajarn Chinatep, Ajarn Asi, Ajarn Witaya, Ajarn Supavut, Ajarn Jirapong, Ajarn Tawan and Ajarn Nuksit.

Making Shelley (the autonomous Audi TTS) ran autonomously up Pikes Peak played an important part in my research. It was a challenging task that could not have been done without great partnerships with the Electronics Research Laboratory of Volkswagen of America (ERL) and the Oracle, and the great support from Audi of America, the Volkswagen Automotive Innovation Lab (VAIL) and OmniSTAR. Besides these great partnerships, I had the privilege to work with a great team in a very challenging environment. We had both ups and downs (literally and figuratively), but we always pulled through. Waking up at four in the morning to work in a high altitude environment was harsh, but needless to say, when Shelley made it to the top of Pikes Peak by herself, it was quite a memorable experience (Fig. 1). Without their assistance, my research could not come this far. My thanks go to Burkhard Huhnke, Bernhard Müller-Beßler, Marcial Hernandez, Rob Simpson, Robert MacLellan, Dirk Langer, Pablo Marx, Mike Duigou, Ivan Tarasov and David Hoffert, and my special thanks to Gany Stanek and Felix Weidner who gave me tremendous help interfacing



Figure 1: September 9, 2010, first successful autonomous run up Pikes Peak, Colorado (the author was the photographer)

between my controller and Shelley.

Testing has been an integral part of this project and we have been fortunate to receive great support from many venues across the country, such as Pikes Peak International Hill Climb, City of Colorado Springs - Colorado, the Bureau of Land Management - Salt Lake District, the Santa Clara County Fairgrounds, the City of Mountain View - California, SLAC National Accelerator Laboratory, Stanford University Parking & Transportation Services, Thunderhill Raceway Park, Infineon Raceway and Mazda Raceway Laguna Seca.

Although four and a half years in graduate school may sound long, I was lucky to enjoy spending my time hanging out and discussing (random topics) with the incredibly fun and intellectual people in the Dynamic Design Lab (DDL). I spent my time traveling with many people in the DDL, including Rami and Paul, who I shared rooms with all across the U.S. and Europe. In addition to students in the DDL, I would like to thank Jennifer, Adele and Denise for their tremendous help with my purchasing and traveling. Furthermore, many DDL members gave me valuable

comments to improve my writing, especially Kirstin, Guido, Joe and Nitin, who spent a great amount of time reading my dissertation and papers. Besides DDL members, I also owe Claude and Mary for their comments and feedbacks on my writing techniques.

Initially, I was concerned if I would have a chance to enjoy automotive activities outside of my research at DDL. Luckily, Stanford has been building up a very nice automotive environment, especially when Sven came to Stanford to help form the Center of Automotive Research at Stanford (CARS). Furthermore, I had a great time doing track and drift days with Josh (who was kind enough to let me borrow his pink Miata), Shad, Joe and Jackie. Without these activities to relax myself, I would not be able to last throughout my PhD career. Besides my car activities, both Cat and I appreciated the time we spent eating, hanging out, playing soccer and traveling with the Thai community at Stanford.

Like many others who came to Stanford, I was bit by a startup bug. Thanks to the Entrepreneurial Design for Extreme Affordability teaching team: Prof. Patell, Stuart and Erica, who sparked my interest in becoming a social entrepreneur in the future. I had a great time working on Safi, a spinoff project from Extreme class that focuses on an affordable hand sanitizer, and learned a tremendous amount from my co-founders Kate (who's business knowledge I greatly appreciate), Nathalie and Ken. I hope that sometime in my future, I will apply my technical knowledge to solve a social issue in Thailand.

Finally, I would like to thank my family and my host family, who have been great support and always encourage me. Thank you dad for always keep asking me when I will finish, my mom for always giving me positive nudges, and my brother and my sister who always check-in to see how Cat and I are doing. Last but not least, I owe a lot to Cat, who decided to leave her stable life to join my PhD journey, where we began our family life in the U.S. I know how much she hates changes, and yet, she decided to take her leap of faith to join my PhD journey. I greatly appreciated her support and for standing by my side no matter what the situation. Thank you, Cat.

Contents

Abstract	v
Acknowledgements	viii
1 Introduction	1
1.1 Motivation	1
1.2 State of the art	3
1.2.1 Racecar driver approach	3
1.2.2 Vehicle control	5
1.2.3 Autonomous vehicles in practice	12
1.3 Dissertation contributions and outline	13
1.3.1 A modular controller framework inspired by racecar driver behavior	14
1.3.2 Experimental results on an autonomous racing vehicle	15
1.3.3 Analytical controller design using the center of percussion	15
2 Driver and Controller Structure	17
2.1 Racecar drivers	17
2.1.1 Cornering sequences	18
2.1.2 Understanding vehicle limits on a “ <i>g-g</i> ” diagram	18
2.1.3 Driving at the limits	20
2.2 A controller architecture for racing	21
2.3 Path information	22
2.3.1 Path description (racing line)	22

2.3.2	Friction estimation	25
2.4	Speed profile	25
2.4.1	Constant radius	27
2.4.2	Clothoid entry	27
2.4.3	Straight	28
2.4.4	Clothoid exit	29
2.4.5	Effect of longitudinal weight transfer, bank and grade	31
2.5	Path tracking at the limits	32
2.5.1	Steering controller	33
2.5.2	Longitudinal controller	33
3	Basic Lateral Controller	34
3.1	Feedforward steering controller	35
3.2	Feedback steering controller	39
3.2.1	Lanekeeping	39
3.2.2	Lanekeeping stability	42
3.2.3	Yaw damping	42
4	Longitudinal Controller	44
4.1	Feedforward longitudinal controller	44
4.1.1	Feedforward acceleration	45
4.1.2	Drag compensation	45
4.2	Slip circle feedback controller	46
4.2.1	Slip circle concept	47
4.2.2	Implementing the slip circle controller	49
4.3	Tracking of desired speed profile	52
4.3.1	Complex map	52
4.3.2	Speed feedback	54
4.4	Total longitudinal force	54
5	Experimental Results	55
5.1	Experimental setup	56

5.2	Experimental results on a dirt surface	56
5.2.1	“ <i>g-g</i> ” diagram on a dirt surface	63
5.3	Experimental results on a salt surface	64
5.3.1	Overall controller performance	64
5.3.2	Performance with over-estimated friction	70
5.3.3	Effect of no-slip gain k_{noSlip}	75
5.3.4	Effectiveness of yaw damping	75
5.4	Experimental results on a paved surface	77
5.4.1	Tracking the desired speed	84
5.5	Pikes Peak	85
5.6	Conclusions	86
6	Integrated Steering Controller	88
6.1	Integrated steering controller	89
6.1.1	Center of percussion	91
6.1.2	Feedforward steering controller	93
6.1.3	Feedback steering controller	94
6.1.4	Converting front lateral force to steering input	99
6.1.5	Stability at the limits	100
6.2	Simulation results	103
6.2.1	Friction sensitivity	104
6.2.2	The importance of weight transfer	107
6.3	Experimental results	107
6.3.1	Comparison with simulation results	110
6.4	Steering gain analysis	113
6.4.1	Choosing gains for Lyapunov stability	113
6.4.2	Output feedback linearization	117
6.4.3	Linear Quadratic Regulator (LQR)	120
6.5	Conclusions	126
7	Conclusions and Future Work	130

A Weight Transfer	134
A.1 Effect of longitudinal weight transfer	134
A.1.1 Brake proportioning (\tilde{f})	138
A.2 Effect of grade	139
A.2.1 Shifting “ $g-g$ ” diagram	140
A.2.2 Reduction in normal load	142
A.3 Effect of bank	142
A.3.1 Effect of bank on lateral forces	142
A.3.2 Effect of bank on normal load	144
A.4 Calculating longitudinal acceleration	145
A.4.1 Calculating a_x for straight section	145
A.4.2 Calculating a_x for corner entry section	146
A.4.3 Calculating a_x for constant radius section	147
A.4.4 Calculating a_x for clothoid-exit section	148
B Autonomous Audi TTS (Shelley)	151
B.1 Steering system	152
B.1.1 Steering system dynamics	152
B.1.2 Low-level feedforward steering controller	154
B.1.3 Frequency response of the steering system	155
B.1.4 Low-level feedback steering controller	157
B.2 Throttle system	158
B.3 Brake system	159
B.4 Gear shift system	159
B.5 xPC target, a.k.a. “Peak Box”	159
C Future Work	160
C.1 Real-time friction estimation	160
C.2 Force to delta	161
C.3 Path modification	162

D Driving P1 at the limits	165
D.1 Preliminary work on P1	165
D.1.1 Speed controller	166
D.1.2 Experimental setup	167
D.1.3 Experimental results	168
D.1.4 Conclusions for section D.1	175
D.2 Feedforward longitudinal control	176
D.2.1 Longitudinal feedback algorithm	177
D.2.2 Experimental results	177
D.2.3 Conclusion for section D.2	182
Bibliography	183

List of Tables

5.1	Controller gains and parameters for dirt surface	58
5.2	Controller gains and parameters for Bonneville Salt Flats	66
5.3	Controller gains and parameters for paved surface	79
6.1	Controller gains and parameters based on the controller in Chapter 3	99
6.2	Friction sensitivity	106
6.3	LQR scaling factors and the result gains	109
B.1	Shelley's parameters	151
D.1	Summary of each controller's tracking performance	175
D.2	Demonstrating feedforward longitudinal controller performance	178

List of Figures

1	September 9, 2010, first successful autonomous run up Pikes Peak, Colorado (the author was the photographer)	x
1.1	While an average driver may lose control of a vehicle on an icy road, a racecar driver can negotiate a turn at the friction limits without losing control (courtesy of www.audiusanews.com)	2
1.2	Autonomous Audi TTS (courtesy of www.audiusanews.com)	3
1.3	Layout of prior art in vehicle control	5
2.1	Driving at the limits	19
2.2	Overall controller structure	22
2.3	Clothoid map: showing (a) shape and (b) curvature	23
2.4	Clothoid map fits to a racecar driver's racing line (courtesy to Paul Theodosis)	24
2.5	Speed and acceleration profiles using parameters from Table 5.3 and B.1: showing (a) type of segment (b) speed profile (c) longitudinal acceleration profile and (d) lateral acceleration profile	30
2.6	Effect of longitudinal weight transfer on maximum achievable acceleration, $\mu = 0.7$ (using parameters from Table 5.3 and B.1)	31
2.7	Overall controller block diagram	32
3.1	Basic steering controller: consisting of feedforward steering, lanekeeping feedback steering and yaw damping feedback steering.	35
3.2	Planar bicycle model	36

3.3	Example of feedforward steering from a handling diagram, using ramp steer $U_x = 15 \text{ m/s}$	38
3.4	Lanekeeping system	40
4.1	An overview of the longitudinal controller	45
4.2	Relationship between tire curves and a slip circle	47
4.3	Different control scenarios on a slip circle, when $\alpha_{ref} = \alpha_{peak}$	49
4.4	A small section of Pikes Peak map, around “ski area”. Note that a long left-sweep is followed immediately by a tight right-hand turn.	53
4.5	The corresponding speed profile for the small section of Pikes Peak map in Fig 4.4 (0=straight, 1=corner entry, 2=constant radius and 3=corner exit).	53
5.1	Autonomous Audi TTS on a dirt surface at Santa Clara County Fairgrounds, Santa Clara, CA	57
5.2	Front (a) and rear (b) tire curves fitted to the ramp steer data, on a dirt surface	59
5.3	Comparison of three tire curves from different testing surfaces	59
5.4	Map used on a dirt surface, plotting on North and East coordinates	60
5.5	Controller commands (a-b) and vehicle states (c-h) on dirt surface, with no-slip gain. Feedback force in Figure b only shows slip circle controller command.	61
5.6	“ $g-g$ ” diagram from Audi TTS on dirt surface	63
5.7	Autonomous Audi TTS at Bonneville Salt Flats, Utah	65
5.8	Map used on a salt surface, plotting on North and East coordinates	65
5.9	Front (a) and rear (b) tire curves fitted to the ramp steer data, on a salt surface	67
5.10	Controller commands (a-b) and vehicle states (c-h) on salt surface, with zero no-slip gain. Feedback force in Figure b only shows slip circle controller command.	68
5.11	“ $g-g$ ” diagram from Audi TTS on salt surface, with zero no-slip gain k_{noSlip}	70

5.12 Controller commands (a-b) and vehicle states (c-h) on salt surface when the actual friction is less than the predicted value, with zero no-slip gain. Feedback force in Figure b only shows slip circle controller command.	71
5.13 “ <i>g-g</i> ” diagram from Audi TTS on salt surface, when over the limits. Note that no-slip gain k_{noSlip} is set to zero	72
5.14 Front (a) and rear (b) combined slip on salt surface when over the limits. Note that no-slip gain k_{noSlip} is set to zero	73
5.15 Controller commands (a-b) and vehicle states (c-h) on salt surface. Without yaw damping and with no-slip gain, at north corner in Fig. 5.8	76
5.16 Map used on a paved surface with gravel on top, plotting on North and East coordinates. Note that the map has very short constant radius sections	78
5.17 Front (a) and rear (b) tire curves fitted to the ramp steer data, on a paved surface with gravel on top	78
5.18 Controller commands (a-b) and vehicle states (c-h) on paved surface, with zero no-slip gain. Feedback force in Figure b only shows slip circle controller command.	80
5.19 Controller commands (a-b) and vehicle states (c-h) on paved surface when the friction value is over-estimated, with zero no-slip gain. Feedback force in Figure b only shows slip circle controller command.	81
5.20 “ <i>g-g</i> ” diagram from Audi TTS on paved surface, with zero no-slip gain	82
5.21 Poor speed tracking on paved surface, with zero no-slip gain	83
5.22 Effects of the corner entry speed, using a point mass model	83
5.23 Improved speed tracking on paved surface, with zero no-slip gain . . .	84
5.24 “ <i>g-g</i> ” diagram from Audi TTS on paved surface, after tuning speed gain	85
5.25 Pikes Peak International Hill Climb Course Map [30]	86
6.1 Lateral tracking parameters	90
6.2 Effect of rear tire force at the center of percussion, superimposing rotational and translational effects	93

6.3	Rear tire curve, showing the effect of η_r	95
6.4	Monotonically decreasing η_r function	95
6.5	Modified tire curve used in (6.19)	100
6.6	Map used in the simulation and the experimental results in Section 6.3.1, plotting on North and East coordinates	103
6.7	Vehicle's state variables from the simulation	104
6.8	Vehicle's slips from the simulation	105
6.9	Controller's inputs from the simulation	105
6.10	" $g-g$ " diagram from the simulation	106
6.11	Comparison of vehicle states between with and without longitudinal weight transfer, (a-b) large errors when not taking weight transfer into account (c-e) vehicle states	108
6.12	Comparison of slip between with and without longitudinal weight trans- fer; large oversteering occurs when the controller does not take the weight transfer into account	108
6.13	Steering controller command (a) road wheel angle (b) feedback com- mands from different states (c) lateral slip	110
6.14	Comparison of vehicle states between simulation and experimental results	111
6.15	Comparison of slip between simulation and experimental results . .	111
6.16	Comparison of inputs between simulation and experimental results .	112
6.17	Comparison of " $g-g$ " diagrams between simulation and experimental results	113
6.18	Showing the value of $z(k_2, k_4)$ in (6.34), (a) varies vehicle speed U_x (b) varies η_r	118
6.19	Showing tracking performance when using output feedback linearization	120
6.20	Controller commands (a-b) and vehicle states (c-h) when using output feedback linearization	121
6.21	Steering controller command using output feedback linearization (a) road wheel angle (b) feedback commands from different states (c) ve- hicle states	122

6.22 Controller commands (a-b) and vehicle states (c-h) using gain set 1: LQR	124
6.23 “ <i>g-g</i> ” diagram using gain set 1: LQR	125
6.24 Steering controller command using gain set 1: LQR (a) road wheel angle (b) feedback commands from different states	126
6.25 Controller commands (a-b) and vehicle states (c-h) using gain set 3: improve e_{cop}	127
6.26 “ <i>g-g</i> ” diagram using gain set 3: improve e_{cop}	128
6.27 Steering controller command using gain set 3: improve e_{cop} (a) road wheel angle (b) feedback commands from different states	128
A.1 Weight transfer during braking, \hat{x} and \hat{y} represent vehicle body-fixed coordinate (figure of Audi TTS, courtesy of www.audiusanews.com)	135
A.2 Effect of longitudinal weight transfer on maximum acceleration, using $\mu = 0.7$ and vehicle parameters from Table B.1, assuming no accelera- tion limitation from engine torque	139
A.3 Effect of grade (figure of Audi TTS, courtesy of www.audiusanews.com)	140
A.4 Effect of grade on a “ <i>g-g</i> ” diagram	141
A.5 Effect of bank, vehicle is turning left (figure of Audi TTS, courtesy of www.audiusanews.com)	143
B.1 Identifying jacking torque in the steering system	153
B.2 Time history of the steering torque input and the hand wheel output, using a chirp input	155
B.3 Frequency response from the steering system identification, using chirp input. The handwheel output was shifted 20 ms forward to compensate for communication delay	156
B.4 Steering plots, showing a) tracking performance b) steering torque input T , steering torque feedback T_{FB} , jacking torque compensation $T_{jacking}$ and aligning moment compensation T_{align}	158
D.1 Stanford P1 by-wire research vehicle	165

D.2	Vehicle trajectory: with feedback steering only	168
D.3	Vehicle trajectory: with completed steering control and feedforward speed	169
D.4	Front tire slip angle: with completed steering control and feedforward speed	170
D.5	vehicle trajectory: adding lookahead error speed feedback	171
D.6	“ <i>g-g</i> ” diagram: adding lookahead error speed feedback	171
D.7	Front tire slip angle: adding lookahead error speed feedback	172
D.8	Vehicle trajectory: adding heading error speed feedback	173
D.9	“ <i>g-g</i> ” diagram: adding heading error speed feedback	174
D.10	Front tire slip angle: adding heading error speed feedback	174
D.11	“ <i>g-g</i> ” diagram: without trail-braking and throttle-on-exit	177
D.12	“ <i>g-g</i> ” diagram: with trail-braking and throttle-on-exit	178
D.13	Plots of input commands and vehicle states	180

Chapter 1

Introduction

1.1 Motivation

With an estimated of one billion automobiles around the world [31], the automobile has become a part of many lives. Yet, many lives are lost in vehicle accidents. In the United States alone, the National Highway Traffic Safety Administration (NHTSA) reports that 5 million crashes occurred in 2009 [59], causing over 30,000 deaths and 2 million injuries. With a growing number of cars, better vehicle safety is needed to reduce these fatalities.

Many vehicle technologies, including driver assistance systems, have greatly improved vehicle safety. Technologies such as Anti-lock Braking System (ABS) and Electronic Stability Program (ESP) reduce vehicle accidents by providing assistance to the drivers during emergency maneuvers. Dang [11] demonstrated in a NHTSA report that ESP can reduce fatal run-off-road crashes by as much as 36 percent for passenger cars. Nevertheless, these types of systems do not take any path information into account and focus only on vehicle stabilization. With technology advancement in Global Positioning System (GPS), mapping and by-wire technologies, future driver assistance systems can utilize path information to provide proper control actuation. These new technologies open up an opportunity to rethink the future of driver assistance system.

Historically, race cars have provided the inspiration for many developments in



Figure 1.1: While an average driver may lose control of a vehicle on an icy road, a racecar driver can negotiate a turn at the friction limits without losing control (courtesy of www.audiusanews.com)

production vehicles. With the ability to fully access vehicle’s actuators (steering, throttle, brake, etc.), racecar drivers now provide a similar inspiration for the design of vehicle safety systems. Racecar drivers can drive a vehicle along a given path while utilizing the friction limits without losing control, while average drivers may loss control of a vehicle when the tires reach their limits. Thus, this inspiration from racecar drivers was used to rethink the future of driver assistance systems.

Inspired by racecar drivers, the goal of the autonomous vehicle controller presented in this dissertation was to capture their ability to maximize the tire forces while tracking a path. The knowledge gained from driving a path autonomously at the friction limits can be extended to driver assistance systems, where the system can assist average drivers to fully utilize the tire forces to avoid obstacles or avoid losing control on icy road, such as in the situation shown in Fig. 1.1. To advance this goal, an autonomous Audi TTS (Fig. 1.2) was built, where the project is a collaboration between Volkswagen Electronics Research Laboratory, Oracle and the Dynamic Design Lab at Stanford University.

In addition to driver assistance application, a racing controller that can drive a vehicle at the limits of handling has direct application to autonomous vehicles. The



Figure 1.2: Autonomous Audi TTS (courtesy of www.audiusanews.com)

“virtual racecar” driver, which has a full understanding of friction limits, can drive a vehicle safely on different surfaces, such as a snowy and an icy road. The ability to drive a vehicle autonomously and safely in both normal and extreme conditions is crucial for the public acceptance of autonomous vehicles.

1.2 State of the art

Before discussing the state of the art in vehicle control, the following section explains the inspiration of this dissertation: racecar drivers.

1.2.1 Racecar driver approach

The inspiration of the autonomous racing controller in this dissertation came from learning how racecar drivers control a vehicle at its friction limits. Books written by racecar drivers give insights into driving at the limits and provide inspirations

for the design of the racing controller [78, 3, 45, 71]. One of the design challenges is to translate what racecar drivers described in these books into equations that can be implemented into the racing controller. Some authors have more technical background, and based their explanations on their engineering knowledge [78, 71], which often facilitate the controller design process. For instance, Piero Taruffi, an Italian Formula 1 grand prix winner with a doctorate degree in engineering, wrote a book “The Technique of Motor Racing” [78] that gives engineering insights into his driving approach and mathematical analysis of his racing line. Although, a large number of explanation in these racing books is still based on drivers intuition without much scientific explanation, they share some common concepts that were applied into the autonomous racing controller as follows.

The first concept derived from racecar drivers is based on how they breakdown their driving tasks into generating a line that they want to follow (a racing line) and controlling a vehicle at the friction limits [78, 3, 45]. This concept provides a structure for the autonomous racing controller described in this dissertation. The second concept derived from racecar drivers is how they use various driving techniques to fully utilize the tire forces. For instance, racecar drivers use a combination of steering and brake while entering a corner, which is called trail-braking, and use a combination of steering and throttle while exiting a corner, which is called throttle-on-exit [3, 45]. These driving techniques are incorporated into the racing controller by applying the following concept.

To quantify if racecar drivers fully utilize the tire forces, a “ $g-g$ ” diagram introduced by Rice [64, 49] is often used. This “ $g-g$ ” diagram is a plot of vehicle longitudinal and lateral acceleration, and since the friction force from the tires limits the maximum vehicle acceleration, a boundary is formed on a “ $g-g$ ” diagram. Thus, the goal of racecar drivers is to follow the path while ensuring that the vehicle acceleration trace the friction boundary on a “ $g-g$ ” diagram. Lopez [45] gave a good overview of how racecar drivers coordinate their steering, throttle and brake input to achieve this goal, while a more mathematical analysis of driving at the friction limit on a “ $g-g$ ” diagram can be found from Mitchell et al. [53, 52] and Zapletal [97]. This concept of driving at the friction limits motivates the controller design, where a “ $g-g$ ”

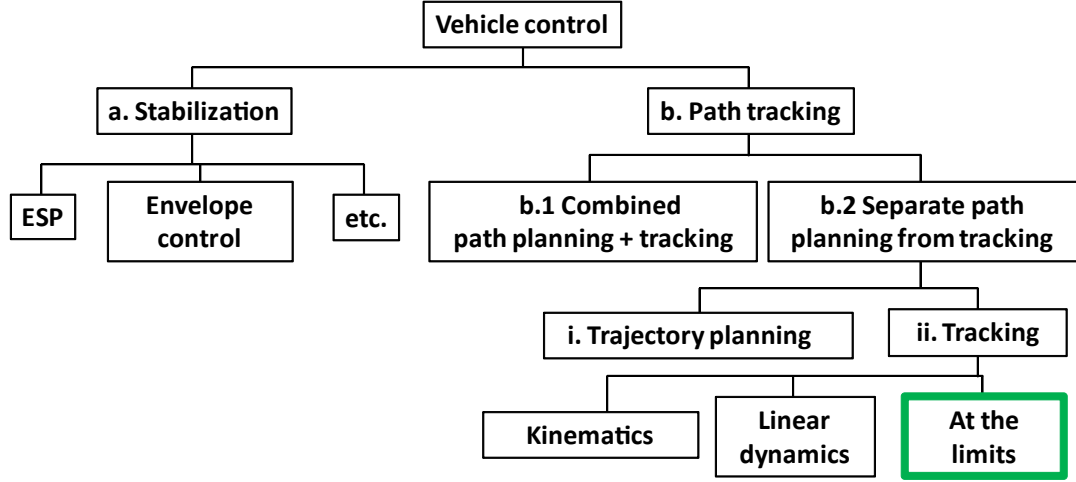


Figure 1.3: Layout of prior art in vehicle control

diagram was used.

1.2.2 Vehicle control

Figure 1.3 provides an overview of the state of the art in vehicle control, both in production and in research. They are grouped into various categories according to their objectives (Fig. 1.3). At the top level, the vehicle control methods are separated into vehicle stabilization and path tracking. Vehicle stabilization category includes many production controllers that do not take any path information into account. On the other hand, only a few production controllers exist in path tracking category, while most of the path tracking controllers are in research phase, especially path tracking at the limits of handling. The following sections discuss some prominent production technologies and selected research relevant to the design of the autonomous racing controller.

a. Vehicle stabilization

The first category represents vehicle stabilization that does not take any path information into account. Some of the prominent production systems in this category

are Electronic Stability Program (ESP), Anti-Lock Brake System (ABS) and traction control system. The ESP stabilizes a vehicle via controlling vehicle yaw motion through individual wheel braking. The detailed explanation of how ESP operates can be found from van Zanten et al. [89, 88]. The ABS and traction control system stabilize the vehicle by preventing all tires from having excessive slide. This concept is similar to racecar drivers trying to maximize tire forces without exceeding the friction limits [48]. Although ESP, ABS and traction control system only focus on controlling longitudinal inputs through throttle and brake, unlike racecar drivers who coordinate steering, throttle and brake to maximize tire forces.

Besides existing technologies in production vehicles, there are many research activities in vehicle stabilization because most of the required sensors and actuators are either in production or close to production ready. For instance, from measured yaw rate and side slip, Bobier and Gerdes [5] employed a sliding surface technique to design an envelope control, which ensures that the vehicle will operate within a defined safe envelope through assisting steering input. Alternatively, the concept of a friction limit circle on a “ $g-g$ ” diagram can be extended to design a longitudinal feedback controller for a driver assistance system. Takahashi et al. [75] and Yamakado et al. [96] introduced a “g-vectoring” concept that uses the measured jerks (derivative of accelerations) to calculate assisting braking input that stabilizes a vehicle during cornering by reducing vehicle speed.

b. Path tracking

Advancement in Global Positioning System (GPS), vision system (cameras) and remote sensing system [Light Detection And Ranging (LIDAR) and Laser Detection and Ranging (LADAR)] opens up many opportunities for including path information into controllers. The controllers can utilize this path information to track a desired path as well as stabilize the vehicle. Although a small number of production vehicles have lanekeeping systems that use path information [36], most of the works in this field are still in a research phase. With path information, there are two general approaches to incorporate this information into controllers. The first approach uses an

optimization method to compute both path planning and path tracking simultaneously (b.1 in Fig. 1.3). Alternatively, the task of designing a path can be separated from the path tracking task, which is the approach that most autonomous vehicles use (b.2 in Fig. 1.3).

b.1 Combined path planning and tracking

The first approach in path tracking combines both path generation (a racing line) and vehicle control inputs into one optimization problem. This approach is often employed in a racing application when the objective is to achieve a minimum time around a track. For instance, Gerdts et al. [16] used an optimal control technique to find a racing line that uses a minimum time around a paved track, while Velenis et al. [90] employed a similar technique to describe high side slip maneuvers that minimize time around a corner on a low friction surface. Other optimization methods include using a Model Predictive Control (MPC) to calculate a minimum maneuver time as proposed by Timings and Cole [84, 85], or using sequential quadratic programming (SQP) to find an optimal racing line as proposed by Prokop [63] and Casanova et al. [9]. Since these optimized solutions highly coupled both path and control input, gaining a physical intuition from the results can be difficult. Furthermore, running these optimization methods in real-time can be challenging due to limited computer processing power. Nevertheless, there are merits in these optimization methods because they resemble racecar drivers adjusting their racing line and driving inputs to optimize their lap time.

b.2 Separate path planning and tracking

Besides using an optimization methods, another vehicle control approach is to separate trajectory planning out from tracking a path at the friction limits. This approach is similar to racecar drivers separating their driving tasks into generating a racing line and tracking a path at the friction limits [45, 3, 78]. An overview of the methods used for generating a trajectory are discussed first, then different methods of tracking a desired trajectory are discussed.

i. Trajectory planning

Depending on the design objective, there are multiple techniques to plan a trajectory. Two different methods are discussed in this section. The first method, which is more oriented toward the field of vehicle dynamics, focuses on finding a path that provides a minimum time around a track, i.e. finding a racing line. The second method, which is more oriented toward the field of robotics, focuses on path planning based on environment perception.

In vehicle dynamics field, an optimization technique can be used to find a racing line, albeit without computing vehicle control inputs. For instance, Braghin [6] found a racing line by optimizing between minimizing traveled distance and maximizing traveling speed. Other methods of finding a racing line include using a genetic algorithm, where the algorithm explores different racing lines to search for the line that provides the fastest time [57, 15, 8]. In addition, the Dynamic Design Lab at Stanford University is working on finding an optimal racing line by using a gradient descent method, and the paths utilized in this dissertation were designed using the technique proposed by Theodosis and Gerdès [79].

In robotics field, trajectory planning generally concentrates on environment perception, artificial intelligence and machine learning without taking vehicle dynamics into consideration. From various sensor measurements, the algorithm decides which path to take and which maneuver to execute. This area has been one of the main focuses of autonomous vehicles research for more than 25 years. For instance, Goto and Stentz [19], and Wang et al. [95] at NavLab conducted an extensive research on understanding the environment, sensor fusion and Bayesian formulation since 1987. Similarly, the path planning and controlling systems of an autonomous Mercedes Benz S-class built by Maurer and Dickmanns [47, 46, 12] proved that the vehicle could run autonomously on a German Autobahn at 180km/h in 1995. This ability to properly plan a trajectory according to the environment is crucial for autonomous vehicles. Nevertheless, to fully realize the goal of autonomous vehicles, these technologies of trajectory planning based on environment have to merge with the vehicle control technology in order to provide autonomous vehicles that can operate safely even at the friction limits.

ii. Tracking

From a given path, there are several methods of tracking the desired path, ranging from a slow speed maneuver to a limits handling maneuver, which is the focus of this dissertation. At slow speed, vehicle kinematics or linear dynamics are often used, while a more complicated model that often includes a nonlinear tire model is required for a limit handling maneuver.

Kinematics

A feedforward steering based on vehicle kinematics can be used to track a desired path at slow speed. For instance, Shin et al. [69] used the vehicle geometry and the center of the rear axle as a reference point to design a feedforward steering input for robot vehicles. This kinematic approach also works for an autonomous parking system such as one demonstrated by Jeevan et al. [39] on Volkswagen autonomous valet parking project. However, when tracking a path at the limits, the vehicle will start to slide and the no-slip assumption used in this kinematic approach is no longer valid.

Linear dynamics

Besides using vehicle kinematics to calculate the feedforward steering input, a vehicle model with a linear or nonlinear tire model can be used in the algorithm. In general, a linear tire model is often used for simplicity, although the performance at the friction limits degrades as the nonlinearity in the tires have not been taken into account. Yet, the tracking performance from using a linear tire with steering feedback is still respectable as demonstrated by Müller-Bessler et al. [56, 58], who used a linear plant inversion method to calculate the feedforward steering input for the double-lane change maneuver on an autonomous Golf “53+1”.

Some steering feedback controller designs also utilize a linear tire model. For instance, Thommyppillai et al. [80, 81] and Sharp et al. [68] used a linear tire model to design an optimal linear preview control, to create a “virtual” racecar driver that tracks predefined paths on a flat surface. Although this optimal approach performs well in simulation, implementing this optimal controller in real-time application could pose some challenges due to the required computation time.

For testing in experimental vehicles, simpler approaches based on linear control

theory are often used for steering feedback. For example, the initial design of the steering controller in this dissertation was inspired by Rossetter's lanekeeping system [65], which is a simple proportional controller based on a lookahead error. Rossetter utilized a virtual potential field to derive this lanekeeping system and employed a Lyapunov theory to prove the stability of this linear system. This lanekeeping system was test successfully on a steer-by-wire Corvette [74]. Tseng et al. [86] also designed a lanekeeping steering systems based on a lookahead error. However, Tseng's lanekeeping system projects the lookahead error onto the actual path; thus, incorporating future path information into the feedback signal. This approach is different from Rossetter's lanekeeping system, which does not use any future path information. Thus, with the controller structure that separates the feedforward and feedback steering controllers such as one proposed in this dissertation, the lanekeeping system based on Rossetter's work was initially employed to avoid any interaction between the feedforward and feedback controllers.

Other steering controllers based on linear control theory include a fixed-gain full-state feedback controller. Similar to another steering controller that was explored in this dissertation, Guldner et al. [22, 21] employed front and rear lateral errors to design a fixed-gain full-state feedback steering controller for a vehicle used in an automated highway system [California Partners for Advanced Transportation Technology (PATH) program, see Section 1.2.3]. Another approach that Hingwe and Tomizuka [25] and Pham et al. [62] investigated in the PATH program is to utilize a sliding mode control to design a steering controller. This sliding mode controller mitigates the effect of modeling error from using a linear tire model, although care must be taken to minimize chatter in the steering system.

At the limits

When controlling a vehicle at the friction limits, including the tire nonlinearity can improve the controller performance. Various techniques that include tire nonlinearity into account are discussed in this section, ranging from using prerecorded data to incorporating a nonlinear tire model into the controller design.

The BMW TrackTrainer¹ is one of the autonomous vehicles that focus on driving

¹Only the controller aspect of the BMW TrackTrainer is discussed in this section, the detailed

at the friction limits [93]. Its implemented controller uses prerecorded data from a human driver, while the feedback steering controller uses a dynamic programming method. The longitudinal speed feedback also tracks the prerecorded speed profile by employing a proportional and derivative controller. Although prerecorded data already takes the effect of tire nonlinearity into account, this approach limits the flexibility in path modification and the ability to cope with changes in the environment. This limitation does not exist in other controllers that calculate the desired path and speed profile in real-time.

Besides using prerecorded data, Falcone et al. [13] captured the tire nonlinearity in their Model Predictive Control (MPC) algorithm and test their algorithm in an autonomous double-lane change maneuver. Although the nonlinearity was taken into account, the controller mainly focuses on operation in the linear region and tries to prevent the vehicle from getting close to the friction limits. Gordon et al. [18] utilized a different controller approach called vector fields analysis. At each point along the track, a vector field that constrains the motion of the vehicle is found from the available tire forces; thus, creating reference information for the controller to track. This technique facilitates the analysis of stability and robustness, albeit with heavily mathematical analysis that may not represent how human behaves. Another controller design approach that takes tire nonlinearity into account is to use a differential flatness technique. Peters et al. [61] utilized a differential flatness technique to simplify a nonlinear vehicle model into a point mass model at the vehicle center of percussion (COP) with yaw dynamics. Using the COP as a reference point to reduce the model complexity was also employed in this dissertation, albeit with different approach from what Peters et al. proposed.

Although Rossetter's lanekeeping steering is based on a linear tire model, it inspired the steering controller design in this dissertation because it has proven stability up to the friction limits. Switkes [73] extended Rossetter's work to include a nonlinear tire model in order to conduct the stability analysis at the friction limits. With Switkes' method, the system is proven to be Lyapunov stable as long as the tires are operating within 90% of their operating range. Talvala et al. [76, 77] introduced a

explanation of the BMW TrackTrainer will be discussed in Section 1.2.3.

variable to capture tire nonlinearity and proved that Rossetter's lanekeeping system is asymptotically stable, even when the tires are saturated beyond 90% of their operating range. Consequently, Rossetter's lanekeeping system was used as an inspiration for the initial steering controller design in this dissertation.

1.2.3 Autonomous vehicles in practice

This section provides a historic overview of existing autonomous vehicles in various fields, ranging from vehicle dynamics field that focuses on handling at the limits and tracking a path on an automated highway system, to robotic field that focuses on environment perception and decision.

Various Original Equipment Manufacturers (OEM) built autonomous vehicles that drive at the handling limits for different purposes. Volkswagen built Golf "53+1" from a production Golf GTI for performing a comparison test [56, 58]. The "53+1" can investigate how different tires perform on the same vehicle, given the same double-lane change maneuver at a constant speed. Similar to the Audi TTS in Fig. 1.2, the controller on the "53+1" has full access to steering, throttle and brake actuation. However, unlike the Audi TTS, both Anti-lock Braking System (ABS) and Electronic Stability Program (ESP) were used during testing. BMW also built the TrackTrainer to teach novice drivers how to drive at the friction limits [93]. With this goal in mind, the TrackTrainer controller relies more on prerecorded data from racecar drivers. The BMW TrackTrainer is driven manually around a track by a racecar driver and the data of the racing line and the speed profile are recorded for using as reference information for the controller. Then a novice driver sits in the driver seat while a vehicle is driving autonomously around a track, so that the novice driver can study the racing line.

Besides autonomous vehicles at the limits of handling, many control algorithms described in Section 1.2.2 were developed for vehicles used in automated highway system. The National Automated Highway System Consortium (NAHSC) [38] partnered with the California Partners for Advanced Transportation Technology (PATH) [37] to study the feasibility of having vehicles autonomously platoon on a dedicated highway lane to improve traffic efficiency. Besides scientific contribution, this PATH program

made a historic milestone in 1997 when the project successfully gave an automated highway system demo on the Interstate-15 in San Diego [10].

Although the autonomous vehicles mentioned above may sound relatively recent, work in autonomous vehicles has been an active research in robotic field for a certain period of time. Although most of the research activity in robotic field is oriented toward path planning as discussed in previous section. NavLab at Carnegie Mellon University is one of the pioneers in this field and has been working on autonomous vehicles since 1987 [19, 95]. Since then, the implementation and realization of path planning technology has progressed significantly, from being able to sense road boundaries to the ability to respond to traffic signs and pedestrians. The robustness of the path planning technology was put to the test when the Defense Advanced Research Projects Agency (DARPA) organized the DARPA Grand Challenge (in 2004 and 2005) and the DARPA Urban Challenge (in 2007) [27, 28, 29]. The 2005 DARPA Grand Challenge was won by “Stanley” [83], which is an autonomous vehicle from Stanford University, after it drove autonomously on a 212 km off-road course. Another autonomous vehicle from Stanford University called “Junior” [55] came second in the DARPA Urban Challenge 2007 behind the Tartan Racing team from Carnegie Mellon University [87], after it drove autonomously on a 96 km urban area course with traffic signs and maneuvered around traffic. More recent activities in this area have been conducted and promoted intensively by Google cars in 2010 [82], which have logged over 140,000 miles of autonomous driving.

Although autonomous vehicles that focus on path planning have many proven examples, not much has been emphasized on vehicle control, especially at the limits of handling. Thus, the research in this dissertation was aimed at the vehicle control aspect, so that the future autonomous vehicles know how to maximize tire forces during emergency maneuvers.

1.3 Dissertation contributions and outline

The autonomous racing controller described in this dissertation was designed to gain insights into vehicle control at the friction limits, with the end-goal of applying these

insights into future vehicle safety systems. The controller design was inspired by racecar drivers, and was designed to be intuitive and practical to run in real-time. From these objectives, the following are three key contributions of this dissertation.

1.3.1 A modular controller framework inspired by racecar driver behavior

The controller framework described in Chapter 2 mimics how racecar drivers separate their driving tasks into forming a racing line and controlling their vehicles at the friction limits (Section 1.2.1). As the control inputs are decoupled from the path generation in this approach, the system's structure is more intuitive, unlike the optimization methods discussed in Section 1.2.2. Chapter 2 also explains how racecar drivers use trail-braking and throttle-on-exit techniques to drive a vehicle around a corner at the friction limits. These driving techniques are applied in the control algorithm that uses friction and path information to calculate the controller inputs in real-time. This real-time capability is crucial for adapting the controller to the environmental changes, such as variation in friction value due to rain or changes in the desired path to avoid an obstacle. In contrast, the BMW TrackTrainer does not have this real-time capability because it requires prerecorded data from professional drivers to generate the desired path and the speed profile.

With an application to driver assistance systems in mind, the controller is constructed from individual modules that serve specific tasks, where each module can be adapted into driver assistance systems. Chapter 3 describes a straightforward steering controller with feedback derived from a lanekeeping assistance formulation. Together with the longitudinal controller described in Chapter 4, this results in a basic autonomous racing controller. While very effective, the lanekeeping approach to steering offered some challenges in stability analysis. Thus, the fixed-gain full-state feedback steering module described in Chapter 6 was developed and used in the final design².

²Chapter 6 also demonstrates that the initial feedback steering controller in Chapter 3 can be restructured into the fixed-gain full-state feedback form

1.3.2 Experimental results on an autonomous racing vehicle

The experimental results from testing on different surfaces in Chapter 5 explain how the controller tracks desired paths at the limits of handling. The results also demonstrate the system’s stability even when all the driving aids such as ABS or ESC were switched off, in contrast to the Golf 53+1 and the BMW TrackTrainer where these driving aids were used. The experimental results also highlight which aspects of the controller are important at the limits of handling, such as the effect of yaw damping, tracking the desired speed and the longitudinal weight transfer. The effect of longitudinal weight transfer also indicates one of the ways that a point mass assumption used in some lap-time simulations [51, 91] oversimplifies the problem of driving at the limits.

To fully explore the controller’s potential, the Autonomous Audi TTS was test at Pikes Peak in Colorado, where the path consists of both paved and dirt sections with extreme bank and grade. At Pikes Peak, a complex map with series of consecutive curves was used, which emphasizes the need for the controller to look couple of corners in advance in order to properly monitor the vehicle speed.

1.3.3 Analytical controller design using the center of percussion

The initial steering module in Chapter 3 works well at the friction limits. Nevertheless, a more analytical approach in Chapter 6 was used to restructure the initial steering module into an integrated structure that also facilitates stability analysis. In the initial steering module (Chapter 3), the motion of the center of gravity is used in the feedforward submodule, while the feedback submodule tries to track a reference point projected in front of a vehicle. This creates an inconsistency between the steering submodules. To eliminate this inconsistency, the same reference point at the center of percussion (COP) can be used for both feedforward and feedback steering submodules. At the COP, the rear tire forces do not influence the lateral motion of the COP [50], which greatly simplifies the calculation of the feedforward steering input. The steering module was therefore redesigned to incorporate the motion of the

COP. Furthermore, to improve the fidelity of the feedforward steering module, the tire nonlinearity and transient effects were taken into account. Various sets of gains for the full-state feedback controller were explored, including a set of gains derived from the initial steering feedback controller in Chapter 3 and other sets of gains derived from state-space techniques. With this new steering controller structure, Lyapunov theory was used to show that the closed-loop system is stable even at the limits of handling. In addition, this new steering controller structure still demonstrates path tracking ability at the friction limits in simulation and in experiment.

Chapter 2

Racecar Driver Behavior and Controller Structure

The design of our autonomous racecar was inspired by racecar drivers' ability to control a vehicle at the friction limits without losing control. First, Section 2.1 describes an approach that a racecar driver takes when cornering at the friction limits. Section 2.2 then discusses the structure of the controller and provides an overview of how each module contributes to vehicle control at the limits of handling.

The controller is divided into two parts. First, the path information (Section 2.3) that consists of a predefined path and vehicle limits defines the controller objectives. A predefined path (a racing line), consisting of straight, clothoid and constant radius, is discussed in Section 2.3.1. The desired speed and longitudinal acceleration profiles (Section 2.4) are derived from the curvature of the racing line and the available friction. Once the desired path and the speed profile are calculated, Section 2.5 explains how the controller tracks the desired path at the friction limits.

2.1 Understanding racecar drivers' behavior

A racecar driver's goal is to win a race, which means finishing the race with the fastest time. To be fast around a track, a racecar driver has to fully utilize tire forces while tracking a racing line. To finish a race, a driver has to avoid losing

control of the vehicle while driving at the limits. Furthermore, a top driver has to perform consistently, regardless of the changes in the environment or in the vehicle’s characteristics (robustness). Thus, a racing controller has to robustly track a desired path, utilize tire forces, and stabilize the vehicle.

Racecar drivers achieve the above objectives through their ability to estimate friction and utilize friction information to control a vehicle at the limits. During practice, they formulate a racing line, and through their understanding of vehicle limits, they coordinate their inputs to follow their racing line at the limits of tire adhesion.

2.1.1 Cornering sequences

Figure 2.1(a) depicts how racecar drivers structure their racing line when driving through a turn [45, 3, 78]. At the corner apex, they pick the constant radius arc (which corresponds to a constant steering angle) with the largest radius to maximize vehicle speed. To connect between straight and constant radius sections, a driver needs a transition curve during corner entry and corner exit; during these transitions, drivers have to increase or decrease their steering angle respectively. Thus, in general, each cornering sequence consists of a corner entry where the curvature transitions from zero (straight) to a constant value, a mid corner where the turning radius is constant, and a corner exit where the curvature changes from a constant value back to zero.

Racecar drivers may change the position of the corner apex to create “early apex” or “late apex” turns [78, 45]. Changing the position of the apex affects the corner entry and corner exit speeds, which the drivers have to tradeoff. This tradeoff depends on the type of vehicles that the drivers use as well as the layout of the track.

Once a racing line is established, racecar drivers have to understand their friction limits before they can provide correct inputs to the vehicle.

2.1.2 Understanding vehicle limits on a “ $g-g$ ” diagram

Racecar drivers follow their racing line while ensuring that they maximize the tire forces governed by the friction between the tires and the track surface. They use the

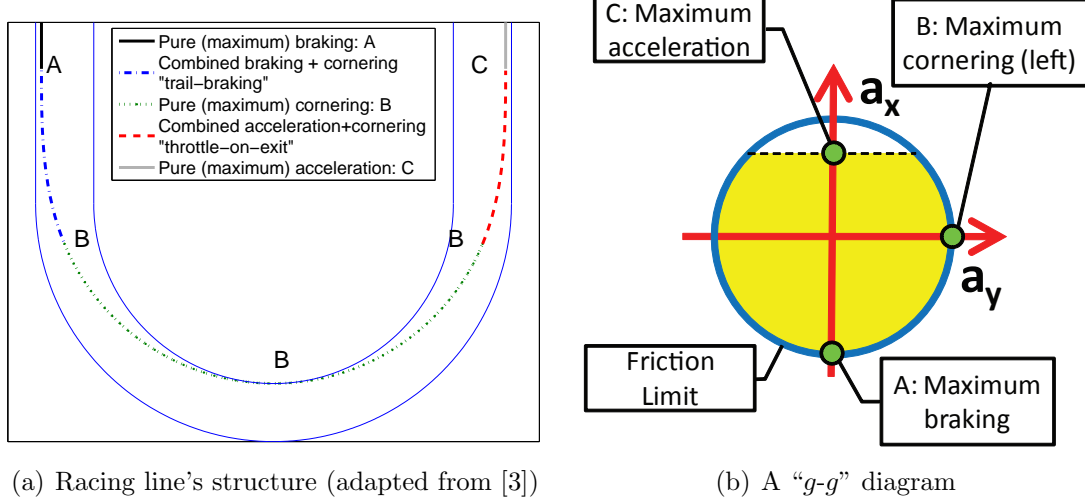


Figure 2.1: Driving at the limits

concept of a friction circle (or traction circle) to conceptualize these limits [45, 3]. To translate this concept into a mathematical model, a “*g-g*” diagram [64, 49] is used (Fig. 2.1(b)).

The force an individual tire can produce is limited by friction. For an isotropic tire, these limits can be viewed as a friction circle on axes of lateral and longitudinal force. The friction forces from the four tires define the vehicle’s capability. During driving, the capability of each tire is continuously changing due to longitudinal and lateral load transfer and aerodynamic downforce effects. These effects can be modeled to give a more accurate sense of the vehicle’s limits in different trim states, but for simplicity, the resulting diagram is often simplified to the same basic circular shape as the isotropic tire. This is known as the friction circle or traction circle for the vehicle.

Force and acceleration are related through Newton’s second law. Since the acceleration of a vehicle can be measured more easily than the forces, the ability of a driver to operate a vehicle at its limits is often evaluated using a friction limit circle on a “*g-g*” diagram (Fig. 2.1(b)). Thus, the acceleration that the driver achieves at

different points along the course can be compared to the maximum acceleration predicted by a simple “ g - g ” diagram or a more complicated representation incorporating load transfer (see Appendix A).

2.1.3 Driving at the limits

Once a racing line and the vehicle limits have been established, the remaining task is to modulate brake, throttle and steering inputs to track the racing line in Fig. 2.1(a) while tracing the friction limit circle in Fig. 2.1(b). To drive at the limits, racecar drivers apply pure braking during the last straight section before the corner entry, point A in Fig. 2.1(b). Similarly, during pure cornering around the apex, they maximize their tire forces in a lateral direction without using any longitudinal forces (point B). At point C, the driver applies the maximum longitudinal acceleration allowed by the engine’s torque (the dashed line in Fig. 2.1(b)). The challenge arises during the transition phases (corner entry and exit), where drivers have to coordinate their steering and longitudinal inputs by using trail-braking and throttle-on-exit techniques.

Trail-braking and throttle-on-exit

During corner entry, racecar drivers have to make a transition from the straight to the constant radius section (Fig. 2.1(a)), while tracing the friction limit circle from point A to point B in Fig. 2.1(b). They have to delicately balance their tire forces between braking and steering to trace the fourth quadrant of the friction limit circle depicted in Fig. 2.1(b). This technique is called trail-braking [45, 90], during which drivers slowly decrease the amount of braking while increasing the amount of steering. Similarly, during corner exit, drivers use a throttle-on-exit technique where they slowly increase their throttle input while unwinding the steering wheel to trace the first quadrant of the friction limit circle (from point B to point C).

The tradeoff between the available cornering and braking forces during corner entry highlights the importance of corner entry speed. If drivers approach the corner entry too fast, tracking the original racing line becomes unfeasible. Higher vehicle

speed requires higher cornering force, which consequently reduces the available braking force. Thus, as the corner becomes tighter, a vehicle traveling at an excessive speed will prematurely use all of the friction capability for cornering and not be able to track the racing line. If drivers choose to stay on the brake, they no longer have sufficient cornering force to remain on the path. Thus, no matter what drivers do, if the vehicle approaches the corner with excessive speed, it will deviate from the desired path. To avoid this problem, drivers have to hit the braking point properly in order to achieve the correct entry speed. If the drivers notice that they are approaching the corner too fast, they have to modify their path to create a “recovery line” [3, 41]. Notice that this dilemma does not exist in the corner exit. Lifting the throttle reduces vehicle speed without sacrificing any cornering ability because the curvature is decreasing.

2.2 A controller architecture for racing

As described in Section 2.1, racecar drivers divide driving at the limits into two tasks [78, 45, 3]. First, they find a racing line and understand the available friction limits through practicing. After practicing, they have a racing line and a speed profile that they want to track. From these objectives, they plan their steering, throttle and brake inputs and while driving, they adjust these inputs according to tracking errors.

To mimic these racecar drivers’ behaviors, the controller separates path information from path tracking at the limits, as shown in Fig. 2.2. The path information contains the targets that the controller tries to achieve, i.e., the desired path that the vehicle wants to track as well as the desired speed and acceleration profiles that the vehicle tries to achieve. To track the path at the friction limits, the controller separates the task into controlling the vehicle’s lateral motion through the steering input and the longitudinal motion through the throttle and brake. Both the steering and longitudinal controllers consist of feedforward and feedback modules that imitate racecar drivers planning their control inputs and adjusting their inputs according to errors.

There are advantages from structuring the controller as shown in Fig. 2.2. With

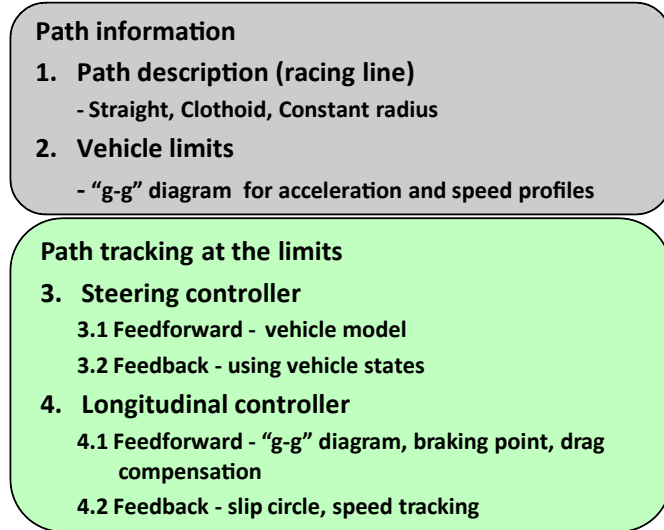


Figure 2.2: Overall controller structure

modular controller design, the benefits of each module can be realized and the interaction between each module can be investigated. Furthermore, each controller module can be adapted for future driver assistance systems. For instance, we can integrate steering feedback or longitudinal feedback into driver assistance systems where the system can help the driver during extreme maneuvering, such as preventing loss of vehicle control on an icy road or other low friction surface.

2.3 Path information

Similar to a racecar driver sensing the environment, the controller has to know its reference value (desired path) and its control authority (available friction), which dictates the speed and acceleration profiles. From this path information, the controller can calculate its feedforward commands.

2.3.1 Path description (racing line)

A predefined path, which consists of three types of segments - a straight, a transition curve and a constant radius curve - is structured to mimic a racecar driver's racing

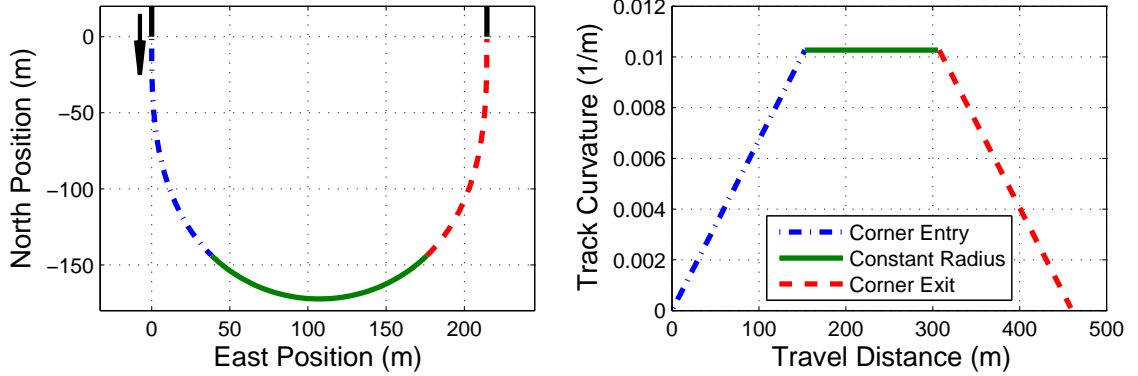


Figure 2.3: Clothoid map: showing (a) shape and (b) curvature

line (Fig. 2.3). A clothoid geometry is used for a transition curve as its curvature changes linearly with the distance traveled, resulting in smooth feedforward steering and simplifying the feedforward longitudinal calculation. The following section explains a clothoid curve in detail.

Clothoid path

Transition curves (corner entry and exit) are required to connect between straight and constant radius sections. During these transitions, the controller trail-brakes or applies throttle-on-exit to mimic racecar drivers driving at the friction limits. Any abrupt change during these transitions is undesirable as it can upset vehicle balance. A clothoid curve, which has linear curvature (Fig. 2.3(b)), is chosen to approximate this transition as it produces a linear steering input between straight and constant radius sections when the vehicle speed is constant. Besides the clothoid map having nice mathematical properties, Theodosis et al. [79] show that it is possible to fit a clothoid map into a racing line, as shown in Fig 2.4.

A clothoid path (also known as an Euler Spiral) is commonly used in highway road design [1]. It is based on a Fresnel Integral [40] and contains only one parameter c , which describes the shape of the clothoid. This parameter c controls the rate that the curvature changes along the segment, i.e., the slope of the curvature in Fig. 2.3(b). A clothoid can be expressed as

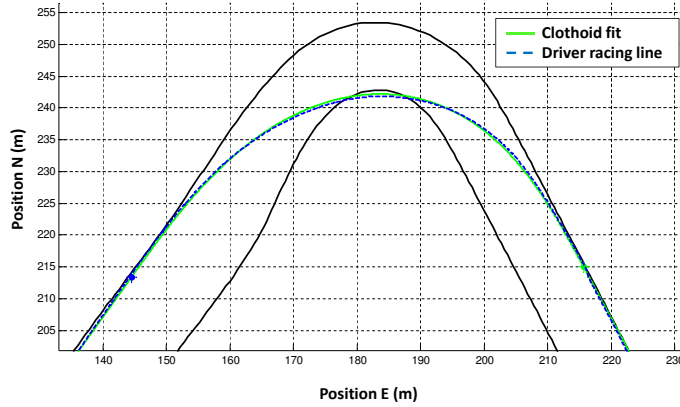


Figure 2.4: Clothoid map fits to a racecar driver’s racing line (courtesy to Paul Theodosis)

$$\begin{aligned} x &= C(\dot{s}) = \frac{1}{c} \int_0^{\dot{s}} \cos(q^2) dq \\ y &= S(\dot{s}) = \frac{1}{c} \int_0^{\dot{s}} \sin(q^2) dq , \end{aligned} \quad (2.1)$$

where $\dot{s} = cs$ and s is the distance measured along the clothoid segment.

The curvature $\mathcal{K}(s)$ of a track can simply be found from [20]

$$\mathcal{K}(s) = \frac{1}{R(s)} = \frac{\dot{x}\ddot{y} - \dot{y}\ddot{x}}{(\dot{x}^2 + \dot{y}^2)^{\frac{3}{2}}} , \quad (2.2)$$

where $R(s)$ is the radius of the clothoid curvature, $\dot{x} = \frac{dx}{ds}, \dot{y} = \frac{dy}{ds}$, $\ddot{x} = \frac{d^2x}{ds^2}$, and $\ddot{y} = \frac{d^2y}{ds^2}$. By substituting x and y from Equation 2.1 into Equation 2.2, the clothoid curvature is

$$\mathcal{K}(s) = \frac{1}{R(s)} = 2c^2s . \quad (2.3)$$

This linear relationship between curvature \mathcal{K} and the distance traveled s produces a smooth feedforward steering that will be described in Section 3.1. In previous work, which used a polynomial-based map [66] to calculate the feedforward steering, abrupt changes in the feedforward steering input were observed. These sudden changes were caused by the unevenness of the second derivative values in equation (2.2) when using the polynomial-based map. This undesired steering motion caused the vehicle to oscillate along the path, creating a yaw motion and unnecessary front tire slip, which became a critical issue during cornering at the limits. With a clothoid map, the transition of the curvature along the path is smooth and results in smooth feedforward steering. Furthermore, the linear relationship between distance traveled and curvature greatly simplifies the feedforward longitudinal calculation in Section 2.4. In addition, a clothoid curve has many established methods for curve fitting within some geometry constraints [94, 2, 79].

2.3.2 Friction estimation

A friction limit circle on a “ g - g ” diagram is used to describe the vehicle limits, which governs the maximum acceleration (and hence, the speed profile) that a vehicle could achieve. In this research, the controller uses a priori knowledge of friction obtained from a ramp steer maneuver and relies on the controller robustness to handle any variation of the track surface. This can easily be extended to include real-time friction estimation based on tire slip or aligning moment [26].

2.4 Calculate desired speed profile from path information and friction limit

Besides tracking the desired path, the controller also has to drive a vehicle at the friction limits. Once the desired path is defined and the available friction is found (Section 2.3.2), a point mass model can be used to find the maximum achievable speed profile that the controller will try to track. Our method of finding the desired speed profile is similar to the method used in lap-time simulation [51, 7]; although,

later on in Section 2.4.5, we will include the effect of weight transfer, bank and grade into the calculation.

Once the desired speed profile is found, the longitudinal acceleration profile, which is a by-product of the calculation process, will be used for the feedforward longitudinal calculation in Section 4.1.1. In addition, from a desired corner entry speed, the braking point on the preceding straight section can be determined. This braking point is an important parameter because it dictates how the vehicle will behave in the subsequent corner, as will be discussed in Section 2.4.3.

One of the methods of finding the friction limit circle in Fig. 2.1(b) is to use a ramp steer maneuver. Once the limits are known, the goal of this section is to compute the desired speed (and the desired longitudinal acceleration) while traveling along the desired path. The friction limit circle in Fig. 2.1(b) can be translated into a simple mathematical relationship between a_x and a_y as follows:

$$(\mu g)^2 = a_x^2 + a_y^2 , \quad (2.4)$$

where a_x is vehicle's longitudinal acceleration, a_y is vehicle's lateral acceleration and μ is an effective friction coefficient.

To estimate the desired speed profile and the longitudinal acceleration along the clothoid segment s , the calculation starts by substituting curvature \mathcal{K} from (2.3) into a_y , approximated by steady state cornering:

$$a_y(s) \approx \frac{U_x(s)^2}{R(s)} = U_x(s)^2 \mathcal{K}(s) = U_x(s)^2 2c^2 s , \quad (2.5)$$

where $U_x(s)$ is the desired speed along the traveled distance s and $R(s)$ is the radius of the curvature along the path s . These $a_x(s)$ and $a_y(s)$ in (2.5) will make the vehicle's acceleration trace the friction limit circle on a “ $g-g$ ” diagram while going around a corner.

The curve in Fig. 2.3 is divided into three sections, and each has a different calculation process. The calculation starts by estimating the desired vehicle speed at the corner's apex and then integrating along the path to find the desired speed along

the path $U_x(s)$.

2.4.1 Constant radius

At mid corner, the vehicle is operating at maximum cornering (point B in Fig. 2.1(b)), where $a_x = 0$ and $a_y = \mu g$. The speed at this point can be found from using (2.4) and (2.5). As a consequence, $U_x(s) = \sqrt{\mu R(s)g}$, where $R(s)$ is the radius of the curvature at the apex.

2.4.2 Clothoid entry

The goal of this section is to calculate the correct amount of $U_x(s)$ (and $a_x(s)$) at each point along the clothoid entry s , so that when combined with the $a_y(s)$ generated from vehicle cornering, the vehicle's acceleration will trace counterclockwise along the fourth quadrant of the friction limit circle. That is, the vehicle's acceleration will make a transition from full-braking (point A in Fig. 2.1(b)) to full cornering (point B), similar to racecar drivers trail-braking.

The overall concept of finding longitudinal acceleration $a_x(s)$ relies on the process of finding $U_x(s)$. Once $U_x(s)$ is known, $a_y(s)$ can be estimated from (2.5). Thus, if the available friction μ and $a_y(s)$ are known, $a_x(s)$ can be found from (2.4).

The calculation of $U_x(s)$ starts by substituting $a_y(s)$ from (2.5) into (2.4), and rearranging (2.4) to obtain

$$a_x(s) = \sqrt{(\mu g)^2 - (2c^2 s U_x(s))^2} . \quad (2.6)$$

From the differential equation of $a_x(s)$,

$$a_x(s) = \frac{dU_x(s)}{dt} = \frac{dU_x(s)}{ds} \frac{ds}{dt} = \frac{dU_x(s)}{ds} U_x(s) , \quad (2.7)$$

where t is time. Substituting this definition of $a_x(s)$ into (2.6) produces

$$\frac{dU_x(s)}{ds} = \frac{1}{U_x(s)} \sqrt{(\mu g)^2 - (2c^2 s U_x(s)^2)^2}. \quad (2.8)$$

Equation (2.8) is then solved in real-time by using backward integration.

$$\begin{aligned} U_x(\tilde{s}_{n+1}) &\approx U_x(\tilde{s}_n) + \frac{\Delta\tilde{s}}{U_x(\tilde{s}_n)} \sqrt{(\mu g)^2 - (2c^2 \tilde{s}_n U_x(\tilde{s}_n)^2)^2} \\ \Delta\tilde{s} &= \tilde{s}_{n+1} - \tilde{s}_n \end{aligned} \quad (2.9)$$

for $n = 0, 1, 2, \dots, L^{cloth}/\Delta\tilde{s}$, where $\tilde{s}_n = n\Delta\tilde{s}$, \tilde{s} is the traveled distance measured from the end of clothoid, i.e., $\tilde{s} = L^{cloth} - s$, and L^{cloth} is the length of the clothoid section. The integration starts from the end of the clothoid entry where $\tilde{s} = 0$ (point B in Fig. 2.1(b)) and ends at the beginning of the clothoid where $\tilde{s} = L^{cloth}$ and $\mathcal{K} = 0$ (point A). The speed calculated from the constant radius section is used as the initial condition.

After $U_x(s)$ along the clothoid entry is found from (2.9), the desired longitudinal acceleration $a_x(s)$ along s can be found from (2.6).

One of the key parameters in this section is the calculated corner entry speed that came from (2.9). This corner entry speed greatly influences how the vehicle will corner, as will be discussed in the following section.

2.4.3 Straight

Once the desired vehicle speed along the path $U_x(s)$ is found, a corner entry speed and the braking point on the preceding straight section can be determined. This braking point is an important parameter. Braking too early or too much will result in a slower corner entry speed, because the vehicle does not fully utilize the tire forces. Braking too late or not sufficiently will result in vehicle sliding or deviation from the intended path as mentioned in Section 2.1.3.

Thus, in order to achieve the correct corner entry speed, the controller has to start braking in the section before reaching the corner entry. If the section before corner

entry is a straight section, the braking distance $s_{braking}$ can be found from

$$s_{braking} = \frac{(U_x)^2 - (U_x^{entry})^2}{2\mu g} , \quad (2.10)$$

where U_x is the current vehicle speed and U_x^{entry} is the desired corner entry speed. This braking point is calculated in real-time. In practice, the effect of the time delay in the braking system has to be compensated by the controller. A conservative safety factor can also be added into (2.10) by slightly scaling μ down to ensure sufficient braking distance is available to achieve the correct entry speed.

2.4.4 Clothoid exit

During corner exit, the controller transitions from full cornering (point B in Fig. 2.1(b)) to full acceleration (point C). It uses a throttle-on-exit technique to trace along the circle by modulating the correct amount of throttle and steering.

Similar to the clothoid entry, calculating the longitudinal acceleration $a_x(s)$ starts by estimating $U_x(s)$ at the constant radius section. Equation (2.8) has to be integrated from the beginning of the clothoid, where $s = 0$, to the end of the clothoid, where $s = L^{cloth}$. Similar to the clothoid entry, the initial condition at $s = 0$ is found from the constant radius section.

Note that the estimated vehicle speed $U_x(s)$ could be overestimated as the powertrain may not have sufficient torque to accelerate the vehicle out from a corner at its friction limit, see Fig. 2.1(b). From the controller standpoint, this will simply saturate the throttle command at wide open throttle, which is the desired behavior. If a more accurate $U_x(s)$ is desired for simulation purpose, equation (2.8) can be modified to

$$\frac{dU_x(s)}{ds} = \frac{1}{U_x(s)} a_x^{powertrain} , \quad (2.11)$$

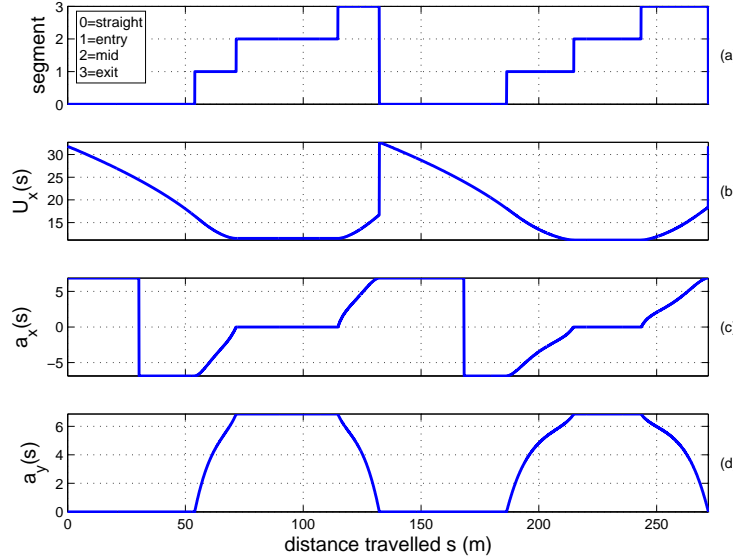


Figure 2.5: Speed and acceleration profiles using parameters from Table 5.3 and B.1: showing (a) type of segment (b) speed profile (c) longitudinal acceleration profile and (d) lateral acceleration profile

whenever the calculated $a_x(s)$ is higher than the available acceleration from the powertrain $a_x^{powertrain}$.

Figure 2.5 shows the speed and acceleration profiles when a vehicle is driving around an oval map. The type of segment is shown in Fig. 2.5a, where 0 = straight, 1 = clothoid entry, 2 = constant radius, and 3 = clothoid exit. During cornering, the speed profile $U_x(s)$ is calculated from (2.8). The speed profile in the straight section is calculated from $U_x(s) = \sqrt{(U_x^{entry})^2 + 2\mu gs}$, where s is the distance to the next segment. There is a discontinuity in $U_x(s)$ when the vehicle travels from the clothoid exit to the straight segment (see Fig. 2.5b) because different equations are used for calculating $U_x(s)$. This does not cause any concern because the controller will just apply full throttle after the corner exit, which is the correct behavior as will be described in Section 5.4.1.

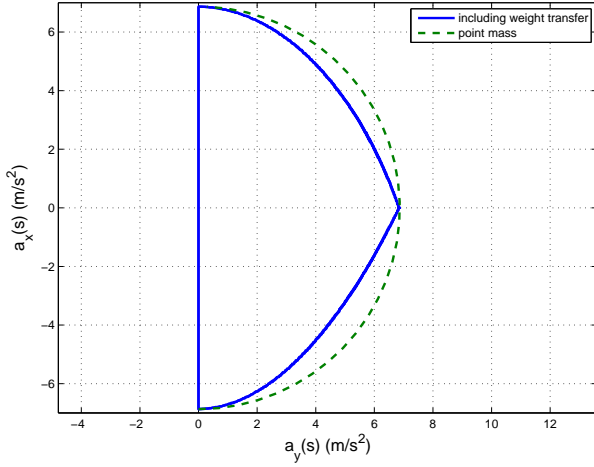


Figure 2.6: Effect of longitudinal weight transfer on maximum achievable acceleration, $\mu = 0.7$ (using parameters from Table 5.3 and B.1)

2.4.5 Effect of longitudinal weight transfer, bank and grade

The effects of longitudinal weight transfer, bank and grade are taken into account in the controller; a detailed explanation is given in Appendix A and the vehicle parameters in Table B.1 are used. Although, the core of the calculation process still follows the procedures described in this section.

The friction limit circle in a “ $g-g$ ” diagram lumps all four tires into one circle. When testing this assumption at the limits on a low friction surface, an oversteering behavior during trail-braking was observed. This was due to the weight transfer during braking where the rear normal force was reduced, causing the rear tires to slide. Thus, to overcome this issue, we use a quasi-static weight transfer assumption to predict the changing normal load. Rather than using a friction limit circle that represents all four tires, front and rear friction limit circles with sizes varying according to their normal load are used. Figure 2.6 depicts how the effect of weight transfer reduces the maximum acceleration that the vehicle can generate.

Furthermore, the bank and grade of the path affect the normal load of each tire. The orientation of the bank dictates if the vehicle can travel faster or slower around a

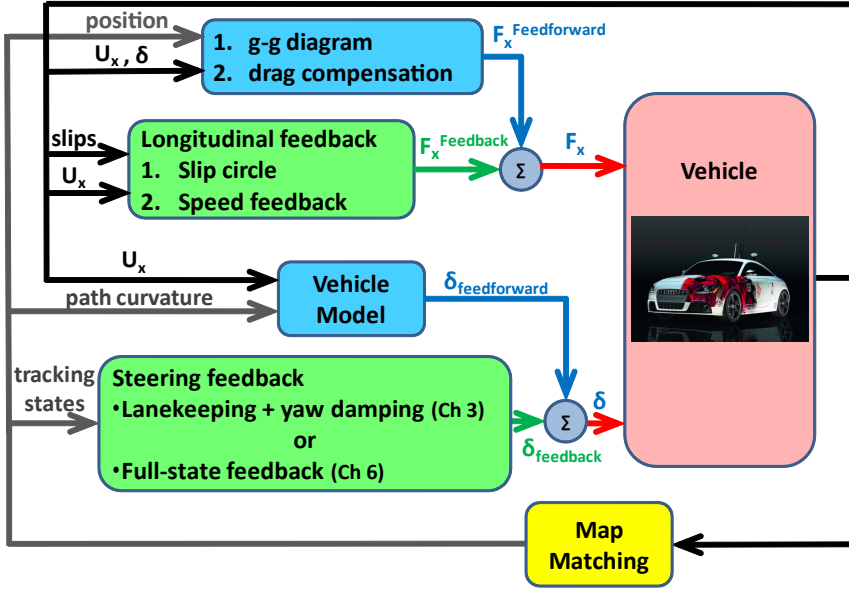


Figure 2.7: Overall controller block diagram

corner. For instance, an off-camber corner¹ reduces the normal load during cornering, and thus, reduces the cornering speed.

2.5 Path tracking at the limits

Similar to racecar drivers planning ahead, feedforward controllers are designed to calculate steering and longitudinal inputs that track the path while the vehicle's acceleration traces the friction limit circle. During driving, feedback controllers imitate a driver's vehicle control ability, making adjustments based on vehicle responses and tracking errors. Figure 2.7 shows the block diagram of the controller, which represents the path tracking part of the controller in Fig. 2.2.

¹when the inside of the corner is higher than the outside of the corner

2.5.1 Steering controller

Once the curvature of a track is known, a feedforward steering command can be calculated from a vehicle model. The steering feedback based on measured vehicle states adds robustness to the controller and mitigates any tracking errors caused by modeling errors or any system disturbances. Consequently, the steering controller provides the system with path tracking ability and system robustness.

Two different approaches for designing a steering controller are discussed in this dissertation. Chapter 3 explains how a basic steering controller uses a linear bicycle model to calculate a feedforward steering, while a lanekeeping system [66] with yaw damping is employed for the feedback steering. The results from this initial steering controller provide insights into the controller design and lead to the new steering controller structure in Chapter 6. A more analytic design approach is proposed in Chapter 6, where the feedforward and feedback steering are derived from equations of motion and full-state feedback is used for designing the feedback steering controller.

2.5.2 Longitudinal controller

Using the curvature of the track and the available friction, the longitudinal feedforward controller estimates the desired longitudinal acceleration and the speed profile around a corner (see Chapter 4). The feedforward controller calculates the amount of throttle and brake for a desired trajectory, as explained in [43], to trace the friction limit circle on a “ g - g ” diagram [49]. This is similar to a racecar driver using trail-braking and throttle-on-exit techniques [45, 3, 92]. Once the corner entry speed is known, the braking point on the preceding straight section can be determined. This braking point is an important parameter. Braking too early or too much will result in a slower corner entry speed. Braking too late or not sufficiently will result in vehicle sliding or deviation from the intended path. For the longitudinal feedback controller, a slip circle is used to control tire slip while speed feedback is employed to ensure that the vehicle speed tracks the desired speed profile.

Chapter 3

Basic Lateral Controller (Steering Controller)

Although the steering structure in Chapter 6 was used in the final design, this chapter describes how an initial steering controller was utilized to quickly analyze the system's performance and identify the challenges of controlling an autonomous vehicle. Simplifications were made in the feedforward steering submodule to enable rapid prototype of the complete racing controller and to understand what factors most heavily influence the controller's performance at the friction limits. Even with this basic design, the steering controller can perform at the limits of handling while maintaining minimal tracking errors, as discussed in more detail in Chapter 5. The steering feedback submodule in this chapter was restructured into a fixed-gain full-state feedback form in Chapter 6 to perform stability analysis.

A steering controller is used to mimic racecar drivers controlling a vehicle at the limits through the steering inputs. A feedforward steering controller is used to predict the steering command while a feedback steering controller is designed to adjust the steering input according to tracking errors. As a consequence, the desired steering command is calculated from the sum of feedforward and feedback steering controllers. Figure 3.1 shows the structure of the initial steering controller discussed in this chapter that is a part of the autonomous vehicle controller, shown in Fig.2.7.

As Fig. 3.1 demonstrates, the feedforward steering controller uses a vehicle model

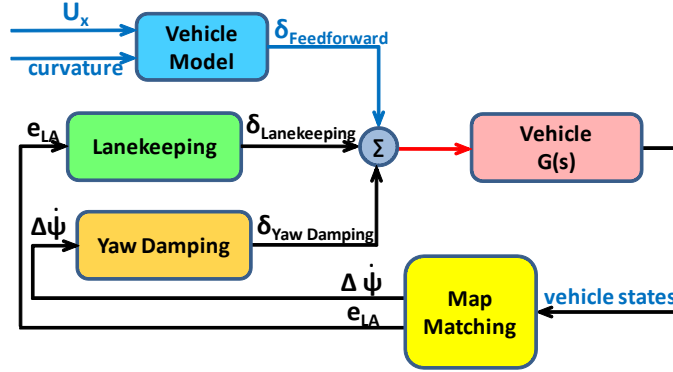


Figure 3.1: Basic steering controller: consisting of feedforward steering, lanekeeping feedback steering and yaw damping feedback steering.

to predict the required steering angle. The feedback steering controller requires vehicle states referenced to the path. Consequently, a map-matching algorithm [66] uses the current vehicle position and the knowledge of the desired path to calculate the vehicle's lateral error e and heading error $\Delta\psi$. The remainder of this chapter explains how a bicycle model is used for calculating a feedforward steering input while a lanekeeping system and yaw damping are employed for a steering feedback.

3.1 Feedforward steering controller using a bicycle model

Feedforward steering actively predicts the steering input to minimize lateral tracking error. If a controller does not include any feedforward steering, the vehicle has to deviate from the path before the lanekeeping system starts to steer the vehicle back to the path. Thus, the addition of a driver steering model (feedforward steering) into the system improves the performance of the system because the feedforward steering will steer the vehicle before it deviates from the path.

Several methods to determine the feedforward steering from the lateral acceleration and path information exist. It can be calculated from a complex vehicle model

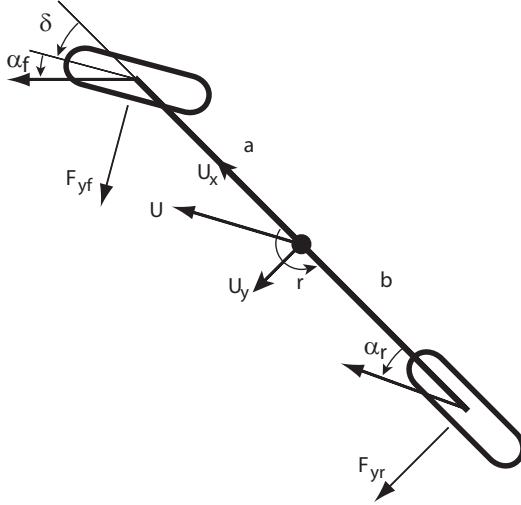


Figure 3.2: Planar bicycle model

with four nonlinear tires. Alternatively, empirical data generated from a ramp steer maneuver can create a vehicle specific steady-state feedforward steering lookups table. For simplicity in the initial study in this chapter, the analysis uses a basic bicycle model, shown in Fig. 3.2, with a linear tire and a steady state assumption. The effects of the tire modeling errors are then handled by the steering feedback. A more comprehensive feedforward steering, which includes tire nonlinearity and transient dynamics of the system, will be discussed in Chapter 6.

By using vehicle kinematics and assuming small angles, the feedforward steering is found from

$$\delta_{feedforward} = \frac{Lr}{U_x} - \alpha_f + \alpha_r . \quad (3.1)$$

where δ is the steering angle, L is the vehicle length in Fig. 3.2, r is the vehicle yaw rate, α_f and α_r are the front and rear slip angles, respectively. These slip angles are derived from vehicle kinematics.

The equations of motion are derived from a bicycle model, assuming the vehicle is cornering at a steady state, i.e.

$$\begin{aligned} F_{yf} + F_{yr} &= ma_y = m \frac{U_x^2}{R(s)} \\ aF_{yf} - bF_{yr} &= 0 , \end{aligned} \quad (3.2)$$

where m is the vehicle mass, a and b are the distances from the front and the rear axle to the vehicle's center of gravity, F_y^f and F_y^r are the front and the rear lateral forces, and a_y is the vehicle's lateral acceleration.

To derive the feedforward steering, a linear tire assumption is used

$$F_y = -C\alpha , \quad (3.3)$$

where C is the lateral axle cornering stiffness.

The distribution between front axle normal load W_f and rear axle normal load W_r can be found from

$$\begin{aligned} W_f &= \frac{b}{L}mg \\ W_r &= \frac{a}{L}mg . \end{aligned} \quad (3.4)$$

Substituting (3.3) and (3.4) into (3.2) yields the following relations:

$$\begin{aligned} -C_f\alpha_f &= \frac{W_f}{g} \frac{U_x^2}{R(s)} \\ -C_r\alpha_r &= \frac{W_r}{g} \frac{U_x^2}{R(s)} \end{aligned} \quad (3.5)$$

The slip angles from the above equations are then used in Equation 3.1, resulting in the following expression for the feedforward steering:

$$\delta_{feedforward} = \left(L + \frac{K_{ug} U_x^2}{g} \right) \frac{1}{R(s)} , \quad (3.6)$$

where K_{ug} is the vehicle understeer gradient

$$K_{ug} = \frac{W_f}{C_f} - \frac{W_r}{C_r} . \quad (3.7)$$

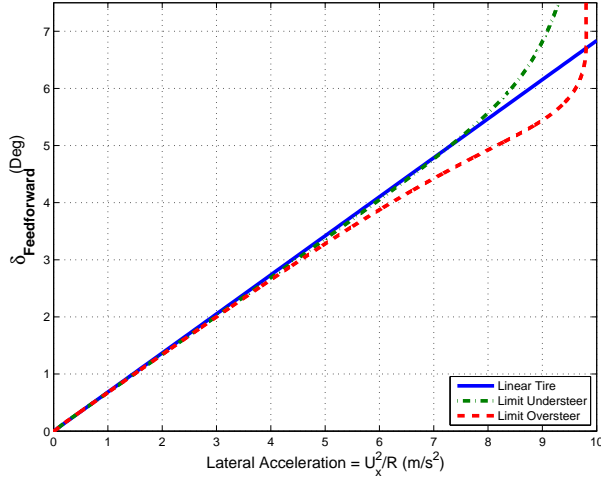


Figure 3.3: Example of feedforward steering from a handling diagram, using ramp steer $U_x = 15 \text{ m/s}$

With a clothoid curve, the curvature along the path $1/R(s)$ in (3.6) can easily be found from (2.3).

With the feedforward steering controller described above, the system has some tracking errors because a linear tire assumption is used. Figure 3.3 depicts an example of variations seen in the feedforward steering when either a linear tire model or a brush tire Fiala model [60] is used ¹. The discrepancy is caused by the differences in the effective cornering stiffnesses, which appear in (3.6) through the vehicle understeer gradient K_{ug} in (3.7). The difference is most noticeable at high lateral acceleration. Although it is possible to improve the accuracy of the feedforward steering by incorporating a nonlinear tire model into (3.6), as will be described in Chapter 6, the preliminary goal of this chapter is to demonstrate how a simple controller performs and observe how feedback controller minimizes the effect of this modeling error.

¹A 4-wheels vehicle model was used with the parameters from Table B.1. Different roll bar stiffnesses were utilized to create understeer and oversteer characteristics (front and rear roll bar stiffness= 90,000 and 80,000 Nm/rad respectively for understeer, and 50,000 and 90,000 Nm/rad respectively for oversteer).

3.2 Feedback steering controller

During testing, the system would be subject to tracking errors due to possible disturbances from the testing environment or from modeling errors because a linear tire assumption is used. To negate any effects of system disturbances and modeling errors, as well as to improve vehicle stability, a steering feedback based on a potential field lanekeeping system [24, 65, 66, 74] is added with additional yaw damping. The steering feedback based on lanekeeping provides path tracking ability and adds robustness to the autonomous racing controller. The yaw damping feedback minimizes the vehicle's yaw oscillation, which can grow as the tires saturate.

3.2.1 Lanekeeping

The controller is built around a potential field lanekeeping system, which provides stability, robustness and path tracking up to the limits of tire adhesion [77]. The lanekeeping feedback mitigates tracking errors due to possible disturbances from the testing environment or from modeling errors caused by the linear tire assumption described in Section 3.1.

The lanekeeping feedback produces an additional steering angle, which is proportional to the lookahead error e_{la} in Fig. 3.4(a).

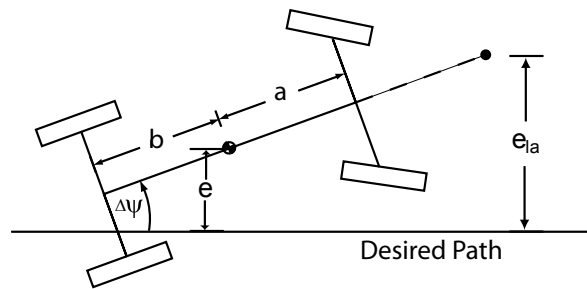
$$\delta_{control} = -\frac{2k_p}{C_f} e_{la} \quad (3.8)$$

where k_p is the lanekeeping potential field gain.

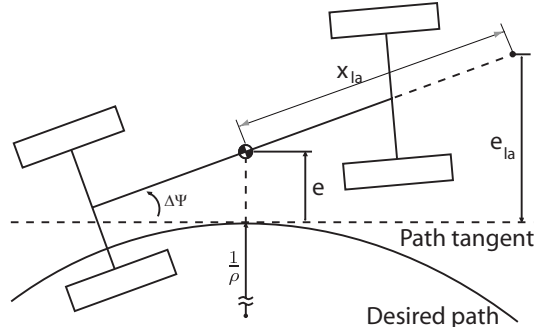
Note that the lookahead error e_{la} in Fig. 3.4(a) is a combination of both lateral error e and heading error $\Delta\psi$, that is

$$e_{la} = e + x_{la} \sin \Delta\psi . \quad (3.9)$$

Substituting e_{la} in Equation 3.9 into Equation 3.8 gives



(a) Definition of heading error ($\Delta\psi$) and lookahead error (e_{la}) on a straight path



(b) Lanekeeping on a curved path

Figure 3.4: Lanekeeping system

$$\delta_{control} = -\frac{2k_p}{C_f}(e + x_{la} \sin(\Delta\psi)) . \quad (3.10)$$

The lanekeeping potential field gain k_p is chosen to ensure stability, as described in [65, 66] and [77], but the lookahead distance x_{la} is tuned for sustained driving at the handling limits. As x_{la} is increased, the lanekeeping system becomes more sensitive to the vehicle's heading error $\Delta\psi$ (see (3.10)). This produces a quick response to vehicle yaw motion, which improves yaw stability. However, if x_{la} is too high, the lanekeeping steering command will become too sensitive to vehicle yaw motion and induce yaw oscillation in the system [77]. Thus, choosing x_{la} is a tradeoff between yaw stability and yaw oscillation during tire saturation. A slightly shorter lookahead distance of $x_{la} = 20$ m is used together with yaw damping feedback to help mitigate this yaw oscillation. Although it is possible to design a lookahead distance x_{la} that varies with vehicle speed, a constant lookahead distance is used in this design to keep the complexity of the controller low.

It is important to point out that the error signal e_{la} used in this lanekeeping system is based on the projection to the closest point on the desired path, as shown in Fig. 3.4(b). As a consequence, the lanekeeping feedback does not depend on the future path information and does not have any inherent conflict with the feedforward steering. This approach is different from lanekeeping systems that use feedback based on future path information, such as the one proposed by [86].

In addition, the steering controller limits the amount of steering needed to avoid exceeding a maximum lateral slip, α^{lim} , on the front axle. Since no additional lateral tire force is generated after the lateral slip exceeds the peak slip, α^{peak} , where the maximum lateral force is generated, there is no significant benefit from additional steering when the lateral slip $\alpha > \alpha^{peak}$. In practice, α^{lim} is chosen to be slightly higher than α^{peak} to ensure that the front axle could generate maximum force and to enable the longitudinal feedback controller to detect any excessive tire slip.

3.2.2 Lanekeeping stability

The lanekeeping steering system used in Section 3.2.1 is proved to be stable even at the friction limits. Hindiyeh et al. explains how this lanekeeping provides yaw stability to the system, while Talvala et al. [76, 77] use Lyapunov theory to prove system stability even when the tires are operating in the nonlinear region. The system is proved to be stable for a range of tire slip even when longitudinal tire force is present. Consequently, adding the longitudinal controller into the system should have minimal impact on the system's stability. Furthermore, Chapter 4 will explain that the longitudinal controller is in fact, minimizing tire slip, which should improve system stability. In Chapter 6, the initial steering controller in this chapter will be restructured into a state-space form, and the system's stability at the friction limits will be discussed in detail.

3.2.3 Yaw damping

In addition to the lanekeeping system, a small amount of yaw damping is added into the steering feedback controller to minimize yaw oscillation. At the limits of handling, the yaw dynamics become more oscillatory since the inherent damping due to the tire forces decrease. Yaw oscillation is undesirable, as it creates unnecessary lateral tire slip. This reduces the available longitudinal tire force that can be used for accelerating the vehicle along the path.

To reduce yaw motion of the vehicle, a steering feedback term $\delta_{damping}$ based on $\Delta\dot{\psi} = d\Delta\psi/dt$ is added into the lanekeeping Equation (3.10) to obtain

$$\delta_{damping} = -k_{\Delta\dot{\psi}}\Delta\dot{\psi}, \quad (3.11)$$

where $k_{\Delta\dot{\psi}}$ is the yaw damping gain.

Rather than differentiate $\Delta\psi$ to obtain $\Delta\dot{\psi}$, which could amplify high frequency noise, $\Delta\dot{\psi}$ is calculated from the measured vehicle states

$$\begin{aligned}\Delta\dot{\psi} &= \dot{\psi}_{CG} - \dot{\psi}_r \\ &= r - U_x \mathcal{K}(\cos \Delta\psi - \tan \beta \sin \Delta\psi),\end{aligned}\tag{3.12}$$

where ψ_{CG} is the heading angle of the vehicle relative to an earth frame, ψ_r is the heading angle of the path relative to the earth frame, \mathcal{K} is the road curvature in (2.3) and β is the vehicle sideslip.

The final steering angle δ is

$$\delta = \delta_{feedforward} + \delta_{control} + \delta_{damping}.\tag{3.13}$$

Chapter 4

Longitudinal Controller

Similar to the steering controller, the longitudinal controller consists of feedforward and feedback components. The feedforward decides when and how much to accelerate and brake, while the feedback is similar to a driver modulating the throttle and brake to control the slip of the tires and the vehicle speed.

From the block diagram of the complete system in Fig. 2.7, Figure 4.1 depicts the structure of the longitudinal controller in detail. The feedforward longitudinal controller uses the desired speed and acceleration profiles calculated in Section 2.4 to estimate the feedforward longitudinal force. Simultaneously, the vehicle operating conditions, such as road bank and rolling resistance, are used to compensate for the vehicle's drag. The slip circle feedback controls the front and rear wheel slip, while the speed feedback ensures that the vehicle tracks the desired speed while it travels along the path.

4.1 Feedforward longitudinal controller

The goal of the longitudinal feedforward algorithm is to design throttle and brake inputs that mimic a racecar driver trail-braking into a corner and applying the throttle on a corner exit. The feedforward longitudinal controller uses the desired speed $U_x(s)$ and acceleration $a_x(s)$ profiles described in Section 2.4 to make the vehicle's acceleration trace the friction limit in a “ $g-g$ ” diagram.

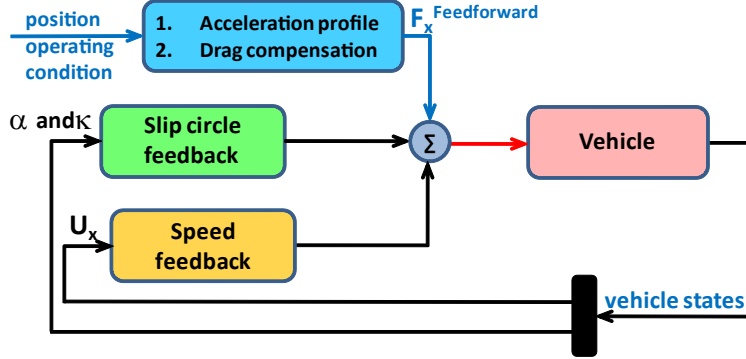


Figure 4.1: An overview of the longitudinal controller

4.1.1 Feedforward longitudinal control from acceleration profile

Once $U_x(s)$ is known, Equation (2.6) is used to find the desired $a_x(s)$ along the path. Thus, from Newton's second law, feedforward longitudinal force along the path $F_x^{FFW}(s)$ can be found from

$$F_x^{FFW}(s) = m a_x(s) . \quad (4.1)$$

4.1.2 Drag compensation

Drag compensation force F_x^{drag} offsets the resistance forces from a vehicle's rolling resistance $F_{rolling}$, aerodynamic force F_{aero} , road grade F_{grade} and the longitudinal component from the front axle turning $F_{turning}$. Without any drag compensation, the vehicle will slow down. The drag from rolling resistance is constant while the effect of aerodynamic drag is proportional to the vehicle speed squared. The rolling resistance (255.57 N) and the drag coefficient ($0.3638 \text{ Ns}^2/\text{m}^2$) were determined from a coasting down test. The Audi TTS was driven up to a certain speed, and the gear was shifted to neutral. While coasting, only drag force resisted the vehicle motion. Thus, the rolling resistance and drag coefficient parameters were deduced from the measured

vehicle speed and the rate of deceleration. The drag compensation is calculated from

$$\begin{aligned}
 F_x^{drag} &= F_{rolling} + F_{aero} + F_{grade} + F_{turning} \\
 F_{rolling} &= 255.57 \\
 F_{aero} &= 0.3638U_x^2 \\
 F_{grade} &= -mg \sin(\theta_{grade}) \\
 F_{turning} &= m \frac{b}{a+b} |\hat{a}_y \tan(\delta)| ,
 \end{aligned} \tag{4.2}$$

where \hat{a}_y is the estimated lateral acceleration calculated from $U_x^2/R(s)$ instead of using the actual a_y to avoid noise from the measurement. The calculation of $F_{turning}$ uses a steady state assumption and assumes that the front lateral force is proportional to the front static normal load.

4.2 Slip circle feedback controller

A longitudinal feedback controller controls front and rear tire slip. It uses a slip circle, which is a combined lateral and longitudinal slip, to fulfil two purposes. First, it provides a longitudinal input that controls tire slip. Even though Section 3.2.2 demonstrates the system stability when operating at the friction limits, the slip circle longitudinal feedback controller further enhances vehicle stability by avoiding rear axle saturation. In addition, controlling front axle slip ensures that sufficient control authority is provided to the steering controller. For instance, when a vehicle is understeering (the front tire is saturated), additional steering no longer provides additional lateral tire force to the vehicle. Thus, the slip circle controller reduces the amount of longitudinal force in order to increase lateral force available to the steering (for four-wheel or front-wheel drive). Second, the slip circle controller ensures that the tires are operating at their limits. If the slip circle controller detects that none of the tires are operating at their limits, it can command additional longitudinal force to utilize the friction.

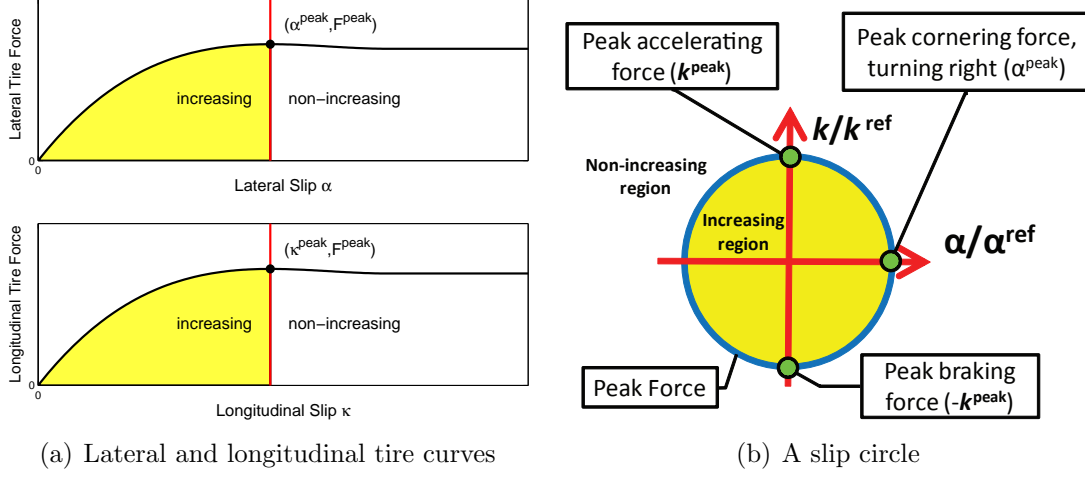


Figure 4.2: Relationship between tire curves and a slip circle

4.2.1 Slip circle concept

Before introducing the idea of combined slip, individual lateral and longitudinal tire curves are shown in Fig. 4.2(a). A lateral tire curve demonstrates how lateral tire slip α generates lateral tire force. The initial slope of the lateral tire curve is the lateral cornering stiffness C used in (3.3). The maximum lateral tire force is achieved when the lateral slip $\alpha = \alpha^{\text{peak}}$, and is equal to the maximum for that the tire can generate.

Similarly, a longitudinal tire curve shows the relationship between the longitudinal tire force and the longitudinal slip κ , which is defined as

$$\kappa = \frac{R_e \omega - V}{V} , \quad (4.3)$$

where ω is the angular velocity of a wheel, R_e is the effective radius of the tire and V is the wheel center's velocity along the tire's longitudinal axis. When only κ is present, the maximum longitudinal force occurs when $\kappa = \kappa^{\text{peak}}$, which corresponds to maximum braking or acceleration.

A slip circle explains the state of the combined longitudinal and lateral tire slip, which can be used as a feedback state for the longitudinal controller. This slip represents how force is distributed between lateral and longitudinal force. By normalizing

lateral slip by $\alpha^{ref} = \alpha^{peak}$ and longitudinal slip by $\kappa^{ref} = \kappa^{peak}$, any point on a unit circle ($\bar{\alpha}^2 + \bar{\kappa}^2 = 1$) in Fig. 4.2(b) produces peak tire force, where normalized quantities $\bar{\alpha}$ and $\bar{\kappa}$ can be defined as

$$\begin{aligned}\bar{\alpha} &= \frac{\alpha}{\alpha^{ref}} \\ \bar{\kappa} &= \frac{\kappa}{\kappa^{ref}}.\end{aligned}\tag{4.4}$$

For instance, $|\bar{\alpha}| = 1$ corresponds to a tire generating peak cornering force while $\bar{\kappa} = -1$ represents a tire generating maximum braking.

A combined slip can be used for estimating the available longitudinal and lateral tire force as described in [67]. To expand this concept, the unit circle in Fig. 4.2(b) can be used to define the tire force boundary between increasing and non-increasing tire force regions. Inside this unit circle, the tire force does not reach its limit and increasing slip increases tire force. However, outside of this unit circle, increasing slip no longer generates additional force. In theory, a racecar driver will try to stay on these unit circles defined for each tire, to obtain maximum tire forces. In practice, due to weight transfer, suspension geometries, etc., it is difficult to be on the unit circle of every tire at once. To provide a fundamental understanding of how this slip circle concept works, we simplify the concept of individual slip circle into front and rear slip circles. The left and right κ of each axle are averaged to create a slip circle of each axle.

In addition, it should be pointed out that there is a fundamental difference between the “ $g-g$ ” diagram in Fig. 2.1(b) and the slip circle in Fig. 4.2(b). A “ $g-g$ ” diagram represents the vehicle’s combined acceleration limits. It is useful to show how close the vehicle is to the limits, but a “ $g-g$ ” diagram does not show when a tire passes its limit. In contrast, a slip circle can detect if a tire is sliding beyond its peak force (outside of a slip circle) or “gripping” (inside of a slip circle) based on the state of the slip relative to the unit circle. Thus, a slip circle is used as a feedback state, while a “ $g-g$ ” diagram is used for calculating desired acceleration and speed profiles.

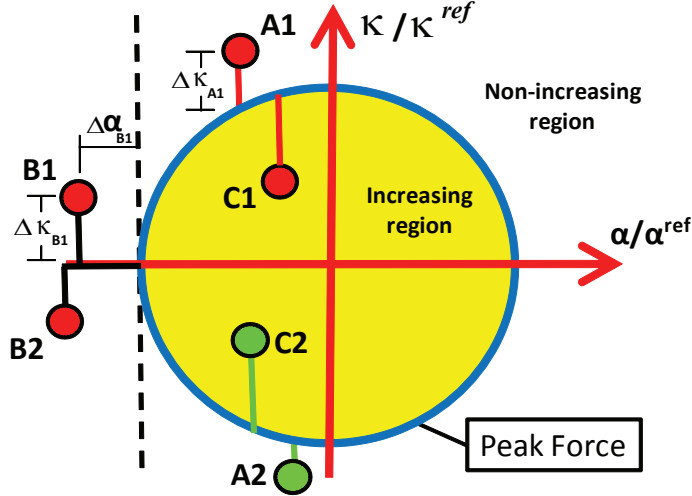


Figure 4.3: Different control scenarios on a slip circle, when $\alpha_{ref} = \alpha_{peak}$

4.2.2 Implementing the slip circle controller

A racecar driver has the ability to control the amount of tire slip to ensure vehicle stability and to operate at the peak tire force. Similarly, the objective of the longitudinal slip circle controller is to track the edge of the unit circle in Fig. 4.2(b). The controller should minimize excessive slip that could cause understeer or oversteer and ensure that the tires are operating close to their peak forces.

To reach the full limits of the vehicle, we have to choose α^{peak} and κ^{peak} to normalize the unit circle in (4.4). In practice, different reference values may be used depending upon the desired vehicle behavior. Since rear axle saturation could cause vehicle instability, different conservative α_{peak} and κ_{peak} values can be chosen to balance between operating at the peak force and minimizing the chances of rear wheel saturation when throttle is applied. For instance, α_f^{ref} was chosen from the peak tire force using a ramp steer maneuver while α_r^{ref} was detuned from the α^{peak} to minimize rear axle sliding. Similarly, κ_f^{ref} and κ_r^{ref} were found experimentally from the peak tire force in a longitudinal tire curve.

To explain how the longitudinal slip circle controller operates in various scenarios, different tire slip conditions shown in Fig. 4.3 are used.

Front or all tires are saturated

When the front axle slip is outside of the unit circle, the slip circle algorithm focuses on controlling the front axle slip. If $|\bar{\alpha}| \leq 1$ (points A1 and A2 in Fig. 4.3), the feedback longitudinal force is proportional to the distance between the slip and the edge of the unit circle (along the $\bar{\kappa}$ -axis). If $|\bar{\alpha}| > 1$ (points B1 and B2), the feedback longitudinal force is proportional to the sum of the distance along the $\bar{\alpha}$ and $\bar{\kappa}$ axes.

$$F_x^{FB} = \begin{cases} k_\kappa \Delta \bar{\kappa} + k_\alpha \Delta \bar{\alpha}, \bar{\kappa} \leq 0 \\ -k_\kappa \Delta \bar{\kappa} - k_\alpha \Delta \bar{\alpha}, \bar{\kappa} > 0 \end{cases} \quad (4.5)$$

where

$$\Delta \bar{\kappa} = \begin{cases} |\bar{\kappa}| - \sqrt{1 - \bar{\alpha}^2}, \bar{\alpha} \leq 1 \\ |\bar{\kappa}|, \bar{\alpha} > 1 \end{cases}$$

$$\Delta \bar{\alpha} = \begin{cases} 0, \bar{\alpha} \leq 1 \\ |\bar{\alpha}| - 1, \bar{\alpha} > 1 \end{cases}$$

k_κ and k_α are the gains of the front longitudinal and lateral slip respectively. These gains were chosen from the controller behavior during the experiment in order to manage the tradeoff between tracking performance and minimizing oscillation due to an excessive gain.

Note that when the front axle slip is at point A2 or B2 in Fig. 4.3, the slip circle commands positive feedback force. This is similar to a racecar driver reducing the amount of braking when the front axle is locking up¹. In contrast, when the front slip is at point A1 or B1, the feedback controller will reduce the amount of throttle, mimicking a racecar driver letting off the throttle to reduce wheel spin.

Notice that with this longitudinal controller, there is no direct control over lateral slip α . Pulling the front slip back into a unit circle becomes a challenge when $|\bar{\alpha}| > 1$.

¹Modulating the longitudinal input influences the longitudinal weight transfer, which will influence tire slip. However, this could have a desirable effect as when the vehicle brakes too much that the rear tires start to slide, reducing the brake increase rear normal force and reduces the amount of slip.

Changing the longitudinal controller input could only have a secondary effect on vehicle speed, which then influences the lateral slip α . Only the front steering input has direct control over front lateral slip α_f .

Only rear tires are saturated

When only the rear axle is sliding (rear slip is outside of the unit circle), equation (4.5) is used with parameters from the rear axle.

None of the tires are saturated

When none of the tires are operating at their peak forces (point C1 or C2 in Fig. 4.3), a racecar driver can adjust the inputs to fully utilize the tire forces. This may be emulated by allowing the controller to increase longitudinal force. For instance, if none of the tires are at the limits during trail-braking, a racecar driver may reduce the amount of brake to allow the vehicle to go faster through a corner. This will increase vehicle cornering speed, which requires additional lateral force, thus a driver increases lateral slip α by letting off the brake. When front and rear slip are inside the unit circle, the slip circle controller applies an additional force of

$$\begin{aligned} F_x^{FB} &= k_{noSlip} \Delta \kappa_{min} \\ \Delta \kappa_{min} &= \min \begin{cases} \sqrt{1 - (\bar{\alpha}_f)^2} - |\bar{\kappa}_f| \\ \sqrt{1 - (\bar{\alpha}_r)^2} - |\bar{\kappa}_r| \end{cases} \end{aligned} \quad (4.6)$$

where k_{noSlip} is the gain when every axle is in the increasing region. The value was found from the experiment and is a tradeoff between tracking the edge of the slip circle and minimizing oscillation in the longitudinal command.

Note that when a vehicle is approaching a corner from a straight section and none of the tires are saturated, the slip circle controller becomes inactive and the longitudinal controller only relies on the feedforward command. A corner entry speed is critical because any excessive speed will require additional lateral force, which the tires may not have during trail-braking. An excessive corner entry speed leads to

vehicle understeer or oversteer during the corner entry. Consequently, rather than allowing the feedback controller to add additional longitudinal force, the vehicle should rely on the feedforward longitudinal command to ensure a correct corner entry speed. Thus, the no-slip gain is only active during cornering.

This feedback gain k_{noSlip} was activated in the experimental results, as shown in Fig. 5.5, 5.6 and 5.15. It was found that using k_{noSlip} without considering the desired speed profile could allow the vehicle speed to increase beyond the entry speed of the following corner (see Section 4.3 and Section 5.3.3). To resolve this problem, this feedback gain k_{noSlip} was not used for further experiments, and the speed tracking in Section 4.3 is used instead.

4.3 Tracking of desired speed profile

As mentioned in Section 2.1.3 and 2.4.2, vehicle speed plays an important role in vehicle control, especially during corner entry. Thus, in order to control the vehicle's lateral acceleration a_y , controlling the vehicle speed U_x becomes critical.

4.3.1 Desired speed profile for a complex map

The desired vehicle speed $U_x(s)$ is calculated from Section 2.4. For a simple oval track, the controller only needs to lookahead one segment in advance to check the entry speed of the following segment. However, this strategy could be problematic when a complex map is used, such as the Pikes Peak map (Fig. 4.4). Such a complex map can have a long sweep curve followed by a tight curve (see Fig. 4.4); thus, the controller would actually have to brake in the long sweep curve ($s=180\text{-}205\text{ m}$ in Fig. 4.5) in order to cope with the tight curve that follows.

The controller would consequently have to look well in advance to ensure that the action of the current segment will not jeopardize the entry speed of the subsequent segments. In the study described here, the controller looks twelve segments in advance² (recall that each segment consists of one type of path, i.e., a constant radius,

²The controller has to look far enough in advance to handle compound curves, but increasing

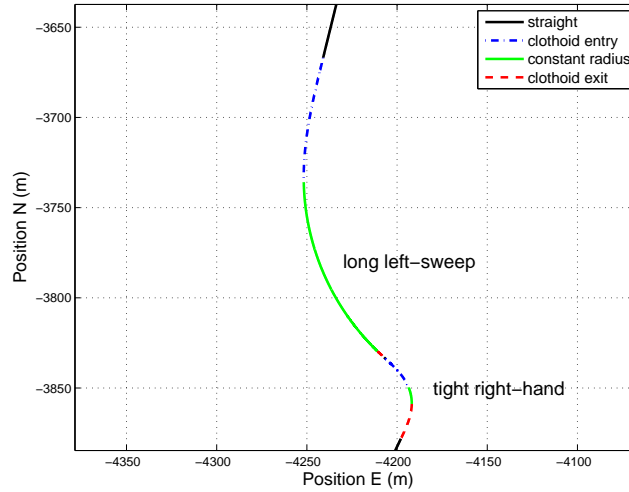


Figure 4.4: A small section of Pikes Peak map, around “ski area”. Note that a long left-sweep is followed immediately by a tight right-hand turn.

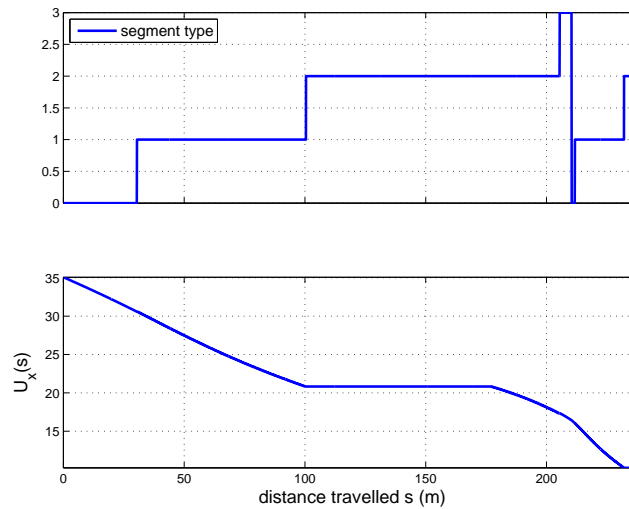


Figure 4.5: The corresponding speed profile for the small section of Pikes Peak map in Fig 4.4 (0=straight, 1=corner entry, 2=constant radius and 3=corner exit).

a straight, or a clothoid). The algorithm calculates the entry speed of the twelfth segment and works backward to the current segment.

4.3.2 Speed feedback

In order to track a desired speed profile, proportional speed feedback is used

$$F_x^{speedFB} = k_{speed}(U_x(s) - U_x) , \quad (4.7)$$

where k_{speed} is the speed feedback gain, and the method of choosing this gain is discussed in Section 5.4.1. The speed tracking is active all the time, unless the slip circle detects that the combined slip of either front or rear axles are outside their slip circles. In this situation, the slip circle feedback remains active, while the speed feedback is temporarily inactive to prevent the controllers from working against each other.

4.4 Total longitudinal force

The total longitudinal force F_x is the combination of the feedforward longitudinal force calculated from the speed and acceleration profiles (Section 4.1.1), the drag compensation (Section 4.1.2), the slip circle feedback (Section 4.2) and the speed feedback (Section 4.3). The longitudinal force command F_x is therefore

$$\begin{aligned} F_x = & F_x^{FFW} + F_x^{drag} \\ & + F_x^{FB} + F_x^{speedFB} . \end{aligned} \quad (4.8)$$

If the total longitudinal force is positive, the force is converted to throttle position via an engine map. On the other hand, if the total longitudinal force is negative, the force is converted to either throttle position that will produce engine brake using an engine map or a commanded brake pressure using a lookup table.

number of lookahead segments will increase the controller's computation time.

Chapter 5

Experimental Results

This chapter explains the performance of the autonomous racing controller described in Chapters 2 through 4. The experimental results are divided into three sections, with each section corresponding to a different testing surface. Section 5.2 discusses the results when the controller was first used on a rough dirt surface. Although the controller in this initial experiment was still under development, the results give an overview of how the controller reacts when the vehicle oversteers and understeers. Section 5.3 then discusses how the controller was tested at high speed on a salt surface. These results provide a detailed explanation of how the controller operates during cornering. The results on this surface also show that the controller can track a friction limit circle very well while maintaining a minimal tracking error. Section 5.3 also explores the effects of no-slip gain k_{noSlip} and the drawbacks associated with it. Section 5.4 discusses the controller's performance on a paved surface. Although its performance on a paved surface is comparable to the results on a salt surface, the results on a paved surface highlight the importance of speed tracking. This speed tracking performance is addressed in Section 5.4.1.

Before the experimental results are discussed in detail, the following section describes the vehicle and equipment used in testing.

5.1 Experimental setup

We use a four-wheel drive Audi TTS named “Shelley” (see Fig. 5.1 and 5.7). A detailed description of this Audi can be found in Appendix B. The Audi TTS has a production electric power steering motor, an active brake booster and an electronic throttle that were modified to receive commands from the controller. The vehicle is equipped with a Differential Global Positioning System (DGPS) and Inertial Navigation System (INS), from which vehicle position and other states are obtained. A map matching algorithm [66] utilizes the information from the DGPS/INS system to find the vehicle’s path tracking errors, such as lateral error e and heading error $\Delta\psi$ in Fig. 3.4(a). These tracking states, measured relative to the desired path, are used for calculating steering feedback input in (3.10). The wheel speed measurements and the measured vehicle speed from the GPS are used to calculate the longitudinal slip in (4.3). Because front and rear longitudinal slip tend to have high frequency noise from the wheel speed measurements, moving average filters with fifty samples, equally weighted, are used to smooth the measurements. The sampling rate of the controller is 200 Hz.

5.2 Experimental results on a dirt surface

The Audi TTS was first tested on a dirt surface at Santa Clara County Fairgrounds, Santa Clara, California (Fig. 5.1). The results, discussed in this section, reflect an early version of this controller in its first use on an actual production vehicle. Thus, some of the gains had not yet been refined, as well as the effect of weight transfer discussed in Section 2.4.5, the yaw damping discussed in Section 3.2.3 and the speed tracking discussed in Section 4.3 were not used on this surface. Nevertheless, the results obtained on a dirt surface, which has high surface roughness and high friction variation, demonstrate how the controller behaves when operating under and over the friction limits.

Table 5.1 displays the gains used on the dirt surface. Although intuitively it seems appropriate to choose α_{peak} and κ_{peak} to normalize the unit circle in (4.4), in



Figure 5.1: Autonomous Audi TTS on a dirt surface at Santa Clara County Fair-grounds, Santa Clara, CA

practice, a lower reference value κ_{ref}^{rear} was used. Since rear axle sliding could cause vehicle instability, different levels of conservatism can be chosen to balance between operating at the peak force and minimizing the rear wheels' slide when throttle is applied. The constants α_{ref}^{front} and α_{ref}^{rear} were found experimentally from the peak tire force using a ramp steer maneuver. These values were then tuned according to the behaviors of the system. For instance, if the vehicle was oversteering, then a lower α_{ref}^{rear} was used. The final values of α_{ref}^{front} and α_{ref}^{rear} are shown in Table 5.1. Similarly, κ_{ref}^{front} was chosen from the peak tire force in a longitudinal tire curve. The constant κ_{ref}^{rear} was detuned from the κ_{peak} to minimize rear axle sliding.

Front and rear tire curves were fitted to the ramp steer data (see Fig. 5.2) to determine the friction coefficients and the front and rear cornering stiffness values in Table 5.1. Different fitted tire curves from three different surfaces are also shown in Fig. 5.3, which indicates that higher friction surface generates higher cornering stiffness values.

The controller drives the Audi TTS autonomously around a left-handed oval map (see Fig. 5.4) on a rough dirt surface. A section that consists of one straight and one 180 degree (hairpin) turn was used for the analysis. Figure 5.5a and 5.5b show the steering and longitudinal controller inputs, respectively, both of which consist of feedforward and feedback commands. The front and rear tire slip are depicted in

Table 5.1: Controller gains and parameters for dirt surface

estimated friction value	μ	0.5	
front cornering stiffness	C_f	50,000	N/rad
rear cornering stiffness	C_r	50,000	N/rad
including weight transfer		no	
<i>steering controller</i>			
lanekeeping gain	k_p	3,500	N/m
lookahead distance	x_{la}	15.3	m
yaw damping gain	$k_{\Delta\psi}$	0	s
<i>longitudinal controller</i>			
front axle lateral slip	α_f^{ref}	8	deg
limited front axle lateral slip	α_f^{lim}	12	deg
rear axle lateral slip	α_r^{ref}	8	deg
front axle longitudinal slip	κ_{front}^{ref}	.2	
rear axle longitudinal slip	κ_{rear}^{ref}	.1	
kappa front slip gain	k_κ^f	2,000	N
alpha front slip gain	k_α^f	2,000	N
kappa rear slip gain	k_κ^r	1,000	N
alpha rear slip gain	k_α^r	1,000	N
no-slip gain	k_{noSlip}	4,000	N
speed gain	k_{speed}	2,000 ^a	Ns/m

^aonly active on the straight and clothoid entry section

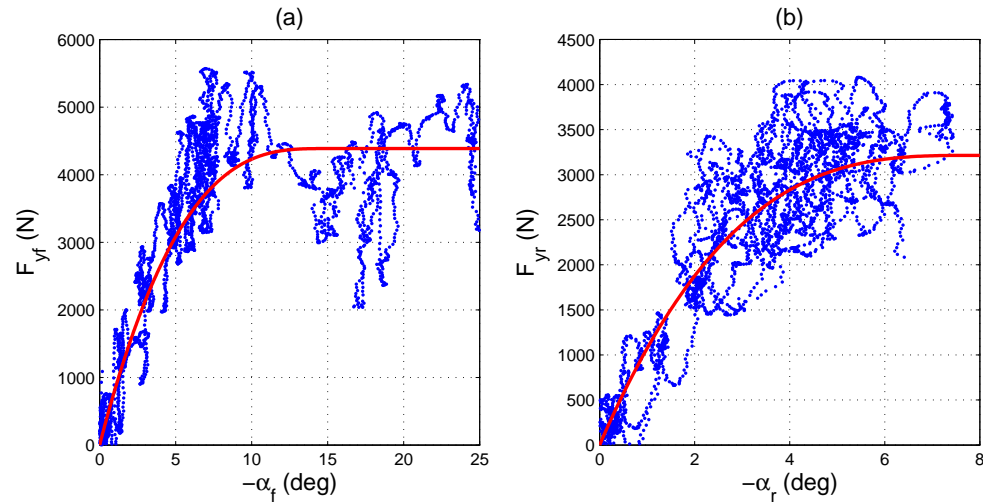


Figure 5.2: Front (a) and rear (b) tire curves fitted to the ramp steer data, on a dirt surface

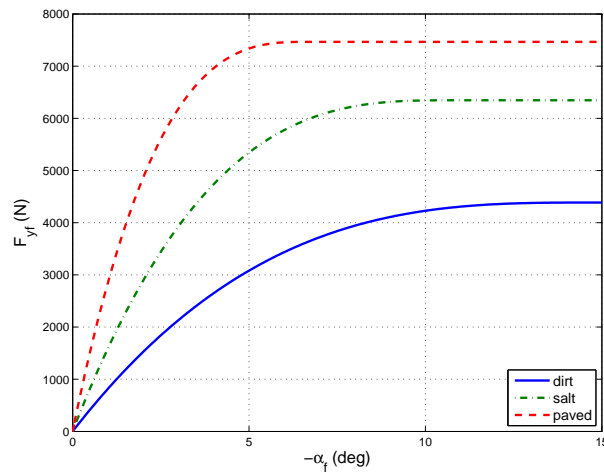


Figure 5.3: Comparison of three tire curves from different testing surfaces

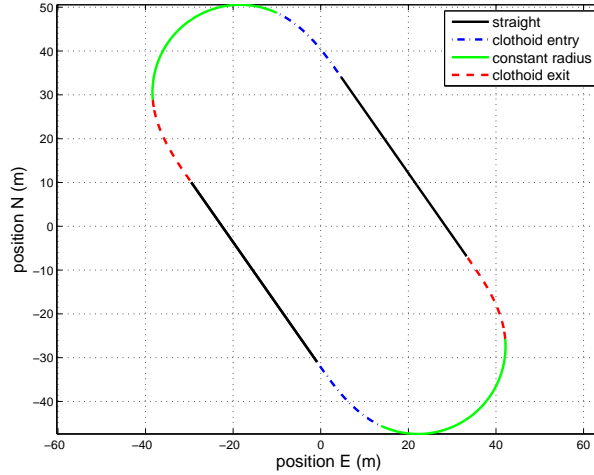


Figure 5.4: Map used on a dirt surface, plotting on North and East coordinates

Fig. 5.5c to 5.5e. The slip norm $|slip| = \sqrt{\bar{\alpha}^2 + \bar{\kappa}^2}$ in Fig. 5.5e is effectively the sum of lateral and longitudinal normalized slip, i.e., the radius of the slip circle. Vehicle states are displayed in Fig. 5.5f to 5.5h. The oscillation in the vehicle states was due to the lack of yaw damping in the system combined with the large friction variation and surface roughness of the testing surface.

Operation under the limits

The feedforward longitudinal command, calculated from the desired path and the friction value, is shown in Fig. 5.5b. The results in Fig. 5.5 demonstrate the slip circle controller's ability to increase longitudinal force to utilize the tire force. During the mid corner section (68.3-69.1 s, see the longitudinal commands in Fig. 5.5b), the longitudinal feedback controller detects that none of the tires are saturated, since $|slip| < 1$ (see Fig. 5.5e). Thus, the controller commands additional force. Similarly, during an early part of trail-braking (66-67 s) and a later part of throttle-on-exit (71.8-72.9 s), the slip circle controller detects that the tires are not at their limits and provides additional feedback force to increase vehicle speed.

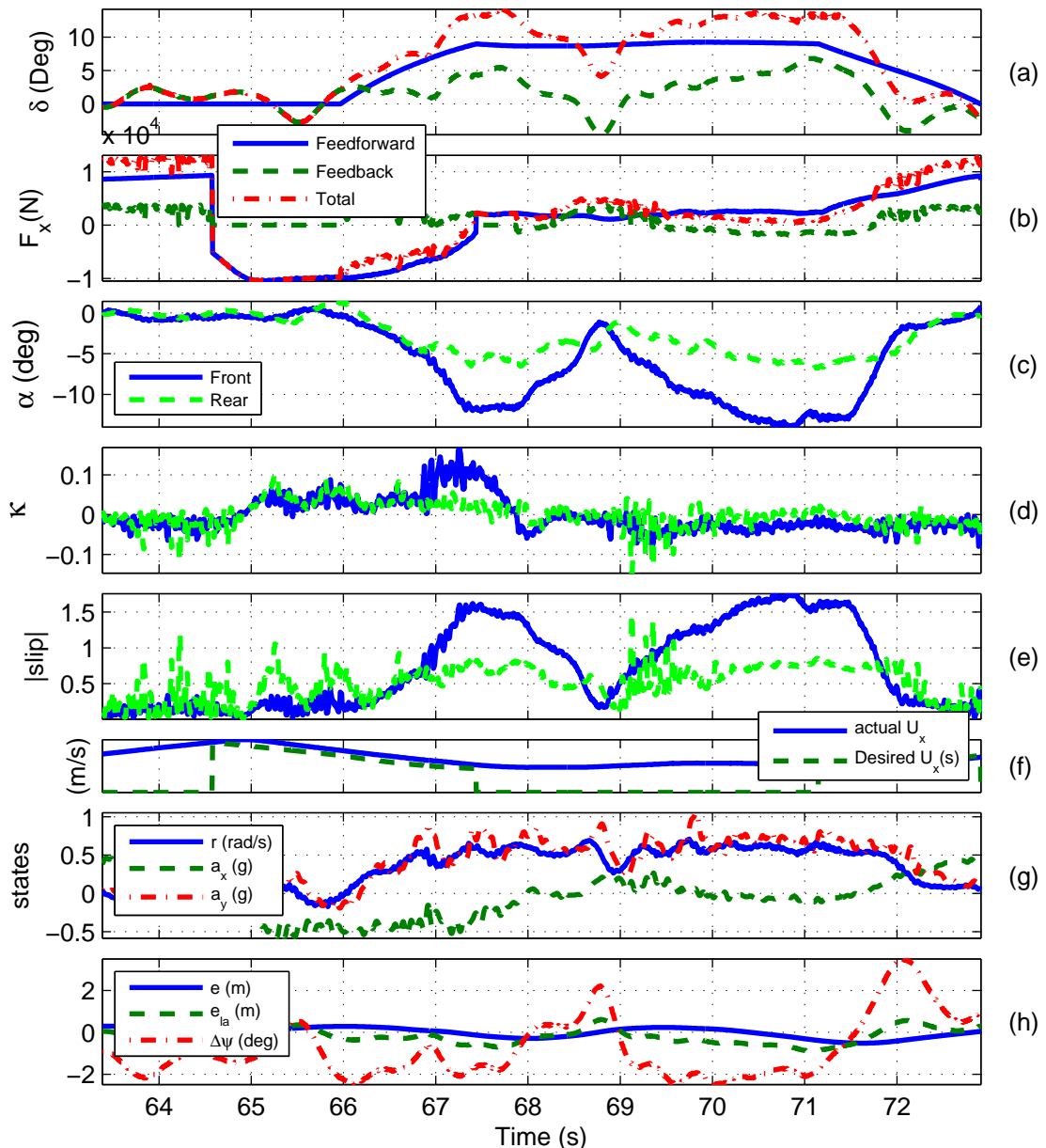


Figure 5.5: Controller commands (a-b) and vehicle states (c-h) on dirt surface, with no-slip gain. Feedback force in Figure b only shows slip circle controller command.

Operation when understeering

As shown in Fig. 5.5b, the longitudinal slip circle feedback controller controls the amount of tire slip (Fig. 5.5e). During 69.5-71.7 s, the controller detects that the front axle is sliding, because the slip norm is greater than 1. Consequently, the slip circle controller reduces the longitudinal force to control the slide (see $F_x^{feedback}$ in Fig. 5.5b). Reducing the front longitudinal slip provides additional lateral force to the steering controller and allows the vehicle to regain tracking ability.

Similarly, at the end of trail-braking (corner entry, 67-67.5 s in Fig. 5.5), the slip circle controller commands positive force when a large slip is observed at the front axle. This large slip is caused by turning and braking at once. The controller reduces the amount of brake (thus, reducing the amount of longitudinal slip) in order to provide additional lateral force for turning. This front axle slip is similar to the point B2 in Fig. 4.3.

The front lateral slip limit α^{lim} (12 deg) was chosen to be higher than α_{ref} (8 deg) to decouple the slip circle controller from the steering controller. If these two values are the same, the steering controller will limit the amount of steering, and α_{front} will never exceed α_{ref} (from $\alpha^{lim} = \alpha_{ref}$). A higher α^{lim} will ensure that the slip circle controller will slow the vehicle down before α_{front} hits α^{lim} .

Operation when oversteering

The slip circle longitudinal controller also controls the amount of rear slip to avoid instability from the rear axle sliding. The vehicle oversteers during 68.6-69 s because the rear lateral slip becomes larger than the front lateral slip in Fig. 5.5c. To maintain yaw stability, the controller countersteers (see feedback steering in Fig. 5.5a).

During 69-69.4 s, the longitudinal rear slip κ_r exceeds the reference value of 0.1, indicating that the rear tires lose traction due to an excessive feedforward longitudinal command. The slip circle detects this excessive slip and reduces the amount of throttle input.

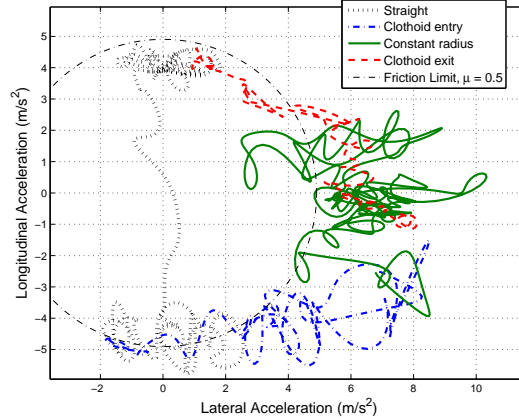


Figure 5.6: “*g-g*” diagram from Audi TTS on dirt surface

5.2.1 “*g-g*” diagram on a dirt surface

Figure 5.6 shows the vehicle’s acceleration on a “*g-g*” diagram. Although the controller used an estimated friction value of 0.5, the actual vehicle’s acceleration was higher than 0.5. There are two reasons for this: first, the no-slip gain k_{noSlip} was used; thus, when the controller sensed that none of the tires were operating at their limits, it increased the vehicle speed, which effectively increased the vehicle’s lateral acceleration. Second, because the speed tracking was not used in this early stage of development, the actual vehicle speed was higher than the desired speed (Fig. 5.5f). This higher speed causes the vehicle’s acceleration to peak around $0.65g$. For an oval track, using the no-slip gain without monitoring the vehicle speed does not cause any problems because every corner is followed by a straight segment. However, if a complex map that has two consecutive curves is used, using the no-slip gain without monitoring the vehicle’s speed could cause a vehicle to slide in the subsequent corner because the no-slip gain increases the vehicle speed beyond the desired corner entry speed of the subsequent corner.

If an accurate friction value is known, the vehicle will trace along the friction limit circle, as shown in the “*g-g*” diagram (Fig. 5.6). Nevertheless, the slip circle longitudinal controller senses the available friction and provides additional longitudinal force to increase speed and utilize the friction.

Even on a rough dirt surface, the controller drives the Audi TTS autonomously to its limits without losing control, while having a lateral tracking error e of less than 0.5 m. The lateral slip in Fig. 5.5c also indicates that the tires operate close to their limits, as a ramp steer maneuver indicates that $\alpha_{peak} \approx 8$ deg (Fig. 5.2). These initial experimental results also highlight the need for additional yaw damping in the controller. There is a low frequency oscillation that appears in the lookahead error (e_{la}), yaw rate, and lateral acceleration in Fig. 5.5g, 5.5h and 5.6 that can be minimized by adding yaw damping. Weight transfer, which potentially causes oversteering during corner entry, was not included in the rough dirt experiment. The results in the following sections explain how yaw damping and adding weight transfer improve the controller performance.

5.3 Experimental results on a salt surface

To analyze the controller performance at high speed, the Audi TTS was tested at Bonneville Salt Flats in Utah where the vehicle ran autonomously at 100 mph (Fig. 5.7) around a left-hand oval track (Fig. 5.8). The front and rear tire curves fitted to the ramp steer data on this salt surface are shown in Fig. 5.9 and the tire parameters are summarized in Table 5.2. The controller gains shown in Table 5.2 were fine tuned to obtain good tracking results on a salt surface. To demonstrate how the algorithm controls the vehicle, the controller's behavior is explained segment by segment during each cornering stage. The effects of no-slip gain k_{noSlip} and yaw damping were also investigated.

5.3.1 Overall controller performance

Figure 5.10 provides an overview of how the controller performs on a high speed oval track. The results while driving around the south corner, shown in Fig. 5.8, are divided into four segments: straight, corner entry, constant radius and corner exit. This follows the path structure discussed in Section 2.3.1. The no-slip gain k_{noSlip} was deactivated to explore the performance of the feedforward longitudinal controller,



Figure 5.7: Autonomous Audi TTS at Bonneville Salt Flats, Utah

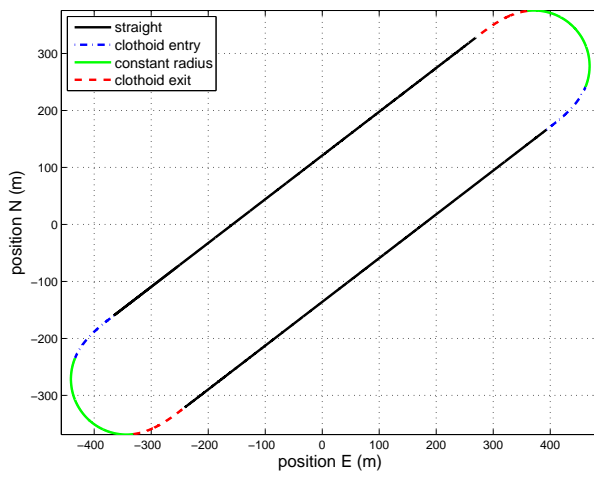


Figure 5.8: Map used on a salt surface, plotting on North and East coordinates

Table 5.2: Controller gains and parameters for Bonneville Salt Flats

estimated friction value	μ	0.5	
front cornering stiffness	C_f	130,000	N/rad
rear cornering stiffness	C_r	140,000	N/rad
including weight transfer		yes	
<i>steering controller</i>			
lanekeeping gain	k_p	3,500	N/m
lookahead distance	x_{la}	20	m
yaw damping gain	$k_{\Delta\dot{\psi}}$.1	s
<i>longitudinal controller</i>			
front axle lateral slip	α_f^{ref}	7	deg
limited front axle lateral slip	α_f^{lim}	12	deg
rear axle lateral slip	α_r^{ref}	5	deg
front axle longitudinal slip	κ_{front}^{ref}	.1	
rear axle longitudinal slip	κ_{rear}^{ref}	.1	
kappa front slip gain	k_κ^f	3,000	N
alpha front slip gain	k_α^f	2,000	N
kappa rear slip gain	k_κ^r	3,000	N
alpha rear slip gain	k_α^r	2,000	N
no-slip gain	k_{noSlip}	N/A ^a	N
speed gain	k_{speed}	2,000 ^b	Ns/m

^athe no-slip gain k_{noSlip} is used only in Section 5.3.3

^bonly active on the straight and clothoid entry section

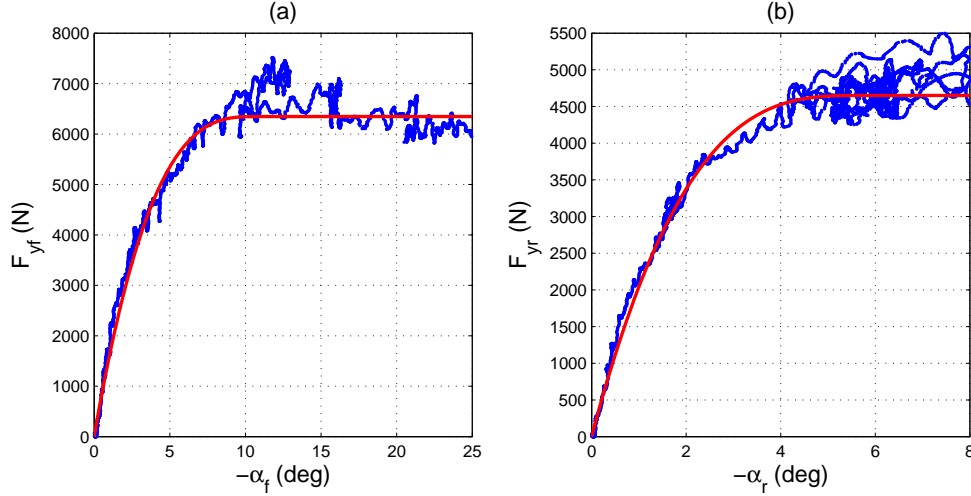


Figure 5.9: Front (a) and rear (b) tire curves fitted to the ramp steer data, on a salt surface

which also takes the effect of weight transfer into account.

Straight: $t = 67.6 - 71.1 \text{ s}$

The vehicle transitions from full throttle to full braking, as shown in Fig. 5.10b, when the distance to the corner entry satisfies (2.10) at $t = 68.5 \text{ s}$. During braking, the longitudinal slip κ illustrated in Fig. 5.10d is negative to generate braking force and the longitudinal acceleration (Fig. 5.10g) is approximately equal to $-0.5g$.

Corner entry: $t = 71.1 - 75.1 \text{ s}$

During this transient phase, the controller trail-brakes by gradually releasing the brake (see Fig. 5.10b), while the feedforward steering increases the steering angle (see Fig. 5.10a). Although the lateral slip α increases and the longitudinal slip κ decreases, as shown in Fig. 5.10c and 5.10d, the magnitude of the combined slip ($|slip| = \sqrt{\bar{\alpha}^2 + \bar{\kappa}^2}$) in Fig. 5.10e is approximately constant.

Note that, as Fig. 5.10a shows, the lanekeeping steering feedback commands additional steering throughout the corner. This is expected because a linear tire model

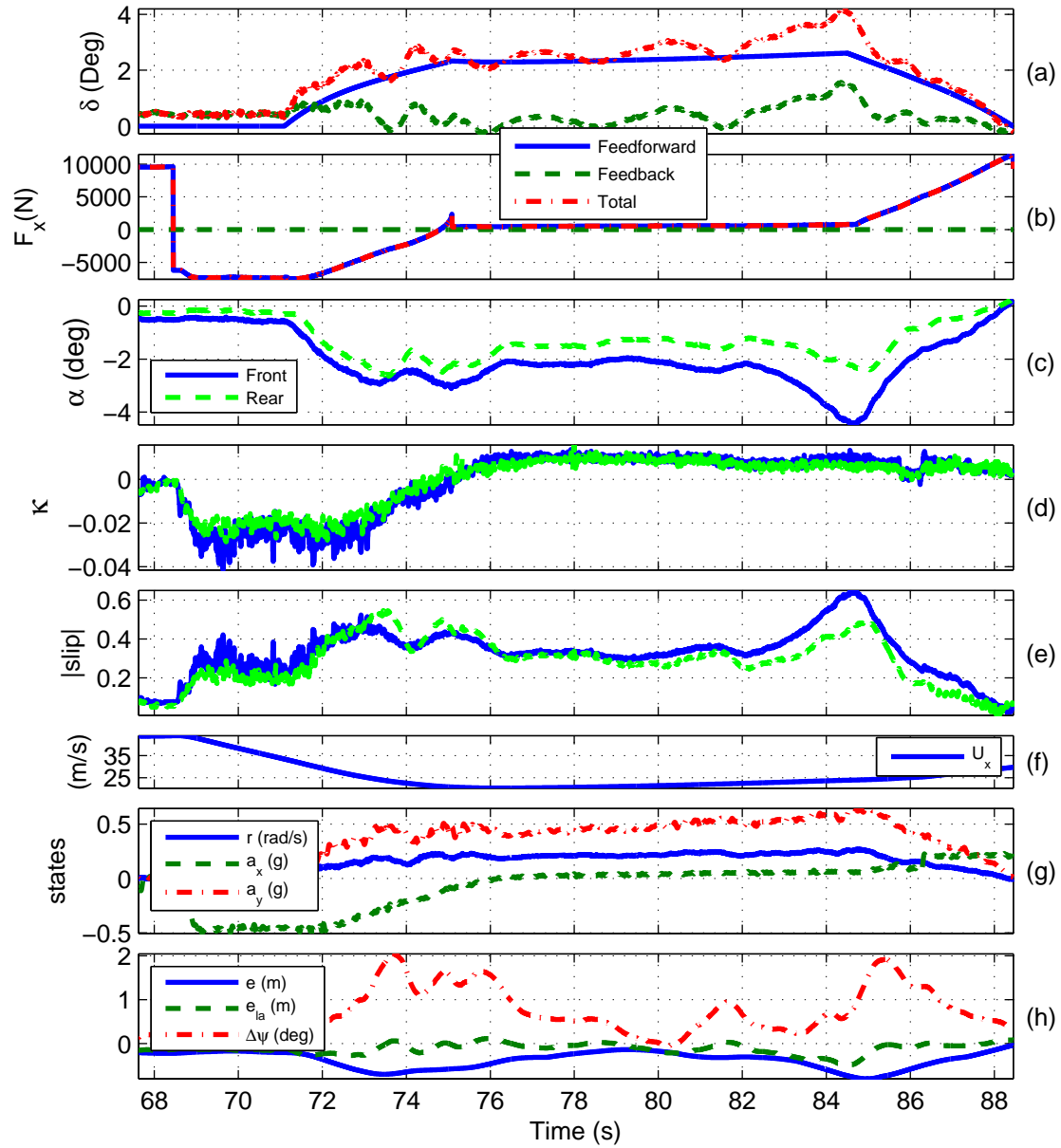


Figure 5.10: Controller commands (a-b) and vehicle states (c-h) on salt surface, with zero no-slip gain. Feedback force in Figure b only shows slip circle controller command.

was used in the feedforward steering calculation. Since the experimental vehicle has an inherent limit understeer characteristic, additional steering is required when cornering at high lateral acceleration, as shown in Fig. 3.3. Chapter 6 will discuss how to incorporate this tire's nonlinearity into the algorithm, to minimize the effect of modeling error and enable the lanekeeping steering feedback to apply only small trims to the steering.

Constant radius: $t = 75.1 - 84.5 \text{ s}$

At this point in the maneuver, all of the feedforward commands (Fig. 5.10a and 5.10b) are relatively constant. The lanekeeping steering feedback (Fig. 5.10a) makes small corrections to minimize the lookahead error e_{la} (Fig. 5.10h). Note that the no-slip gain k_{noSlip} is set to zero (Figs. 5.10–5.12) to investigate the effectiveness of the feedforward longitudinal controller. Since the front and rear tire slip are both inside the unit slip circle and the no-slip gain is off, the slip circle feedback command is zero, as displayed in Fig. 5.10b. The slight speed increase in Fig. 5.10f is a result of overcompensating for the vehicle's drag.

Corner exit: $t = 84.5 - 88.5 \text{ s}$

The controller applies throttle-on-exit. It progressively increases the throttle while unwinding the steering, as shown in Fig. 5.10a. A small dip in the longitudinal slip κ around $t = 86 \text{ s}$ (Fig. 5.10d) indicates clutch disengagement from the Direct-Shift Gearbox (DSG). This consequently creates a small drop in the longitudinal acceleration (Fig. 5.10g).

While the vehicle is driving at its predicted friction limits, it still maintains good tracking performance. The lookahead error e_{la} in Fig. 5.10h, which is the state that the lanekeeping tries to track, remains within 0.5 m. The lateral error e , which is a by-product of controlling e_{la} , stays within 0.8 m throughout the corner.

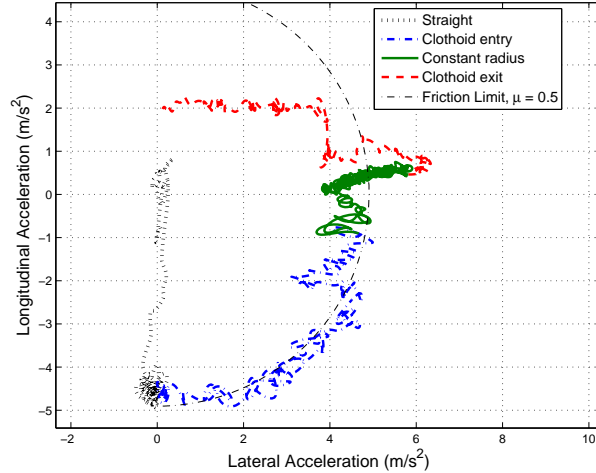


Figure 5.11: “*g-g*” diagram from Audi TTS on salt surface, with zero no-slip gain k_{noSlip}

“*g-g*” diagram on a salt surface

Figure 5.11 shows the effectiveness of the feedforward longitudinal controller when the no-slip gain is inactive. The goal of the feedforward longitudinal controller is to design a longitudinal force command (brake and throttle input) that will make the vehicle’s acceleration trace the friction limit circle ($\mu g = 0.5g$) on a “*g-g*” diagram. Figure 5.11 shows that the vehicle’s acceleration traces the friction limit circle very well, up to the engine’s power limit. The dip in the clothoid exit around $a_y = 4$ and $a_x = 1 \text{ m/s}^2$ corresponds to the gearshift mentioned previously.

5.3.2 Performance with over-estimated friction

This section shows how the same controller with the same parameters performs on a different corner of the same oval (north corner in Fig. 5.8). Figure 5.12 demonstrates the robustness of the controller and how it reacts when the actual friction coefficient is lower than the predicted value ($\mu = 0.5$). Although the vehicle oversteers during 33.8-35.2 s and understeers during 44-45 s (from $|slip| > 1$), the vehicle remains stable as described below.

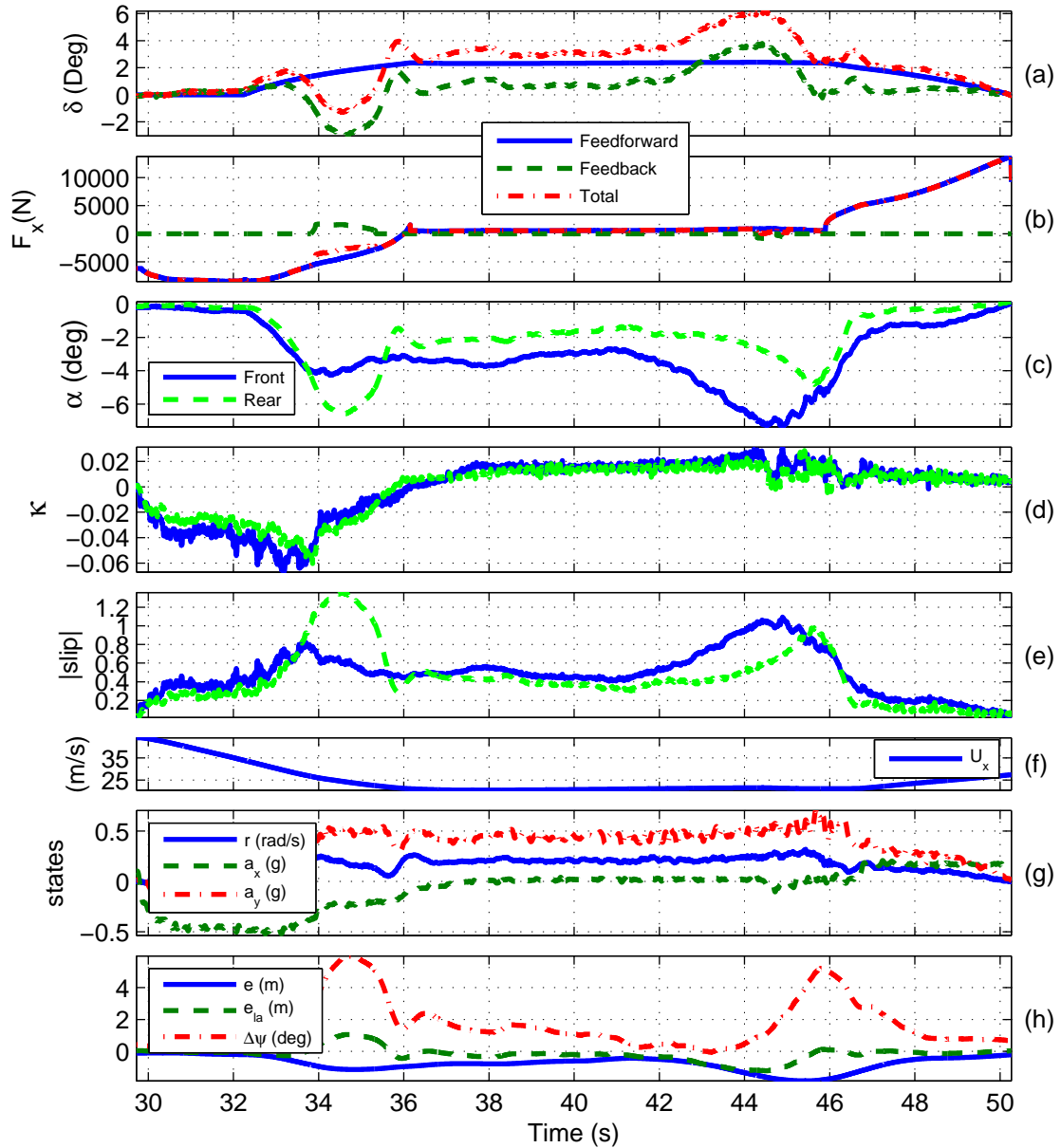


Figure 5.12: Controller commands (a-b) and vehicle states (c-h) on salt surface when the actual friction is less than the predicted value, with zero no-slip gain. Feedback force in Figure b only shows slip circle controller command.

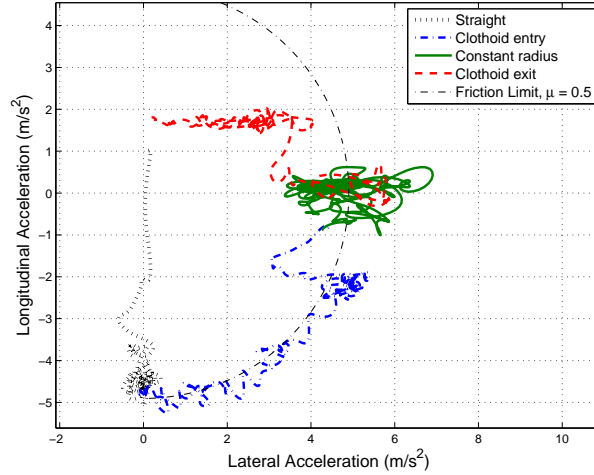


Figure 5.13: “*g-g*” diagram from Audi TTS on salt surface, when over the limits. Note that no-slip gain k_{noSlip} is set to zero

Correcting oversteer

During the corner entry from 32.2–36.1 s, the vehicle is trail-braking into the corner. The rear slip starts to grow due to a combination of the brake force and the weight transfer, which reduces the normal force on the rear axle. Since the predicted friction value is too large, the slip norm of the rear axle in Fig. 5.12e and Fig. 5.14b grows outside of the slip circle ($|slip|_r > 1$). The longitudinal slip circle feedback controller reduces the amount of braking force (see Fig. 5.12b) to allow the rear axle to regain grip. At the same time, the lanekeeping steering controller countersteers and ensures stability of the system. Consequently, the rear slip norm $|slip|_r$ slowly drifts back into the unit circle as depicted in Fig. 5.14b.

The saturation of the rear tires causes the lateral error e and lookahead error e_{la} to grow as shown in Fig. 5.12h, but the vehicle remains stable. In addition, since the controller has to make adjustments in the steering and longitudinal inputs when the vehicle is oversteering at the end of clothoid entry, the vehicle’s acceleration no longer traces the friction limit circle as shown in Fig. 5.13 (at the end of clothoid entry). Thus, anytime the controller has to make significant corrections for oversteering, the vehicle’s acceleration can no longer trace the friction limit circle on a “*g-g*” diagram.

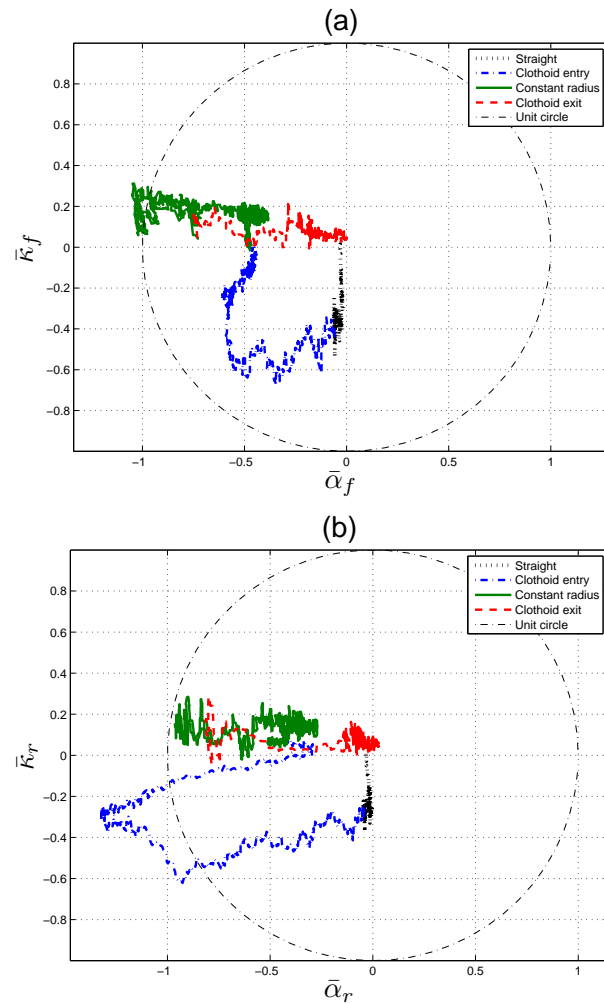


Figure 5.14: Front (a) and rear (b) combined slip on salt surface when over the limits. Note that no-slip gain k_{noSlip} is set to zero

Correcting understeer

During the end of the constant radius turn (36.1 – 45.9 s), the vehicle speed slowly increases (Fig. 5.12f). This is due to the longitudinal controller overcompensating for drag force. Although the increase in speed is minimal, the vehicle is already close to its limits and thus this excessive speed is sufficient to cause the vehicle to understeer ($|slip|_f > 1$ in Fig. 5.12e and 5.14a). This results in increasing tracking error in both e and e_{la} , as demonstrated in Fig. 5.12h. Since the front axle is already saturated, any additional steering does not improve tracking performance. Thus, in this scenario, the controller reduces the amount of throttle (see Fig. 5.12b) to pull the front combined slip back into the unit circle (see Fig. 5.14a). As a consequence, the controller reduces the understeering through minimizing front slip, which in turns improves the tracking performance.

Note that modulating the longitudinal input only has direct control over longitudinal slip κ , i.e. along the $\bar{\kappa}$ -axis in Fig. 4.3. When heavy understeer occurs ($\bar{\alpha} > 1$), controlling longitudinal slip is not sufficient to bring the wheel slip back into a unit circle. A steering input is required to move the lateral slip α back into the unit circle. One potential future improvement is to coordinate steering and throttle inputs to ensure that wheel slip can be moved back into the unit circle from both the longitudinal and lateral directions.

At the corner exit during 45.9 – 50.2 s, since the vehicle has recovered from understeering in the constant radius section, the tracking performance improves as both e and e_{la} reduce to zero in Fig. 5.12h.

The results demonstrate the robustness of lanekeeping and how the racing controller can drive a vehicle to its limits. Nevertheless, the results between Fig. 5.10 and 5.12 show how friction varies along the oval track surface. Although the controller can handle over-predicted friction values, the tracking performance degrades noticeably. This emphasizes the potential advantage of having a correct estimated friction by including realtime friction estimation.

5.3.3 Effect of no-slip gain k_{noSlip}

With the no-slip gain k_{noSlip} turned on in Fig. 5.15e, during the constant radius section (33.8 – 38.6 s, north corner in Fig. 5.8), the slip circle detects that none of the tires are at their limits (from $|slip| < 1$) and starts applying additional longitudinal force. This causes the vehicle speed to increase, see Fig. 5.15f. Eventually, this excessive speed requires additional lateral force to maintain vehicle lateral motion. Due to limited friction, this could cause the vehicle to understeer or oversteer, depending on the vehicle characteristic. In Fig. 5.15c, the rear tires can no longer generate any additional lateral force, causing excessive rear axle sliding (oversteer). Although this overshoot in the slip could be minimized by reducing the no-slip gain, a different method that tracks the vehicle’s speed profile is employed in Section 5.4 because of the following reasons.

Using the no-slip gain k_{noSlip} without tracking the desired speed could cause a problem when a series of curves are linked together. The increase in vehicle speed from the no-slip gain k_{noSlip} in one corner can cause the vehicle to enter a subsequent corner at an excessive entry speed, which could cause the vehicle to slide. Consequently, from Section 5.4 onward, rather than using the no-slip gain k_{noSlip} to adjust the vehicle speed, the vehicle tracks the desired velocity profile derived from the desired trajectory and the estimated friction value.

As shown in Fig. 5.15, slightly excessive speed during a constant radius turn could cause the vehicle to understeer. Thus, the speed tracking in Section 4.3 is implemented in the results in Section 5.4 to ensure that the vehicle’s speed tracks the desired speed profile.

5.3.4 Effectiveness of yaw damping

Figure 5.15 shows how the controller performs without steering yaw damping in Section 3.2.3, at the north corner in Fig. 5.8. Without steering yaw damping, the system dynamics include only the intrinsic damping of the tires, which decreases as the tires approach their limits. This in turn creates an oscillation in the vehicle states, especially yaw motion. This unnecessary yaw motion is undesirable since it requires

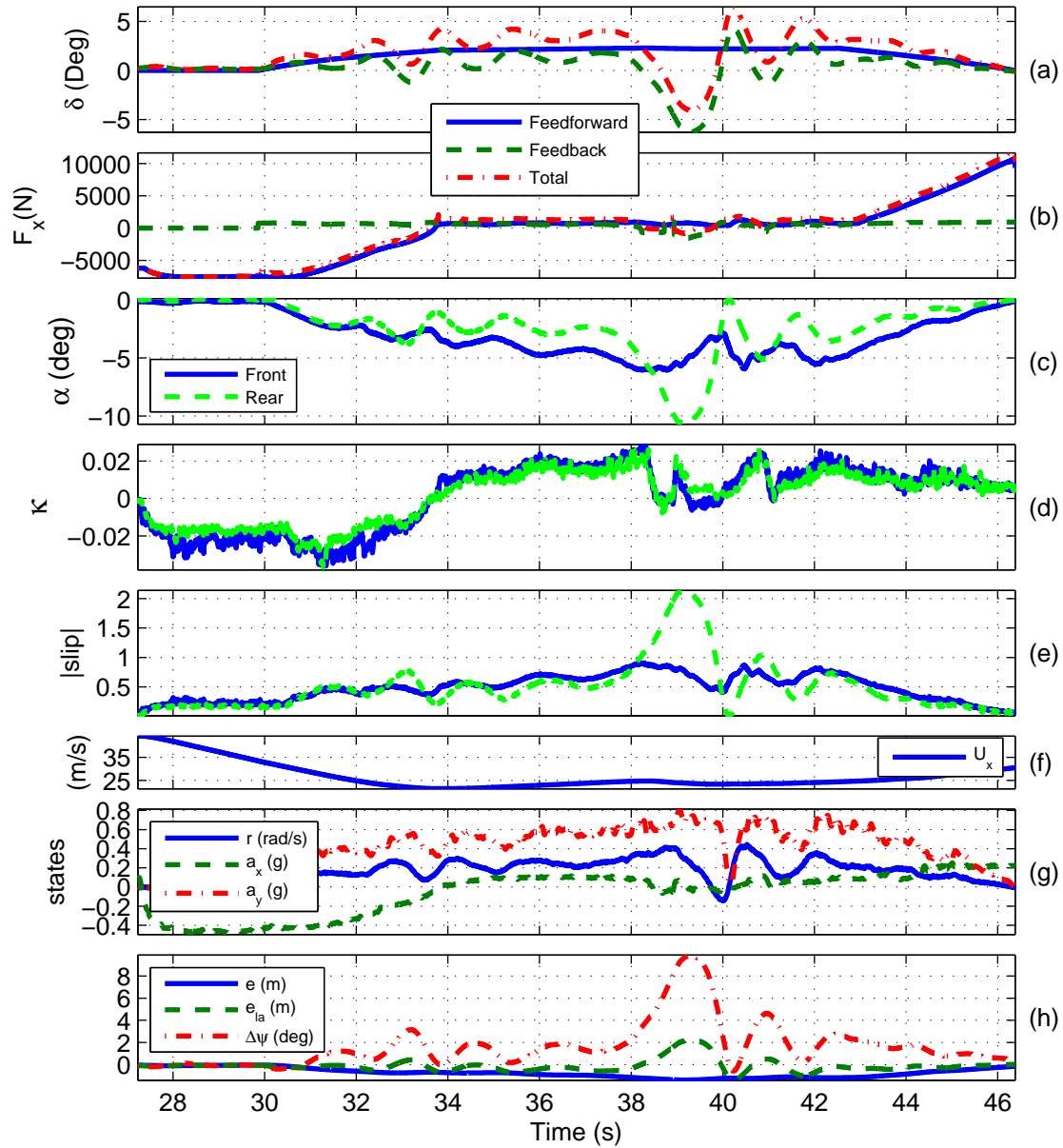


Figure 5.15: Controller commands (a-b) and vehicle states (c-h) on salt surface. Without yaw damping and with no-slip gain, at north corner in Fig. 5.8

additional lateral tire force, which is not necessarily available when the vehicle is operating at its limits. After adding yaw damping (Fig. 5.10 and 5.12), the oscillation in the vehicle states is significantly reduced, demonstrating the effectiveness of injecting yaw damping to compensate for tire saturation. Chapter 6 will discuss how the concept of yaw damping is formulated analytically and how it fits into the steering controller structure.

5.4 Experimental results on a paved surface

The controller was run on a paved surface at Santa Clara County Fairground parking lot, using a left-hand oval map with very short constant radius sections (Fig. 5.16). Although the surface is paved, there are many areas that have patches of gravel, which create friction variation on the surface. The tire curves fitted to ramp steer data are shown in Fig. 5.17 and the tire parameters are summarized in Table 5.3. The controller gains in Table 5.3 are very similar to the gains shown in Table 5.2. However, the front and rear lateral slip α_f^{ref} and α_r^{ref} were reduced as the lateral tire slip tends to be lower on a paved surface (see Fig. 5.3). The results in this section highlight the importance of speed tracking, which will be discussed in Section 5.4.1.

Figure 5.18 and 5.20 show that the controller still tracks the path at the limits while maintaining minimal tracking error. There are oscillations in the vehicle states in Fig. 5.18c and 5.18g, which can be minimized by increasing the yaw damping gain.

In Fig. 5.18e, the slip norm $|slip| < 1$, which indicates that the controller can further utilize the available friction. However, since no-slip gain k_{noSlip} was not used in this case, the controller does not increase the estimated friction value.

The behavior of the controller with an over-estimated friction value on a paved surface is very similar to the behavior on a salt surface. Figure 5.19 demonstrates how the feedback steering controller provides countersteer input (Fig. 5.19a) and modulates the longitudinal feedback input (Fig. 5.19b) to maintain the vehicle's yaw stability and path tacking ability at the friction limits.

Figure 5.20 shows the acceleration of the vehicle corresponding to the controller inputs and the vehicle states in Fig. 5.18. At the beginning of the clothoid entry, the

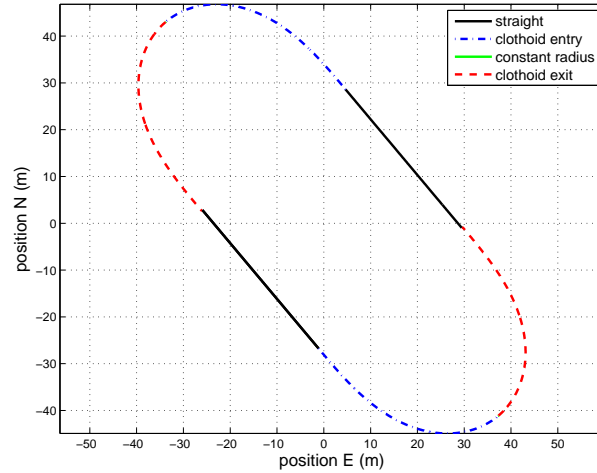


Figure 5.16: Map used on a paved surface with gravel on top, plotting on North and East coordinates. Note that the map has very short constant radius sections

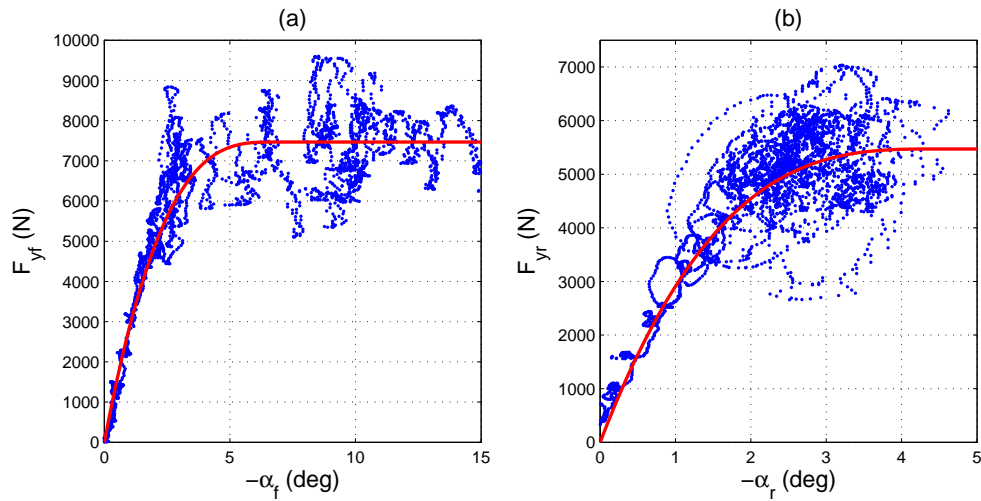


Figure 5.17: Front (a) and rear (b) tire curves fitted to the ramp steer data, on a paved surface with gravel on top

Table 5.3: Controller gains and parameters for paved surface

estimated friction value	μ	0.7	
front cornering stiffness	C_f	190,000	N/rad
rear cornering stiffness	C_r	210,000	N/rad
including weight transfer		yes	
<i>steering controller</i>			
lanekeeping gain	k_p	3,500	N/m
lookahead distance	x_{la}	20	m
yaw damping	$k_{\Delta\psi}$.1	s
<i>longitudinal controller</i>			
front axle lateral slip	α_f^{ref}	5	deg
limited front axle lateral slip	α_f^{lim}	8	deg
rear axle lateral slip	α_r^{ref}	5	deg
front axle longitudinal slip	κ_{front}^{ref}	.1	
rear axle longitudinal slip	κ_{rear}^{ref}	.1	
kappa front slip gain	k_κ^f	3,000	N
alpha front slip gain	k_α^f	2,000	N
kappa rear slip gain	k_κ^r	3,000	N
alpha rear slip gain	k_α^r	2,000	N
no-slip gain	k_{noSlip}	0	N
speed gain	k_{speed}	2,000	Ns/m

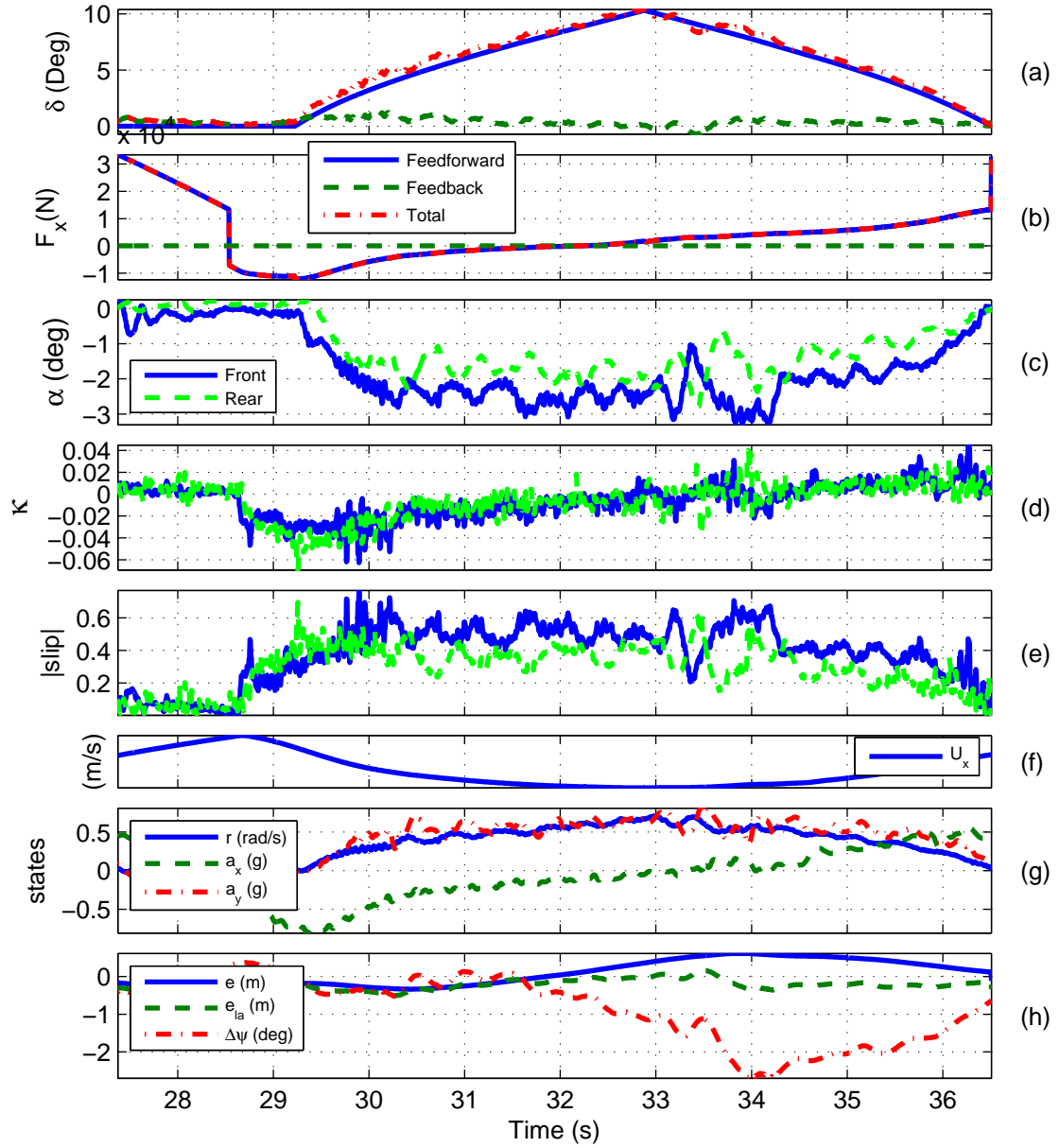


Figure 5.18: Controller commands (a-b) and vehicle states (c-h) on paved surface, with zero no-slip gain. Feedback force in Figure b only shows slip circle controller command.

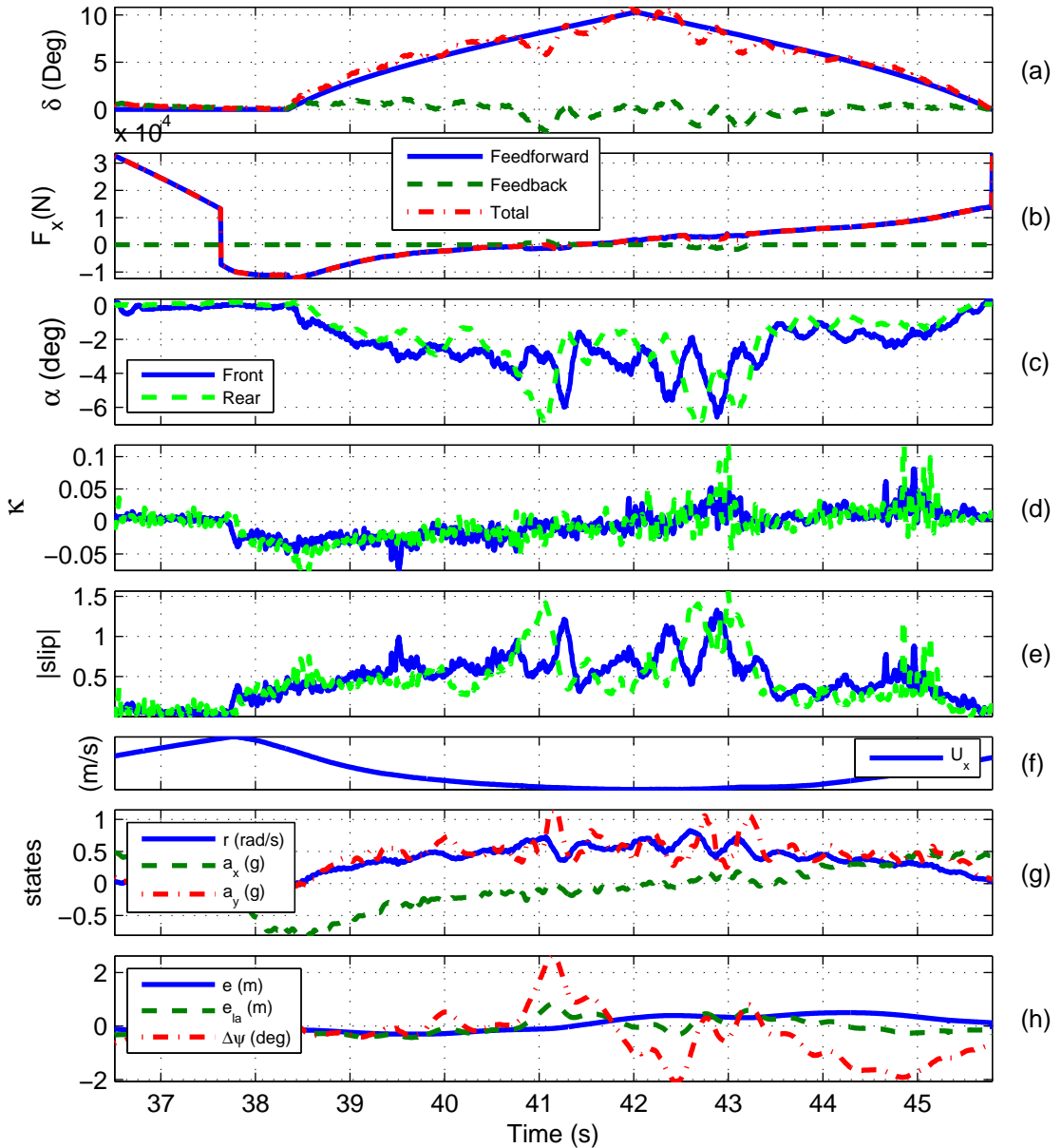


Figure 5.19: Controller commands (a-b) and vehicle states (c-h) on paved surface when the friction value is over-estimated, with zero no-slip gain. Feedback force in Figure b only shows slip circle controller command.

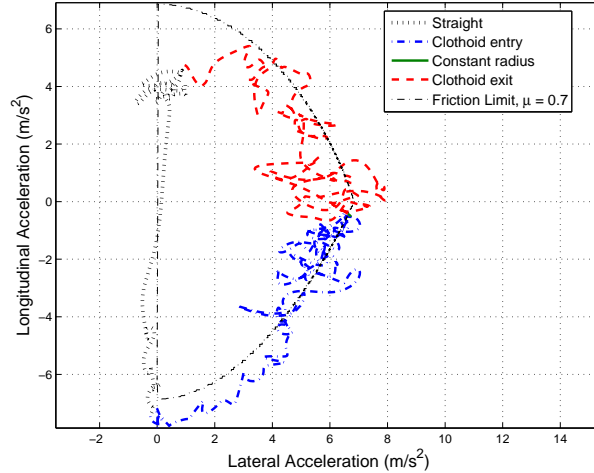


Figure 5.20: “*g-g*” diagram from Audi TTS on paved surface, with zero no-slip gain

vehicle acceleration is outside of the friction limit circle in the “*g-g*” diagram. This indicates that the vehicle speed does not track the desired speed because the speed feedback force $F_x^{speedFeedback}$ in (4.7) commands additional braking. This additional braking creates the deceleration that is beyond the predicted friction limit (Fig. 5.20). The issue of speed tracking is clearly demonstrated in Fig. 5.21 where as much as 1 m/s error in speed tracking is observed.

Although 1m/s may sound insignificant, Figure 5.22 depicts the significance of 1 m/s difference in the corner entry speed U_x^0 . A point mass model and (2.4) are used to create the simulation results in Fig. 5.22. The point mass goes through the same curve at different initial speed, and the plots stop when $\mu g < \sqrt{a_x^2 + a_y^2}$ in (2.4). With the correct corner entry speed of $U_x^0 = 17$ m/s, the point mass travels 20 m along the clothoid entry before it enters the constant radius section. However, with the corner entry speed of $U_x^0 = 18$ m/s, the point mass can only travel 13.7 m along the clothoid entry segment before it runs out of friction force to make the point mass follow the path. After 13.7 m, the point mass will slide and deviate from the intended path. In addition, notice that the difference between the speed profiles grows beyond 1 m/s as the point mass progresses along the path.

Furthermore, in Fig. 5.21, the vehicle accelerates at full-throttle in the straight

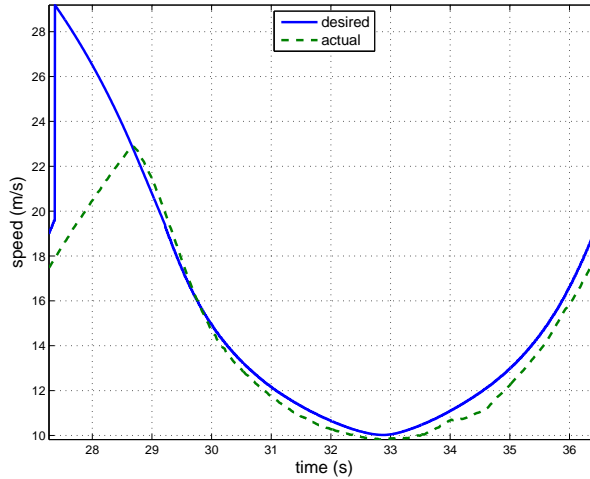


Figure 5.21: Poor speed tracking on paved surface, with zero no-slip gain

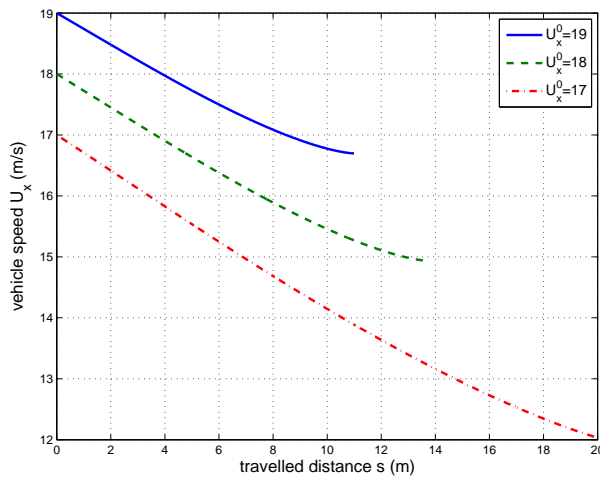


Figure 5.22: Effects of the corner entry speed, using a point mass model

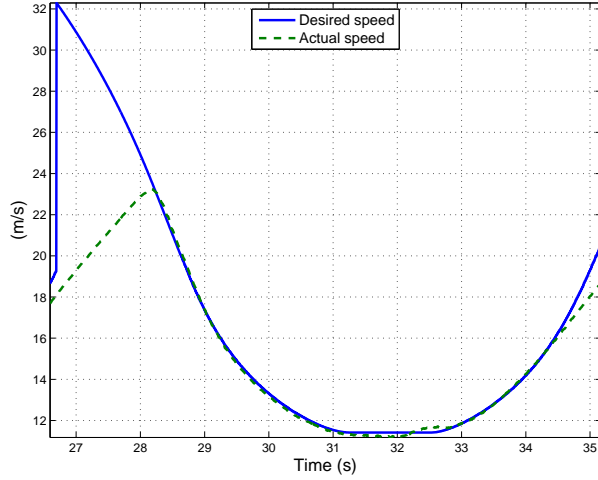


Figure 5.23: Improved speed tracking on paved surface, with zero no-slip gain

section until it hits the braking point, calculated from (2.10), at $t=28.7$ s. Nevertheless, the actual vehicle's speed overshoots the desired speed after the vehicle starts braking. This was due to the time delay in the brake system which was later compensated in Section 5.4.1. Besides compensating for the time delay in the brake system, the speed gain k_{speed} in (4.7) was tuned in the following section to improve the speed tracking.

5.4.1 Tracking the desired speed

Increasing the speed gain k_{speed} from 2,000 to 6,000 Ns/m improves the speed tracking performance as shown in Fig. 5.23. The speed tracking error after $t=34.5$ s is due to the limited engine power because the controller already applies 100% throttle input. Tighter speed tracking is possible by further increasing the speed gain k_{speed} ; however, if k_{speed} is too high, the longitudinal force could induce undesirable pitch oscillation.

The differences between the desired speed and the actual speed during $t=26.7$ - 28.2 s may appear to be large due to a jump in the desired speed when the segment changes from a clothoid exit to a straight section. However, this is not a concern as the desired speed in the straight section is calculated backward from the corner entry

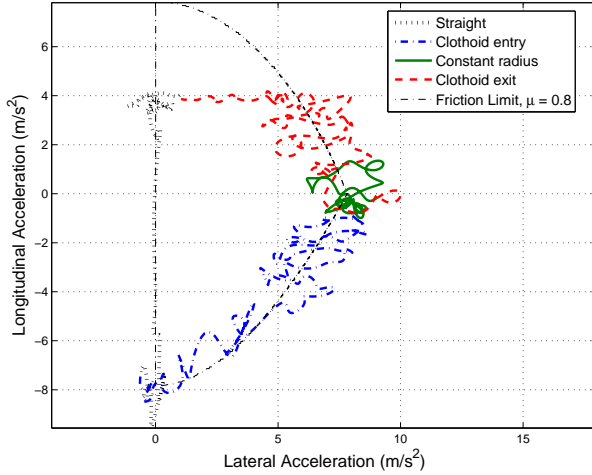


Figure 5.24: “*g-g*” diagram from Audi TTS on paved surface, after tuning speed gain

speed using the algorithm discussed in Section 2.4, while the desired speed during corner exit is dictated by the friction limit circle. Consequently, the desired speed calculation switches when the vehicle travels from a clothoid exit into a straight section. During the early part of the straight, the controller merely applies full-throttle until it hits the braking point, which is the desired behavior.

With better speed tracking, the vehicle’s acceleration tracks the friction limit closely, especially the early part of the corner entry, as shown in the “*g-g*” diagram of Fig 5.24.

5.5 Pikes Peak

In September 2010, the Audi TTS drove autonomously up Pikes Peak International Hill Climb course in Colorado (see Fig. 5.25) six times. The controller discussed in Chapter 2 to 5 was used to test the robustness of the controller because the course consists of both paved and rough dirt surfaces, not to mention the 12.4 miles that climbs up 4,721 ft with an average grade of 7% [30]. The mission of this trip was not to set the course record because the Audi had to follow a lead-vehicle. The Audi did not have a vision system at that time; thus, it required a lead-vehicle to check for

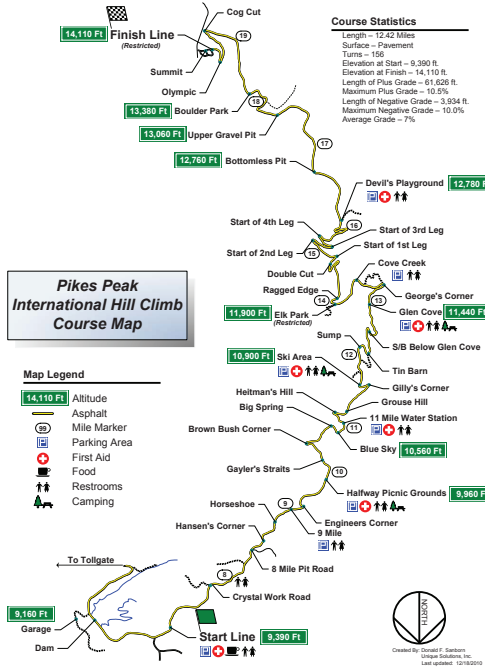


Figure 5.25: Pikes Peak International Hill Climb Course Map [30]

any obstacles such as hikers or animals on the path. The testing experience provided valuable insights regarding the importance of tracking the desired speed when using a complex map, as mentioned in Section 5.3.3, as well as the effects of bank and grade.

5.6 Conclusions

A preliminary controller discussed in Chapter 2-4 was tested on dirt, salt and paved surfaces. The experimental results show that the controller can operate at the friction limit while maintaining minimal tracking error. The controller behavior when the vehicle understeers and oversteers are also discussed, showing that the system remains stable even when the friction value is over-predicted. Adding yaw damping

into the controller minimizes the oscillation in the vehicle states, as discussed in Section 5.3.4, while tuning the speed tracking ensures that the vehicle enters a corner at the correct speed (Section 5.4.1). Furthermore, the results also demonstrate the potential problem associated with using the no-slip gain k_{noSlip} . Using the no-slip gain k_{noSlip} without monitoring vehicle speed can cause excessive corner entry speed for the subsequent corner when a complex map is used. Thus, the no-slip gain k_{noSlip} is no longer used for the rest of the dissertation, and the speed controller that tracks the desired speed profile is used instead.

Chapter 6

Integrated Steering Controller

The basic steering controller is discussed in Chapter 3 and the results in Chapter 5 show that the controller can track the desired path at the limits of the handling. The system appears stable even when the tires are in the nonlinear region, and the experimental results show that the steering controller provides yaw stability through countersteering input when the vehicle oversteers. For eventual integration into safety systems; however, a stronger understanding of stability properties is necessary.

Therefore, a new steering controller structure with a more consistent controller objective is proposed in this chapter. Previously, the goal of the feedforward steering in Section 3.1 was to control the lateral error e referenced to the vehicle center of gravity (CG), while the feedback steering controller in Section 3.2 regulated the lookahead error e_{la} , which is a point projected in front of a vehicle. Thus, the feedforward and feedback steering controllers in Chapter 3 utilized different reference points for controlling the lateral motion of the vehicle. Consequently, a more integrated steering is presented in this chapter, where both feedforward and feedback steering submodules use the same reference point at the center of percussion (COP). Furthermore, to improve the model fidelity of the feedforward steering used in Section 3.1, tire nonlinearity and transient dynamics were taken into account. A fixed-gain full-state steering feedback structure was used to analyze the system's stability, and the sets of gains derived from both the steering controller in Chapter 3 and from state-space techniques were analyzed.

The rest of this chapter is structured as follows. Section 6.1 describes the use of a bicycle model to derive the equations of motion in order to compute the feedforward steering command from the COP. To provide stability to the system, a fixed-gain full-state steering feedback was used in Section 6.1.3 with the set of gains derived from the lanekeeping system with yaw damping in Chapter 3. Using a state-space form, Section 6.1.5 shows a method of finding a Lyapunov function to prove that the system is asymptotically stable. A simulation is created to understand the controller’s behavior and investigate the controller’s sensitivity to the estimated friction value in Section 6.2. Section 6.3 describes the experimental results of this new steering controller structure, which correlate well with simulation results. Other methods of designing feedback gains, such as output feedback linearization, analytic Lyapunov function and Linear Quadratic Regulator (LQR), are discussed in Section 6.4. The stability and the experimental results of each method are also discussed in Section 6.4. Interestingly, none of these other methods for gain selection outperforms the gains derived from lanekeeping and yaw damping in Section 6.1.3.

6.1 Using the center of percussion to design an integrated steering controller

To calculate a steering command, a force-based approach is utilized for computing feedforward and feedback steering inputs. From a bicycle model, vehicle dynamics state variables are transformed into tracking state variables, where utilizing the center of percussion (COP) as a reference point eliminates all the terms associated with the rear tire force. This creates a feedforward steering command that is robust to the disturbances from the rear tire force and simplifies the controller structure. The COP is then employed for designing a feedback steering controller in a state-space amenable to stability analysis using Lyapunov theory.

From the bicycle model in Fig. 3.2, the longitudinal force at the front wheel only has minimal effect on the lateral and yaw motion. Consequently, from assuming a small steering angle and ignoring longitudinal forces, the lateral and yaw equations

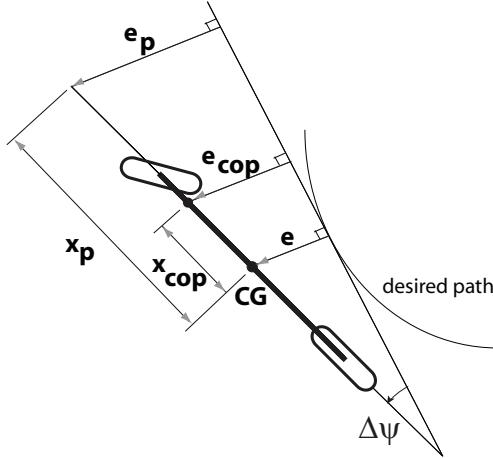


Figure 6.1: Lateral tracking parameters

of motion can be written as

$$\begin{aligned} F_{yf} + F_{yr} &= ma_y = m(\dot{U}_y + U_x r) \\ aF_{yf} - bF_{yr} &= I_{zz}\dot{r}, \end{aligned} \quad (6.1)$$

where a_y and U_y are the lateral acceleration and speed respectively (Fig. 3.2), and I_{zz} is the vehicle's yaw moment of inertia.

To focus on path tracking ability, the vehicle dynamics state variables U_y and r are transformed into state variables referenced to the desired path. Figure. 6.1 defines the lateral error e (referenced to the center of gravity), heading error $\Delta\psi$, and projected error e_p . The relationships between each variable are

$$\begin{aligned} \Delta\psi &= \psi - \psi_r \\ e_p &= e + x_p \sin \Delta\psi \\ \dot{e} &= U_y \cos(\Delta\psi) + U_x \sin(\Delta\psi) \\ \dot{s} &= U_x \cos(\Delta\psi) - U_y \sin(\Delta\psi), \end{aligned} \quad (6.2)$$

where s is the traveled distance, ψ is the vehicle heading, ψ_r is the heading of the

road (path) and x_p is the constant projected distance in Fig. 6.1. By using a small angle approximation for $\Delta\psi$ and assuming that $\dot{U}_x\Delta\psi \approx 0$, differentiating $\Delta\psi$ and e_p in (6.2) results in

$$\begin{aligned}\dot{\Delta\psi} &= r - \mathcal{K}\dot{s} \\ \dot{e}_p &= \dot{e} + x_p\Delta\dot{\psi} \\ \ddot{\Delta\psi} &= \dot{r} - \mathcal{K}\ddot{s} - \dot{\mathcal{K}}\dot{s} \\ \ddot{e}_p &= \dot{U}_y + U_xr - U_x\mathcal{K}\dot{s} + x_p\dot{r} - x_p(\mathcal{K}\ddot{s} + \dot{\mathcal{K}}\dot{s}) ,\end{aligned}\tag{6.3}$$

Substituting $a_y = \dot{U}_y + U_xr$ and \dot{r} from (6.1) into (6.3) yields

$$\begin{aligned}\ddot{\Delta\psi} &= \frac{aF_{yf}-bF_{yr}}{I_{zz}} - \mathcal{K}\ddot{s} - \dot{\mathcal{K}}\dot{s} \\ \ddot{e}_p &= \frac{F_{yf}+F_{yr}}{m} - U_x\mathcal{K}\dot{s} + x_p\frac{aF_{yf}-bF_{yr}}{I_{zz}} - x_p(\mathcal{K}\ddot{s} + \dot{\mathcal{K}}\dot{s}).\end{aligned}\tag{6.4}$$

In (6.4), the steering actuator can only command the front tire force F_{yf} , but has no control over F_{yr} . The rear tire force F_{yr} is generated from the rear slip angle α_r , which changes dynamically according to the vehicle dynamics. Thus, with one input (F_{yf}), the controller can only control one output such as lateral motion e , yaw motion $\Delta\psi$, or a combination of both e and $\Delta\psi$ (i.e. e_p in (6.2)).

6.1.1 Center of percussion

From (6.4), we can choose any projected distance x_p to calculate \ddot{e}_p , as long as the rear tire force F_{yr} is known (F_{yf} is known because it is the input that we specified). However, there is one projected distance x_{cop} in Fig. 6.1 that, if chosen, allows the influence of the rear tire force F_{yr} to be ignored. This eliminates the need to estimate F_{yr} , which is constantly changing through vehicle dynamics as well as highly nonlinear at the limits of handling. This projecting point is called the center of percussion (COP).

At the COP

$$x_{cop} = \frac{I_{zz}}{bm}, \quad (6.5)$$

the effects of the rear tire force on \ddot{e}_p in (6.4) cancel each other out, i.e.

$$\frac{F_{yr}}{m} + x_{cop} \frac{-bF_{yr}}{I_{zz}} = 0. \quad (6.6)$$

This equation is the same as the definition of the center of percussion given by Milliken et al. [50].

Figure 6.2 explains the benefit of using the COP as a reference point for the steering controller. In Fig. 6.2, the rear tire forces F_{yr} produces two effects on the system dynamics. First, they create a constant lateral acceleration of \hat{a}_{yr} along the body of the vehicle. Second, it creates an angular acceleration of \hat{r}_r around the vehicle's CG. At the COP, the effect of rear tire force on the lateral acceleration $\hat{a}_{yr} = \frac{F_{yr}}{m}$ cancels the effect on the rotational acceleration $x_{cop}\hat{r}_r = x_{cop}\frac{bF_{yr}}{I_{zz}}$. As a consequence, using this approach does not require the knowledge of F_{yr} and requires only path information for the calculation.

The benefit of using the COP is demonstrated by substituting x_{cop} in (6.5) into \ddot{e}_p in (6.4)

$$\begin{aligned} \ddot{e}_{cop} &= \frac{F_{yf} + F_{yr}}{m} - U_x \mathcal{K} \dot{s} + x_{cop} \frac{aF_{yf} - bF_{yr}}{I_{zz}} - x_{cop}(\mathcal{K} \ddot{s} + \dot{\mathcal{K}} \dot{s}) \\ &= \frac{L}{b} \frac{F_{yf}}{m} - U_x \mathcal{K} \dot{s} - x_{cop}(\mathcal{K} \ddot{s} + \dot{\mathcal{K}} \dot{s}), \end{aligned} \quad (6.7)$$

where e_{cop} is the lateral error referenced to the center of percussion and L is the vehicle length ($a + b$). The rear tire force F_{yr} is now eliminated from the equation. Consequently, e_{cop} only depends on the front tire force, which can be directly controlled by the steering input. Using the COP also simplifies the feedforward steering calculation as demonstrated in the following section.

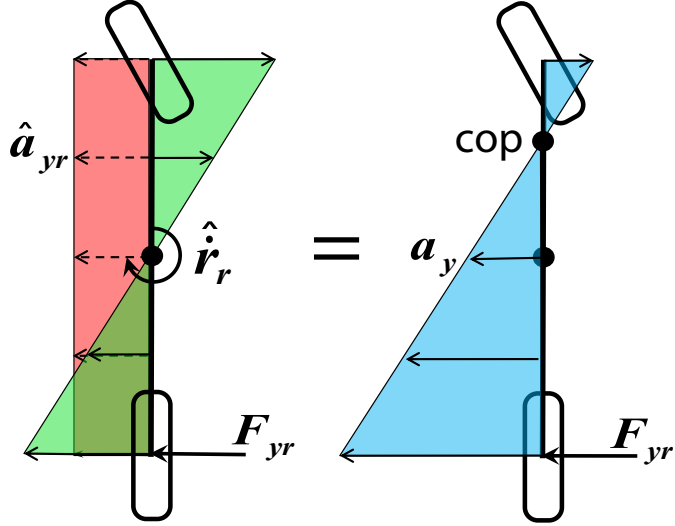


Figure 6.2: Effect of rear tire force at the center of percussion, superimposing rotational and translational effects

6.1.2 Feedforward steering controller

The objective of the feedforward steering force F_{yf}^{FFW} is to eliminate the dynamics of the lateral acceleration \ddot{e}_{cop} . Thus, by equating \ddot{e}_{cop} to zero in (6.7), F_{yf}^{FFW} can be found from

$$F_{yf}^{FFW} = \frac{mb}{L}(U_x \mathcal{K}\dot{s} + x_{cop}(\mathcal{K}\ddot{s} + \dot{\mathcal{K}}\dot{s})) . \quad (6.8)$$

This feedforward steering force eliminates the effect of road curvature by canceling all the terms associated with the curvature \mathcal{K} in the lateral dynamics equation (6.7). In order to calculate F_{yf}^{FFW} in (6.8), the value of x_{cop} , and consequently the value of I_{zz} in (6.5), is required.

Separating the front tire force input into feedforward F_{yf}^{FFW} and feedback F_{yf}^{FB} parts ($F_{yf} = F_{yf}^{FFW} + F_{yf}^{FB}$) and substituting F_{yf}^{FFW} from (6.8) into (6.4) and (6.7) results in

$$\begin{aligned}\Delta\ddot{\psi} &= \frac{a}{I_{zz}}F_{yf}^{FB} + \frac{U_x}{L}\mathcal{K}\dot{s} - \frac{b}{I_{zz}}F_{yr} - \frac{b}{L}(\mathcal{K}\ddot{s} + \dot{\mathcal{K}}\dot{s}) \\ \ddot{e}_{cop} &= \frac{\frac{L}{b}F_{yf}^{FB}}{m}.\end{aligned}\quad (6.9)$$

Consequently, from (6.9), the equations of motion can be written in state-space form as

$$\frac{d}{dt} \begin{bmatrix} e_{cop} \\ \dot{e}_{cop} \\ \Delta\psi \\ \Delta\dot{\psi} \end{bmatrix} = \begin{bmatrix} 0 & 1 & 0 & 0 \\ 0 & 0 & 0 & 0 \\ 0 & 0 & 0 & 1 \\ 0 & 0 & 0 & 0 \end{bmatrix} \begin{bmatrix} e_{cop} \\ \dot{e}_{cop} \\ \Delta\psi \\ \Delta\dot{\psi} \end{bmatrix} + \begin{bmatrix} 0 \\ \frac{L}{bm} \\ 0 \\ \frac{a}{I_{zz}} \end{bmatrix} F_{yf}^{FB} + \begin{bmatrix} 0 \\ 0 \\ 0 \\ -\frac{b}{I_{zz}} \end{bmatrix} F_{yr} + \begin{bmatrix} 0 \\ 0 \\ 0 \\ \frac{U_x\mathcal{K}\dot{s}}{L} - \frac{b}{L}(\mathcal{K}\ddot{s} + \dot{\mathcal{K}}\dot{s}) \end{bmatrix} \quad (6.10)$$

The last vector shows the disturbance from road curvature that the controller cannot eliminate, unless it has an independent actuator to control rear tire force. The representation in (6.10) motivates the use of a state-feedback controller.

6.1.3 Feedback steering controller

The objectives of the feedback steering controller are to provide path tracking and yaw stability to the system, even when the rear tires are saturated (a limit oversteer condition). The scenario when the front tires are fully saturated (a limit understeer condition) is not considered in this chapter as the vehicle yaw dynamics remain stable, albeit with growing tracking error. A limit understeer condition occurs when the steering controller tries to track an infeasible path or has insufficient control authority. Consequently, to minimize understeering, the controller has to adjust the desired path or ensure the correct corner entry speed according to the available friction.

In (6.10), rear lateral tire force F_{yr} is not an input into the system and depends on the vehicle states. Thus, the effect from the rear tire force is incorporated into the system matrix.

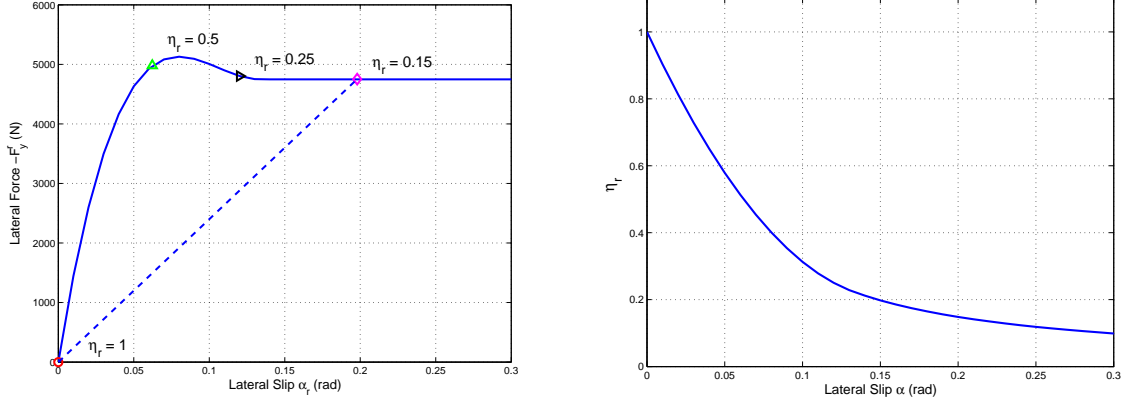


Figure 6.3: Rear tire curve, showing the effect of η_r

Figure 6.4: Monotonically decreasing η_r function

Incorporating rear tire force

Rear tire force is generated through vehicle dynamics and is a function of rear slip angle α_r . When using a linear tire assumption, tire force is linearly proportional to its slip angle ($F_{yr} = -C_r\alpha_r$, where C_r is the rear cornering stiffness). However, when operating a vehicle at its limits, a linear tire assumption is no longer valid. In this paper, a dimensionless parameter η proposed by Talvala et al. [76, 77] is introduced to capture this nonlinear behavior of the rear tires. Unlike using a local cornering stiffness where the local slope goes to zero when a tire is highly saturated, the parameter η still captures the fact that the tire still generates lateral force even when it is highly saturated. The value η can vary from one (when the tire is perfectly linear) towards zero (when the slip angle α goes to infinity), allowing the rear tire force to be described as

$$F_{yr} = -\eta_r C_r \alpha_r. \quad (6.11)$$

Figure 6.3 shows how η_r captures the nonlinearity of the Fiala brush tire model [60]. In Fig. 6.4, the parameter η_r is a function of α_r and remains positive and monotonically decreases as the slip angle increases.

In order to analyze the stability of the system matrix, the rear slip angle α_r in

(6.11) has to be converted into tracking states. From Fig. 3.2, the rear slip angle α_r is calculated from

$$\alpha_r = \arctan\left(\frac{U_y - br}{U_x}\right). \quad (6.12)$$

By using a coordinate transformation in (6.2) and a small angle approximation, the rear slip angle α_r can be rewritten using the tracking states at the COP as

$$\alpha_r = \frac{\dot{e}_{cop} - x_{cop}\Delta\dot{\psi} - U_x\Delta\psi - b(\Delta\dot{\psi} + \dot{\psi}_r)}{U_x}. \quad (6.13)$$

Substituting α_r from (6.13) into (6.11) results in

$$F_{yr} = -\eta C_r \frac{\dot{e}_{cop} - \dot{L}\Delta\dot{\psi} - U_x\Delta\psi - b\mathcal{K}\dot{s}}{U_x}, \quad (6.14)$$

where $\dot{L} = b + x_{cop}$, which is approximately equal to L . This is because from NHTSA's data on vehicle inertial parameters [23], I_{zz} can be approximated by mab ($I_{zz} \approx mab$), which means $x_{cop} \approx a$. By replacing F_{yr} in (6.10) with F_{yr} from (6.14), the new equations of motion in state-space form can be found.

$$\begin{aligned} \frac{d}{dt} \begin{bmatrix} e_{cop} \\ \dot{e}_{cop} \\ \Delta\psi \\ \Delta\dot{\psi} \end{bmatrix} &= \begin{bmatrix} 0 & 1 & 0 & 0 \\ 0 & 0 & 0 & 0 \\ 0 & 0 & 0 & 1 \\ 0 & \frac{b\eta_r C_r}{I_{zz} U_x} & -\frac{b\eta_r C_r}{I_{zz}} & -\frac{\dot{L}b\eta_r C_r}{I_{zz} U_x} \end{bmatrix} \begin{bmatrix} e_{cop} \\ \dot{e}_{cop} \\ \Delta\psi \\ \Delta\dot{\psi} \end{bmatrix} + \begin{bmatrix} 0 \\ \frac{L}{bm} \\ 0 \\ \frac{a}{I_{zz}} \end{bmatrix} F_{yf}^{FB} \\ &\quad + \begin{bmatrix} 0 \\ 0 \\ 0 \\ \frac{U_x \mathcal{K}\dot{s}}{L} - \frac{b}{L}(\mathcal{K}\ddot{s} + \dot{\mathcal{K}}\dot{s}) - \frac{b^2 \eta_r C_r \mathcal{K}\dot{s}}{I_{zz} U_x} \end{bmatrix} \end{aligned} \quad (6.15)$$

The dynamics of the lateral tracking equation e_{cop} in (6.15) are decoupled from the heading error $\Delta\psi$, when using the COP as a reference point. Since \ddot{e}_{cop} does not depend on $\Delta\psi$ or $\Delta\dot{\psi}$, the motion of the COP, e_{cop} , only depends on the front feedback tire force F_{yf}^{FB} . On the contrary, the yaw motion $\Delta\ddot{\psi}$ still contains \dot{e}_{cop} , $\Delta\psi$ and $\Delta\dot{\psi}$

as the vehicle's yaw motion depends on the balance between front and rear tire force. Furthermore, the controllability matrix of the system in (6.15) is full rank when η_r is close to one (i.e. when rear tires behave linearly). However, when the rear tires are highly saturated (η_r approaches zero), the system approaches uncontrollability as it behaves like two separate double integrator systems with a single input ($\ddot{e}_{cop} = \frac{L}{bm} F_{yf}^{FB}$ and $\Delta\ddot{\psi} = \frac{a}{I_{zz}} F_{yf}^{FB}$ in the limit case where $\eta_r = 0$).

From the state-space equation (6.15), a suitable feedback control law for F_{yf}^{FB} is designed and analyzed in the following section.

Fixed gains linear feedback

A full-state linear feedback controller is used for designing a steering controller. This method shapes the dynamic response of the linear system by strategically placing the closed-loop poles at specific locations. Although this approach is normally used for linear time invariant systems, the following sections demonstrate how a set of linear fixed gains adapted from a lanekeeping system can be used to provide Lyapunov stability for the nonlinear system.

With a full-state feedback controller, the feedback control law for the front steering system is

$$F_{yf}^{FB} = -\mathbf{K}x = -k_1 e_{cop} - k_2 \dot{e}_{cop} - k_3 \Delta\psi - k_4 \dot{\Delta\psi}, \quad (6.16)$$

where $x = [e_{cop} \ \dot{e}_{cop} \ \Delta\psi \ \dot{\Delta\psi}]^T$ and $\mathbf{K} = [k_1 \ k_2 \ k_3 \ k_4]$.

After adding fixed-gains full-state feedback (6.16) into (6.15), the closed loop system equation becomes

$$\frac{d}{dt} \begin{bmatrix} e_{cop} \\ \dot{e}_{cop} \\ \Delta\psi \\ \dot{\Delta\psi} \end{bmatrix} = \begin{bmatrix} 0 & 1 & 0 & 0 \\ -\frac{k_1 L}{bm} & -\frac{k_2 L}{bm} & -\frac{k_3 L}{bm} & -\frac{k_4 L}{bm} \\ 0 & 0 & 0 & 1 \\ -\frac{k_1 a}{I_{zz}} & -\frac{k_2 a}{I_{zz}} + \frac{b\eta_r C_r}{I_{zz} U_x} & -\frac{k_3 a}{I_{zz}} - \frac{b\eta_r C_r}{I_{zz}} & -\frac{k_4 a}{I_{zz}} - \frac{\dot{L}b\eta_r C_r}{I_{zz} U_x} \end{bmatrix} \begin{bmatrix} e_{cop} \\ \dot{e}_{cop} \\ \Delta\psi \\ \dot{\Delta\psi} \end{bmatrix} + \begin{bmatrix} 0 \\ 0 \\ 0 \\ \frac{U_x \mathcal{K}\dot{s}}{L} - \frac{b}{L}(\mathcal{K}\ddot{s} + \dot{\mathcal{K}}\dot{s}) - \frac{b^2 \eta_r C_r \mathcal{K}\dot{s}}{I_{zz} U_x} \end{bmatrix}. \quad (6.17)$$

The goal of the feedback steering controller is to provide path tracking ability with yaw stability. A set of gains for a state feedback controller adapted from the steering feedback controller in Chapter 3 is used as a starting point to analyze the stability of the system. The following sections provide the stability proof at the limits and explain how the controller works.

Adapting from lanekeeping

A set of gains in (6.16) is derived from the feedback steering controller (3.13) in Chapter 3. Using (6.2) to transform e into e_{cop} and a small angle assumption, the front lateral feedback force F_{yf}^{FB} is calculated from

$$\begin{aligned} F_{yf}^{FB} &= -k_{LK}(e + x_{la} \sin \Delta\psi) - k_{\Delta\dot{\psi}} \Delta\dot{\psi} \\ &= -k_{LK}(e_{cop} + (x_{la} - a)\Delta\psi) - k_{\Delta\dot{\psi}} \Delta\dot{\psi}, \end{aligned} \quad (6.18)$$

where the values of lanekeeping gain k_{LK} , the lookahead distance x_{la} and the yaw damping gain $k_{\Delta\dot{\psi}}$ are summarized in Table 6.1. Comparing to (6.16), this is equivalent to having $k_1 = k_{LK}$, $k_2 = 0$, $k_3 = k_{LK}(x_{la} - a)$ and $k_4 = k_{\Delta\dot{\psi}}$. Thus, while k_1 adds path tracking ability to the controller, k_3 and k_4 provides yaw stability for the system.

Table 6.1: Controller gains and parameters based on the controller in Chapter 3

<i>Steering controller</i>	<i>Symbol</i>	<i>Value</i>	<i>Unit</i>
lanekeeping	k_{LK}	4000	N/m
lookahead distance	x_{la}	20	m
yaw damping	$k_{\Delta\dot{\psi}}$	9,500	N·s/rad
<i>Equivalent gains in full-state feedback form</i>			
e_{cop}	k_1	4000	N/m
\dot{e}_{cop}	k_2	0	N·s/m
$\Delta\dot{\psi}$	k_3	75,824	N
$\Delta\psi$	k_4	9,500	N·s/rad

6.1.4 Converting front lateral force to steering input

Once the feedforward and feedback front lateral force are calculated, the total force F_{yf} can be converted into the desired front steering angle input δ by using a front slip angle equation with a small angle approximation, i.e.

$$\delta = \frac{U_y + ar}{U_x} - \alpha_f^{des}, \quad (6.19)$$

where the desired front slip angle α_f^{des} is found from a nonlinear tire curve and the required front lateral force F_{yf} (see Fig. 6.5).

Some modifications have been made to the nonlinear tire curve used in (6.19), as depicted in Fig. 6.5. The kinetic friction coefficient μ_k is increased to be the same value as the static coefficient μ_s . The tire force is now monotonically decreasing as the slip angle increases; thus, creating a one-to-one relationship which does not exist if $\mu_s \neq \mu_k$. As a consequence, the lookup table function avoids the issue of having two lateral slip values corresponding to one tire force value. Furthermore, the tire curve in Fig. 6.5 limits the maximum front lateral slip, which is similar to the front maximum lateral slip α^{lim} in Section 3.2.1.

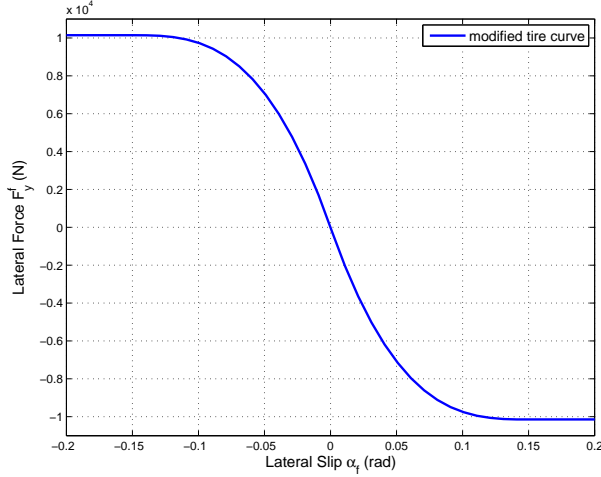


Figure 6.5: Modified tire curve used in (6.19)

6.1.5 Stability at the limits

The stability of the system can be analyzed from (6.17) with the gains described in Table 6.1. The disturbance vector in (6.17) is caused by the path's curvature and is bounded. From the definition of traveled distance along the path s , $|\dot{s}|$ is bounded by the longitudinal speed $|U_x|$ and $|\ddot{s}|$ is bounded by the vehicle's longitudinal acceleration $|a_x|$. The system's stability is analyzed with the absence of the disturbance from the curvature.

Lyapunov theory is used to check the stability of the system [70]. If a matrix P exists such that $\mathcal{L} = x^T Px$ is positive and $\dot{\mathcal{L}} = x^T(A^T P + PA)x$ is negative for all nonzero x , then the system $\dot{x} = Ax$ is asymptotically stable. These requirements can be written as $P \succ 0$ and $A^T P + PA \prec 0$, where A is the closed-loop system matrix in (6.17).

In order to find P such that the system in (6.17) is guaranteed to be asymptotically stable for a wide operating range of the rear tires (η_r), matrix A is rewritten as a convex combination of A_1 and A_2

$$A = A_1 + \eta_r A_2 , \quad (6.20)$$

where

$$A_1 = \begin{bmatrix} 0 & 1 & 0 & 0 \\ -\frac{k_1 L}{bm} & -\frac{k_2 L}{bm} & -\frac{k_3 L}{bm} & -\frac{k_4 L}{bm} \\ 0 & 0 & 0 & 1 \\ -\frac{k_1 a}{I_{zz}} & -\frac{k_2 a}{I_{zz}} & -\frac{k_3 a}{I_{zz}} & -\frac{k_4 a}{I_{zz}} \end{bmatrix} \quad \text{and} \quad A_2 = \begin{bmatrix} 0 & 0 & 0 & 0 \\ 0 & 0 & 0 & 0 \\ 0 & 0 & 0 & 0 \\ 0 & \frac{bC_r}{I_{zz}U_x} & -\frac{bC_r}{I_{zz}} & -\frac{\dot{L}bC_r}{I_{zz}U_x} \end{bmatrix}.$$

Consequently, $A^T P + PA$ can be rewritten as

$$\begin{aligned} A^T P + PA &= (A_1 + \eta_r A_2)^T P + P(A_1 + \eta_r A_2) \\ &= A_1^T P + PA_1 + \eta_r (A_2^T P + PA_2). \end{aligned} \tag{6.21}$$

This convex combination of A_i implies that if $P \succ 0$ is found such that (6.22) is satisfied for different η_r values (η_r^{min} and η_r^{max}), then the resulting system from $\eta_r^{min} \leq \eta_r \leq \eta_r^{max}$ is asymptotically stable.

$$\begin{aligned} A_1^T P + PA_1 + \eta_r^{min} (A_2^T P + PA_2) &\prec 0 \\ A_1^T P + PA_1 + \eta_r^{max} (A_2^T P + PA_2) &\prec 0 \end{aligned} \tag{6.22}$$

Similar to (6.21), the system matrix can be rearranged to pull out the speed inverse $1/U_x$.

$$A = A_3 + \frac{1}{U_x} A_4, \tag{6.23}$$

where

$$A_3 = \begin{bmatrix} 0 & 1 & 0 & 0 \\ -\frac{k_1 L}{bm} & -\frac{k_2 L}{bm} & -\frac{k_3 L}{bm} & -\frac{k_4 L}{bm} \\ 0 & 0 & 0 & 1 \\ -\frac{k_1 a}{I_{zz}} & -\frac{k_2 a}{I_{zz}} & -\frac{k_3 a}{I_{zz}} - \frac{b\eta_r C_r}{I_{zz}} & -\frac{k_4 a}{I_{zz}} \end{bmatrix} \quad \text{and} \quad A_4 = \begin{bmatrix} 0 & 0 & 0 & 0 \\ 0 & 0 & 0 & 0 \\ 0 & 0 & 0 & 0 \\ 0 & \frac{b\eta_r C_r}{I_{zz}} & 0 & -\frac{L b\eta_r C_r}{I_{zz}} \end{bmatrix}.$$

If $P \succ 0$ is found for different speed inverse values ($1/U_x^{min}$ and $1/U_x^{max}$) such that equations in (6.24) are satisfied, then any values of $1/U_x$ between $1/U_x^{min}$ and $1/U_x^{max}$ are asymptotically stable.

$$\begin{aligned} A_3^T P + P A_3 + \frac{1}{U_x^{min}} (A_4^T P + P A_4) &\prec 0 \\ A_3^T P + P A_3 + \frac{1}{U_x^{max}} (A_4^T P + P A_4) &\prec 0. \end{aligned} \quad (6.24)$$

A matrix P that satisfies both (6.22) and (6.24) can be found by using Matlab's Linear Matrix Inequality solver [34]. These matrix inequalities generate four corner limits, which are $\eta_r = \eta_r^{min}$ at U_x^{min} and U_x^{max} and $\eta_r = \eta_r^{max}$ at U_x^{min} and U_x^{max} . By solving for a $P \succ 0$ that satisfies four equations in (6.22) and (6.24), any operating point between these four corner points is asymptotically stable. For example, a P that proves asymptotic stability for $0.15 \leq \eta_r \leq 1$ and vehicle speed of $30 \leq U_x \leq 50$ m/s is shown below.

$$P = 10^5 \begin{bmatrix} 0.0327 & 0.0041 & 0.1103 & -0.0078 \\ 0.0041 & 0.0135 & 0.0464 & -0.0155 \\ 0.1103 & 0.0464 & 5.8945 & 0.1227 \\ -0.0078 & -0.0155 & 0.1227 & 0.0790 \end{bmatrix} \quad (6.25)$$

This P matrix shows that the steering controller can stabilize the vehicle (in the Lyapunov sense) in a wide range of conditions, ranging from a small rear slip angle ($\eta_r = 1$) to a large rear slip angle where the tires are highly saturated beyond their peak tire force (see $\eta_r = 0.15$ in Fig. 6.3).

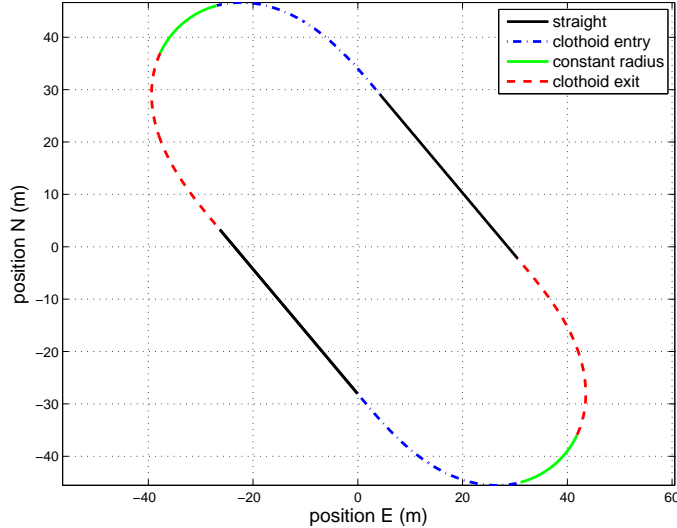


Figure 6.6: Map used in the simulation and the experimental results in Section 6.3.1, plotting on North and East coordinates

6.2 Simulation results

To determine if the controller behaves as expected, a Matlab code was written using Euler integration to simulate the system dynamics. In this simulation, a four-wheel vehicle model (see parameters in Table B.1) with no weight transfer was used together with a nonlinear brush tire Fiala model [60] that takes both longitudinal and lateral forces into account. The Fiala brush tire model used in the simulation has $\mu_s = \mu_k = 0.8$, where μ_s and μ_k are static and kinetic friction coefficients, respectively. Some simplifications were made regarding how the engine and brake system generate torque at the road wheels. After the controller commands longitudinal force, different first-order filters were used to simulate the delay from the engine and the brake system. In addition, we assumed that the amount of torque generated from the engine would only change according to the gear ratio, i.e., there is no torque variation due to the engine speed. The 180 degree hairpin in Fig. 6.6 is used for this analysis, where the path transitions from a straight to a hairpin turn at distance $s = 40$ m.

The simulation results when the controller operates at the friction limit ($\mu = 0.8$)

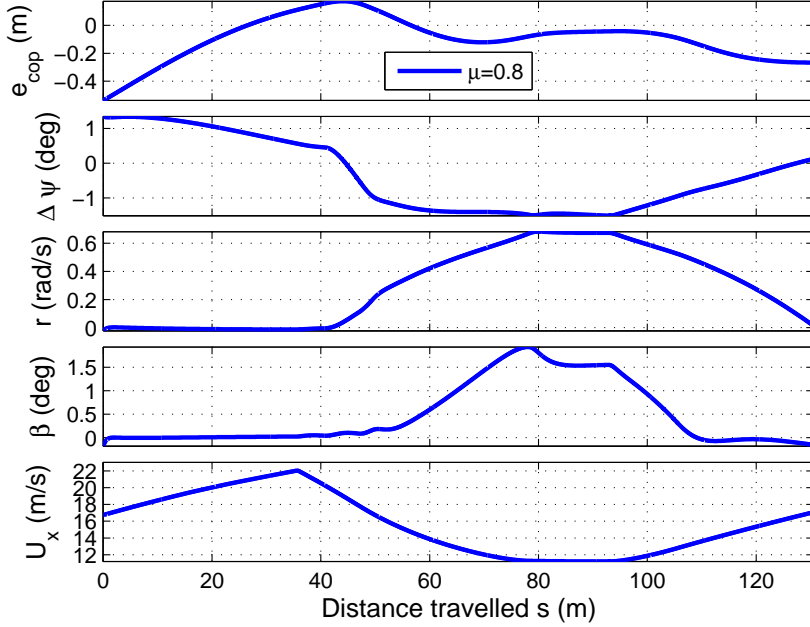


Figure 6.7: Vehicle’s state variables from the simulation

are shown in Figs. 6.7 to 6.10. As expected, the controller tracks the path with minimal tracking error (Fig. 6.7) while operating at the friction limits (Fig. 6.10).

The following sections explore the controller’s sensitivity to the estimated friction value and the effect of longitudinal weight transfer.

6.2.1 Effects of estimated friction value on the controller’s performance

The sensitivity of the estimated friction used in the controller is explored in this section. In this simulation, the controller used different estimated friction values as shown in Table 6.2. As expected, the results show that when the estimated friction is overpredicted, the tracking error grows nonlinearly. There are significant differences in the tracking errors between increasing the estimated friction value from $\mu = 0.8$ to 0.85 and from $\mu = 0.85$ to 0.875. These differences indicate the importance and the delicacy of choosing the controller estimated friction value as the error could grow

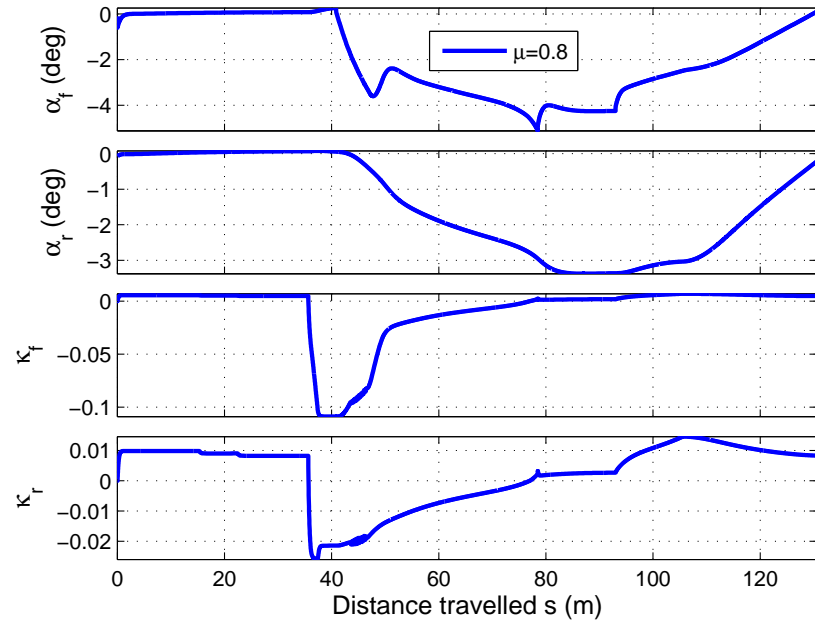


Figure 6.8: Vehicle's slips from the simulation

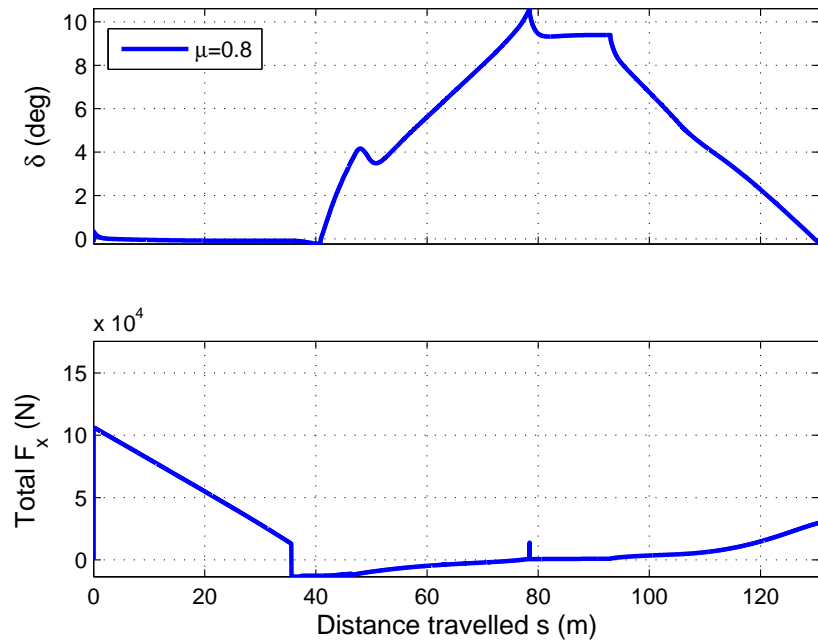


Figure 6.9: Controller's inputs from the simulation

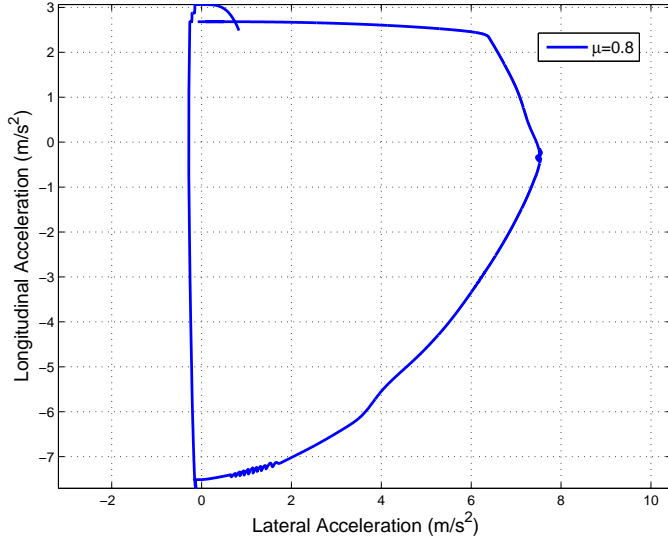


Figure 6.10: “*g-g*” diagram from the simulation

rapidly when the controller overpredicts its limits. When the estimated friction is overpredicted, the vehicle enters a corner at an excessive speed, causing it to slide and deviate from the desired path. Using a real-time friction estimation can also prevent the controller from operating over its friction limits.

The simulation also provides two additional insights into how the controller operates. First, if the vehicle is operating at its friction limits through accurate feed-forward commands, then there is little tire force left. This prevents the feedback

Table 6.2: Friction sensitivity

μ^a	$e_{cop}^{max}{}^b$	$\Delta\psi^{max}{}^c$
0.75	0.30	1.9
0.8	0.27	1.5
0.85	1.39	3.7
0.875	8.09	16.0

^aused by the controller

^bmaximum lateral error at the COP (m), ignoring the error from the initial condition

^cmaximum heading error (deg)

controller from having sufficient tire force to make corrections. Second, the initial condition (i.e., the position and orientation of the vehicle relative to the path) affects the tracking performance of the vehicle. If the vehicle is entering a corner at its friction limits while having a large tracking error, it is difficult to minimize this error as there is no reserve tire force to make steering corrections. For instance, if the vehicle is initially inside a curve, turning less to minimize tracking error will require less tire force. However, if the vehicle is outside a curve, turning more to reduce the lateral error may not be possible because the tires may not have additional forces to turn more.

6.2.2 The importance of weight transfer

Figures 6.11 and 6.12 depict the importance of weight transfer. Similar to what we observed at Bonneville Salt Flats (Section 5.3), if the controller did not take longitudinal weight transfer into account, large tracking errors, shown in Fig. 6.11, and a large oversteering, depicted in Fig. 6.12, were observed in the simulation results. Because the controller did not take the longitudinal weight transfer into account, it used a point mass model and assumed that all tires reach their limits at once, which overpredicted the overall forces that the tires could generate. Thus, the feedforward controller assumed that the vehicle could travel at a higher speed, which eventually caused the vehicle to slide. To incorporate the longitudinal weight transfer, the method in Appendix A with the vehicle parameters in Table B.1 are used.

6.3 Experimental results

The new steering controller structure described in this chapter was test on a paved surface at Santa Clara County Fairground parking lot (see Fig. 6.6). The performance and the behavior of the baseline controller adapted from the lanekeeping steering in Section 6.1.3 are very similar to those of the original steering controller discussed in Chapter 3. This demonstrates that restructuring the steering controller in Chapter 3 into the structure described in this section does not significantly alter the system's

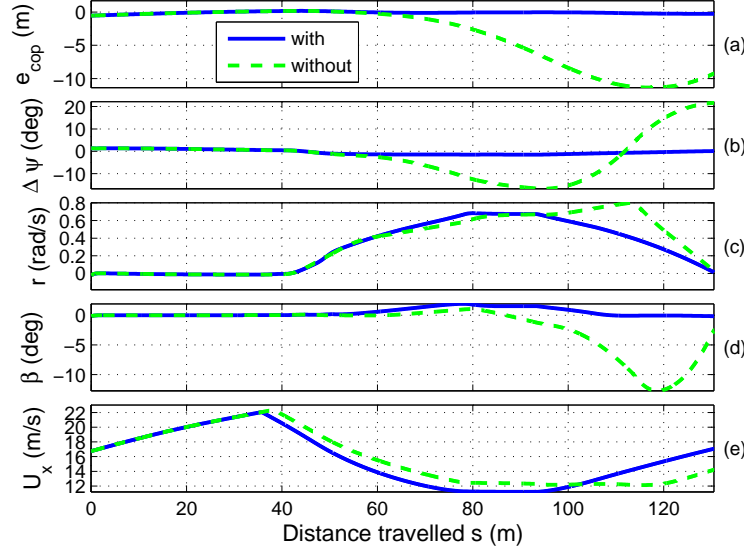


Figure 6.11: Comparison of vehicle states between with and without longitudinal weight transfer, (a-b) large errors when not taking weight transfer into account (c-e) vehicle states

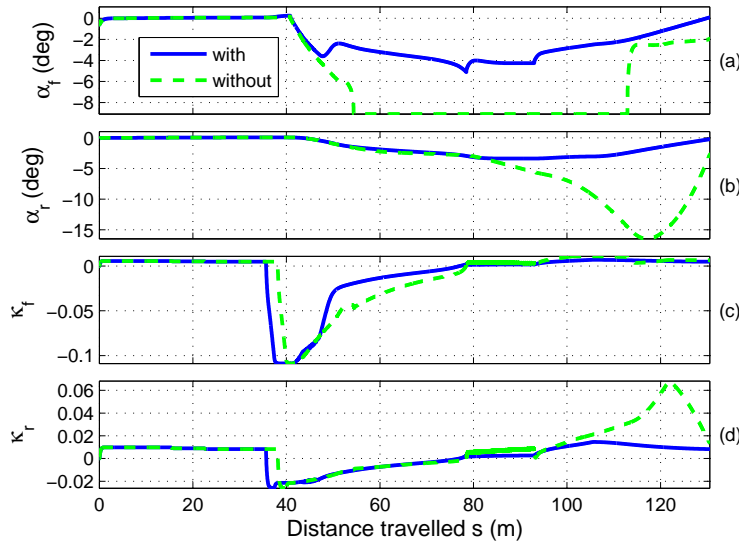


Figure 6.12: Comparison of slip between with and without longitudinal weight transfer; large oversteering occurs when the controller does not take the weight transfer into account

Table 6.3: LQR scaling factors and the result gains

Set No.	q_{11}	q_{22}	q_{33}	q_{44}	k_1	k_2	k_3	k_4	e_{cop}^{max} ^a	$\Delta\psi^{max}$ ^b
baseline lanekeeping ^c	-	-	-	-	4,000	0	75,824	9,500	0.59	2.54
linearization ^d	-	-	-	-	1,723.6	1,723.6	0	0	1.85	6.20
set 1: LQR	20	0.1	818.5	0.1	4,472	3,511	19,906	3,418	1.04	3.65
set 2: improve $\Delta\psi$	20	0	12,278	0.1	4,472	4,649	96,265	10,990	0.74	1.99
set 3: improve e_{cop}	-	-	-	-	10,000	4,649	96,265	10,990	0.38	2.68

^amaximum lateral error at the COP (m), data from one corner^bmaximum heading error (deg), data from one corner^cadapted from lanekeeping in Section 6.1.3^doutput feedback linearization in Section 6.4.2

behavior. The tracking performance of the baseline controller (in Section 6.1.3) is shown in Table 6.3, where the maximum tracking error at the COP is 0.59 m and the maximum heading error is 2.54 deg.

Figure 6.13 demonstrates how the steering controller provides yaw stability into the system. As shown in Fig. 6.13, the vehicle is driving at the limits and when a dense gravel area is reached, the friction drops. This results in oversteering during t=62.2-62.8 s and 63.9-65.2 s. Even when the rear tires have a high slip angle ($\alpha_r = 15$ deg, in Fig. 6.13c), the vehicle remains stable. The steering controller provides yaw stability through its countersteering input (Fig. 6.13b, where a positive front lateral force in a left-handed turn corresponds to a countersteer), which prevents the vehicle from spinning. The steering controller detects the change in the heading error $\Delta\psi$ and reduces the amount of steering input through gain k_3 . Even though the proof in Section 6.1.5 uses small angle approximations, the results in Fig. 6.13 demonstrate system yaw stability even when $\alpha_r = -15$ deg and $\Delta\psi = 15$ deg (not shown). Most of the steering feedback controller commands come from the lateral tracking error (gain k_1) and the heading error (gain k_3).

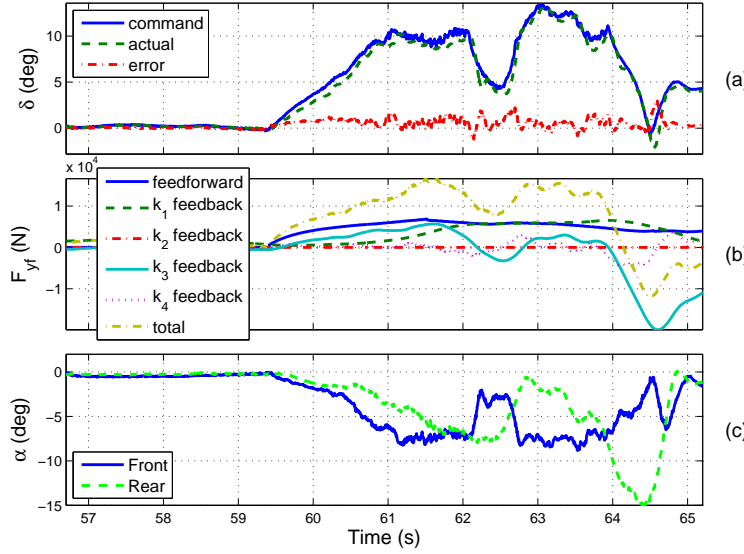


Figure 6.13: Steering controller command (a) road wheel angle (b) feedback commands from different states (c) lateral slip

6.3.1 Comparison with simulation results

Figure 6.14 to 6.17 compare the results between the experiment and the simulation when the path in Fig. 6.6 was used. The simulation uses the initial condition obtained from the first time step of the experimental results. Both results use the same steering controller adapted from the lanekeeping steering system described in Section 6.1.3, and the controller uses an estimated friction value of 0.8.

The magnitudes of the tracking errors and the vehicle states in Figs. 6.14 and 6.15 in both the simulation and the experimental results are comparable. There is a small discrepancy, especially in the lateral error e_{cop} of the straight section (Fig. 6.14a when $s < 40$ m), due to some error in the heading measurement, which is only good to about 0.5 degree. Consequently, the system in the experiment finds an equilibrium other than zero lateral error. Nevertheless, the maximum magnitudes of the lateral and heading errors in the experiment (0.31 m and 1.5 degree) are comparable to the simulation values (0.18 m and 1.4 degree).

The steering and longitudinal inputs also show similar controller commands. The

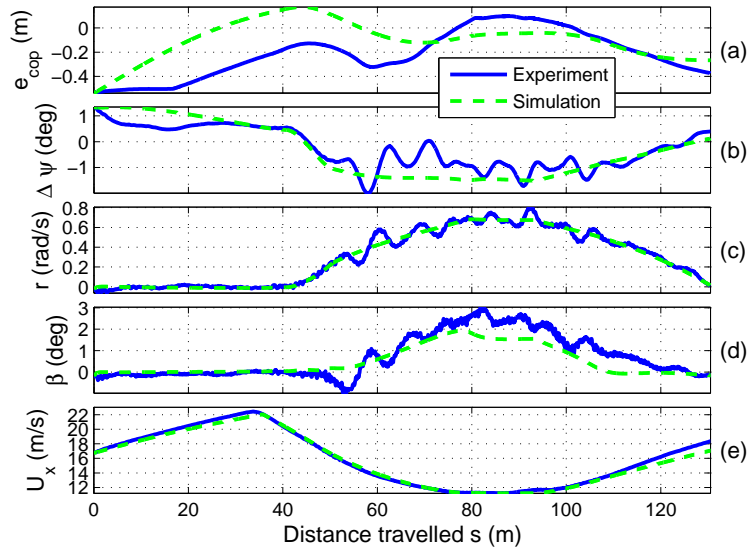


Figure 6.14: Comparison of vehicle states between simulation and experimental results

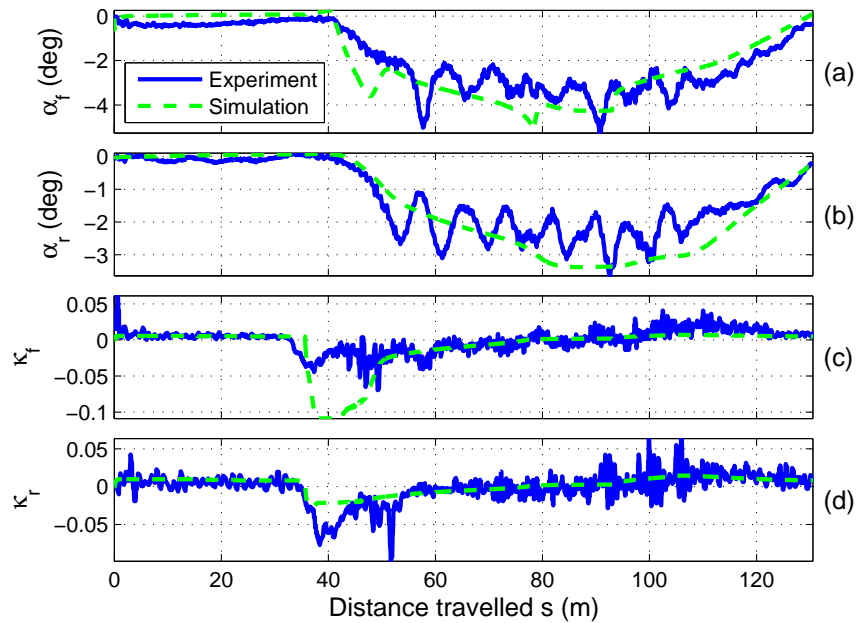


Figure 6.15: Comparison of slip between simulation and experimental results

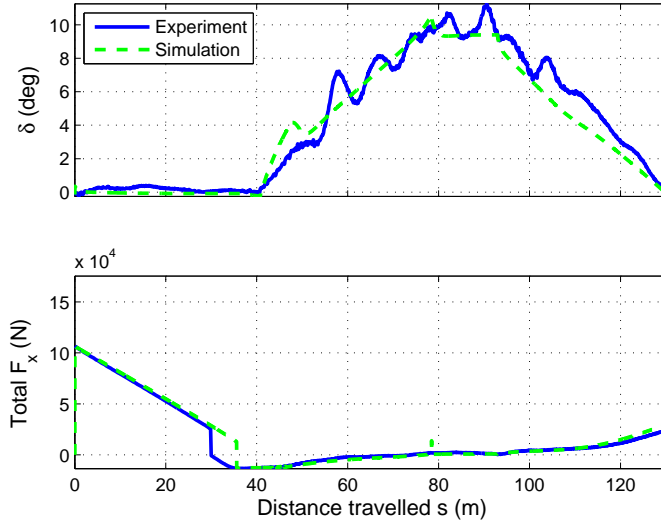


Figure 6.16: Comparison of inputs between simulation and experimental results

controller in the simulation brakes much later than the controller in the experiment as there is no time-delay in brake system in the simulation environment. In addition, note that there are steps in the steering input at $s=78$ and 93 m (Fig. 6.16). These steps are due to the discontinuity in the rate of curvature change, when the segment changes between a clothoid and a constant radius segments as mentioned in Section 6.4.3.

Both simulation and experimental results in Fig. 6.17 show that the controller operates the vehicle at the limits as expected. Furthermore, even in the simulation environment, the vehicle's acceleration will not track the friction limit perfectly. This is because any steering correction made by the feedback steering controller affects the vehicle's lateral acceleration a_y . If the vehicle is not tracking the desired path perfectly, any deviation from the path changes the turning radius, which causes the lateral acceleration to deviate from the desired value.

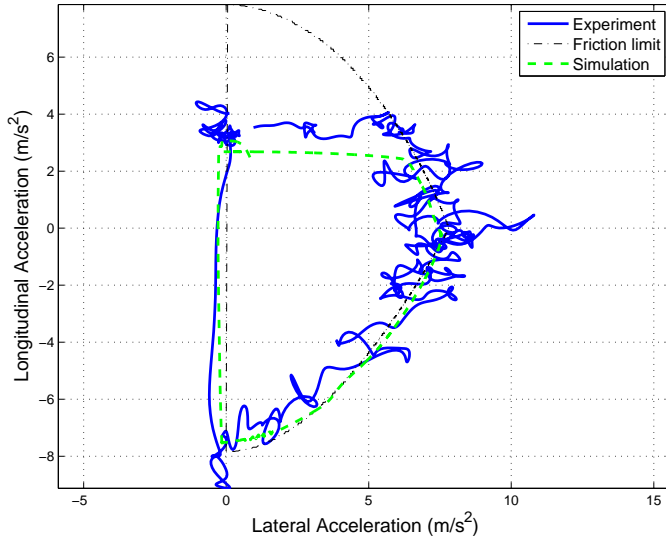


Figure 6.17: Comparison of “ g - g ” diagrams between simulation and experimental results

6.4 Steering gain analysis

With the equations of motion in a state-space form, there are multiple approaches to finding a set of feedback gains. In addition to deriving a set of gains from the lanekeeping steering feedback as mentioned in Section 6.1.3, this section explores sets of gains derived from using an energy-like Lyapunov function, from output feedback linearization and from using a Linear Quadratic Regulator (LQR) method. The gains derived from these techniques were tested on a paved surface with gravel on top, the same surface used in the experiments shown in Section 5.4 and 6.3.

6.4.1 Choosing gains for Lyapunov stability

Since a numerical method was successfully used in Section 6.1.5 to find a matrix P to prove that the system is asymptotically stable, another approach to finding a set of gains from an analytic Lyapunov function is investigated. Using an analytic Lyapunov function approach could potentially provide a set of constraints for designing the steering feedback gains, while guaranteeing the system’s stability. This will eliminate

the process of “guess and check” in Section 6.1.5 where a set of gains is found and (6.22) and (6.24) are solved to find a matrix P .

An energy-like Lyapunov function was chosen, and a set of constraints that makes the system asymptotically stable was found. However, at the end of this section, the set of constraints found from the analytic Lyapunov function is impractical because it is impossible to find a set of fixed gains that works in a wide range of operating conditions.

A Lyapunov function that is related to kinetic (speed square) and potential energy (displacement square) was utilized [65], i.e.,

$$\mathcal{L} = x^T P x = \frac{1}{2} m G_s \dot{e}_{cop}^2 + \frac{1}{2} I_{zz} \Delta \psi^2 + \frac{1}{2} \tilde{k}_1 e_{cop}^2 + \frac{1}{2} \tilde{k}_2 \Delta \psi^2 + \tilde{k}_3 e_{cop} \Delta \psi , \quad (6.26)$$

where the constants \tilde{k}_1 to \tilde{k}_3 represent the energy scaling factor (all are positive values) and $G_s > 0$ is the positive inertial scaling factor, similar to what Switkes used in [72]. With the Lyapunov function in (6.26), the matrix P is found from $\mathcal{L} = x^T P x$ in (6.26).

$$P = \begin{bmatrix} \frac{1}{2} \tilde{k}_1 & 0 & \frac{1}{2} \tilde{k}_3 & 0 \\ 0 & \frac{1}{2} m G_s & 0 & 0 \\ \frac{1}{2} \tilde{k}_3 & 0 & \frac{1}{2} \tilde{k}_2 & 0 \\ 0 & 0 & 0 & \frac{1}{2} I_{zz} \end{bmatrix} \quad (6.27)$$

To check the positive definiteness of matrix P , Sylvester’s theorem can be used [70]. It states that if P is symmetric, it is sufficient and necessary for P to be positive definite if all of its principal minors are strictly positive. From inspection, since the constants \tilde{k}_1 to \tilde{k}_3 are positive, matrix P is positive definite if and only if

$$\begin{vmatrix} \frac{1}{2}\tilde{k}_1 & 0 & \frac{1}{2}\tilde{k}_3 \\ 0 & \frac{1}{2}mG_s & 0 \\ \frac{1}{2}\tilde{k}_3 & 0 & \frac{1}{2}\tilde{k}_2 \end{vmatrix} > 0$$

$$\tilde{k}_1\tilde{k}_2 - \tilde{k}_3^2 > 0.$$
(6.28)

This constraint will be revisited after the analysis of $\dot{\mathcal{L}}$. As mentioned in Section 6.1.5, in addition to $\mathcal{L} > 0$, the system is asymptotically stable if $\dot{\mathcal{L}} < 0$. From (6.26), the derivative of the Lyapunov function is equal to

$$\dot{\mathcal{L}} = mG_s \dot{e}_{cop} \ddot{e}_{cop} + I_{zz} \Delta\dot{\psi} \Delta\ddot{\psi} + \tilde{k}_1 e_{cop} \dot{e}_{cop} + \tilde{k}_2 \Delta\psi \Delta\dot{\psi} + \tilde{k}_3 \dot{e}_{cop} \Delta\psi + \tilde{k}_3 e_{cop} \Delta\dot{\psi}. \quad (6.29)$$

Substituting \ddot{e}_{cop} and $\Delta\ddot{\psi}$ of the closed-loop system in (6.17) gives

$$\begin{aligned} \dot{\mathcal{L}} = & mG_s \dot{e}_{cop} \left(-\frac{k_1 L}{bm} e_{cop} - \frac{k_2 L}{bm} \dot{e}_{cop} - \frac{k_3 L}{bm} \Delta\psi - \frac{k_4 L}{bm} \Delta\dot{\psi} \right) \\ & + I_{zz} \Delta\dot{\psi} \left(-\frac{k_1 a}{I_{zz}} e_{cop} - \frac{k_2 a}{I_{zz}} \dot{e}_{cop} + \frac{b\eta_r C_r}{I_{zz} U_x} \dot{e}_{cop} - \frac{k_3 a}{I_{zz}} \Delta\psi - \frac{b\eta_r C_r}{I_{zz}} \Delta\psi - \frac{k_4 a}{I_{zz}} \Delta\dot{\psi} \right. \\ & \left. - \frac{L b \eta_r C_r}{I_{zz} U_x} \Delta\dot{\psi} \right) + \tilde{k}_1 e_{cop} \dot{e}_{cop} + \tilde{k}_2 \Delta\psi \Delta\dot{\psi} + \tilde{k}_3 \dot{e}_{cop} \Delta\psi + \tilde{k}_3 e_{cop} \Delta\dot{\psi}. \end{aligned} \quad (6.30)$$

To analyze the value of $\dot{\mathcal{L}}$ in (6.30), the equation is rearranged into a matrix form of $\dot{\mathcal{L}} = -z^T Q z$, where z is the vehicle state variables vector. If $Q \succ 0$, then $\dot{\mathcal{L}} < 0$ for all nonzero z . To simplify the analysis, the cross-term $\frac{1}{2}\tilde{k}_3 e_{cop} \Delta\psi$ was used in (6.26) and the gains that eliminate all the terms associated with e_{cop} from (6.30) were chosen. For instance, e_{cop} is eliminated from (6.30) when the scaling factor \tilde{k}_1 to \tilde{k}_3 and the controller gains k_1 and k_3 have the following relation:

$$\begin{aligned}\tilde{k}_1 &= \frac{k_1 L}{b} G_s \\ \tilde{k}_3 &= k_1 a = \frac{k_3 L}{b} G_s \\ \tilde{k}_2 &= k_3 a + b\eta_r C_r.\end{aligned}\tag{6.31}$$

This implies that gain $k_3 = k_1 \frac{ab}{LG_s}$; or effectively, the lookahead distance x_{la} is constrained by $(x_{la} - a) = \frac{ab}{LG_s}$. The ability to scale G_s allows some flexibility in choosing x_{la} in the steering controller, i.e., choosing the lookahead distance. With the gains in (6.31), the derivative of the Lyapunov function is equal to

$$\begin{aligned}\dot{\mathcal{L}} &= G_s \dot{e}_{cop} \left(-\frac{k_2 L}{b} \dot{e}_{cop} - \frac{k_4 L}{b} \Delta \dot{\psi} \right) + \Delta \dot{\psi} \left(-k_2 a \dot{e}_{cop} + \frac{b\eta_r C_r}{U_x} \dot{e}_{cop} - k_4 a \Delta \dot{\psi} - \frac{Lb\eta_r C_r}{U_x} \Delta \dot{\psi} \right) \\ &= - \begin{bmatrix} \dot{e}_{cop} & \Delta \dot{\psi} \end{bmatrix} \begin{bmatrix} \frac{k_2 L G_s}{b} & \frac{k_4 L G_s}{2b} + \frac{k_2 a}{2} - \frac{b\eta_r C_r}{2U_x} \\ \frac{k_4 L G_s}{2b} + \frac{k_2 a}{2} - \frac{b\eta_r C_r}{2U_x} & k_4 a + \frac{Lb\eta_r C_r}{U_x} \end{bmatrix} \begin{bmatrix} \dot{e}_{cop} \\ \Delta \dot{\psi} \end{bmatrix}.\end{aligned}\tag{6.32}$$

Thus, the system is Lyapunov stable if

$$Q = \begin{bmatrix} \frac{k_2 L G_s}{b} & \frac{k_4 L G_s}{2b} + \frac{k_2 a}{2} - \frac{b\eta_r C_r}{2U_x} \\ \frac{k_4 L G_s}{2b} + \frac{k_2 a}{2} - \frac{b\eta_r C_r}{2U_x} & k_4 a + \frac{Lb\eta_r C_r}{U_x} \end{bmatrix} \succ 0.\tag{6.33}$$

By using Sylvester's theorem, the matrix in (6.33) is positive definite if $\frac{k_2 L G_s}{b} > 0$ and the determinant of the matrix is positive. Consequently, this produces another two constraints that if the gains k_2 and k_4 satisfy (6.34), then $\dot{\mathcal{L}} < 0$.

$$k_2 > 0\tag{6.34}$$

$$z(k_2, k_4) = \left(\frac{k_2 L G_s}{b} \right) \left(k_4 a + \frac{Lb\eta_r C_r}{U_x} \right) - \left(\frac{k_4 L G_s}{2b} + \frac{k_2 a}{2} - \frac{b\eta_r C_r}{2U_x} \right)^2 > 0$$

In addition to checking that $\dot{\mathcal{L}} < 0$, the value of the Lyapunov function has to be positive, that is $\mathcal{L} = x^T P x > 0$. Consequently, to check the positive definiteness

of P , the gains in (6.31) are substituted into (6.28) to obtain

$$\begin{aligned} \left(\frac{k_1 L}{b} G_s\right)(k_3 a + b\eta_r C_r) - (k_1 a)^2 &> 0 \\ \left(\frac{k_1 L}{b} G_s\right)\left(k_1 \frac{ab}{LG_s} a + b\eta_r C_r\right) - (k_1 a)^2 &> 0 \\ \left(\frac{k_1 L}{b} G_s\right)(b\eta_r C_r) &> 0. \end{aligned} \quad (6.35)$$

Equation (6.35) is always true because all the values on the left hand side are positive, although η_r could approach zero when the rear tires are highly saturated.

Thus, if a set of gains that satisfies (6.31) and (6.34) is found, then the system is Lyapunov stable. However, there is a challenge in finding a set of gains that works over a wide range of conditions as (6.34) depends on both vehicle speed U_x and the state of the rear tires η_r . Figure 6.18 demonstrates the difficulty of choosing gain k_2 when gain k_4 is fixed. The range of k_2 that makes $z(k_2, k_4) > 0$ in (6.34) changes according to the operating condition (U_x and η_r), and it is difficult to find a fixed gain k_2 that works in a wide range of operating conditions. Because of this difficulty, other approaches are considered for finding a set of fixed-gains for the full-state steering feedback controller and the numerical method discussed in Section 6.1.5 is used for the stability analysis.

6.4.2 Output feedback linearization

An output feedback linearization technique can be used to shape the dynamics of the output state (i.e., e_{cop}), if the internal dynamics of the system are stable [70]. In theory, this method can drive the error e_{cop} down to zero if there are no disturbances in the system and the model of the system is perfectly known.

From (6.15), the lateral tracking error e_{cop} can be written as

$$\ddot{e}_{cop} = \frac{L}{bm} F_{yf}^{FB}. \quad (6.36)$$

We can find the feedback lateral force F_{yf}^{FB} to shape the dynamics of e_{cop} . For instance, if second-order dynamics with two poles at $-1 \pm i$ is desired:

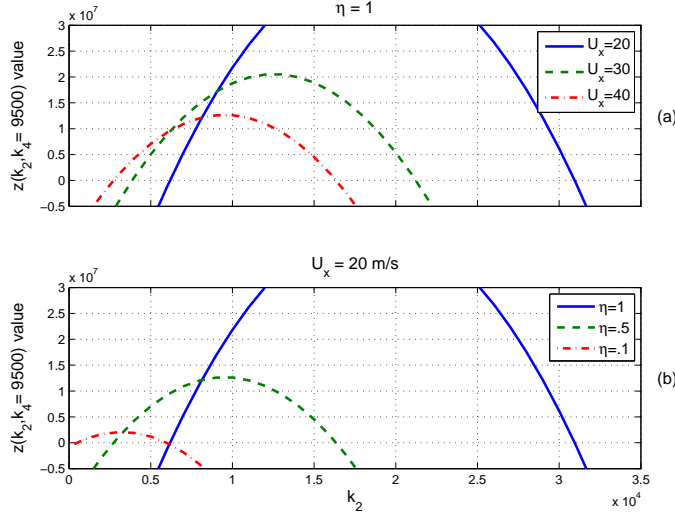


Figure 6.18: Showing the value of $z(k_2, k_4)$ in (6.34), (a) varies vehicle speed U_x (b) varies η_r

$$\ddot{e}_{cop} + 2\dot{e}_{cop} + 2e_{cop} = 0 , \quad (6.37)$$

the required feedback lateral force F_{yf}^{FB} can be found from substituting (6.37) into (6.36).

$$\begin{aligned} \ddot{e}_{cop} &= \frac{L}{bm} F_{yf}^{FB} = -2\dot{e}_{cop} - 2e_{cop} \\ F_{yf}^{FB} &= -2\frac{bm}{L}\dot{e}_{cop} - 2\frac{bm}{L}e_{cop} . \end{aligned} \quad (6.38)$$

Comparing (6.38) to (6.16), this is similar to having a set of gains of $k_1 = k_2 = 2bm/L$ and $k_3 = k_4 = 0$.

With F_{yf}^{FB} in (6.38), e_{cop} will behave as a second-order system in (6.37), if the internal dynamics are stable. The internal dynamics, which come from the heading error $\Delta\psi$ dynamics in this case, can be checked from (6.15). The feedback force F_{yf}^{FB} derived in (6.38) is used and the effect of road curvature is ignored. With the feedback force in (6.38), the outer dynamics of the lateral error e_{cop} are stable and e_{cop} will

eventually go to zero. Thus, when analyzing the stability of the internal dynamics, any terms associated with the dynamics of e_{cop} are set to zero [70]:

$$\begin{aligned}\ddot{\Delta\psi} &= \frac{b\eta_r C_r}{I_{zz} U_x} \dot{e}_{cop} - \frac{b\eta_r C_r}{I_{zz}} \Delta\psi - \frac{\dot{L}b\eta_r C_r}{I_{zz} U_x} \Delta\dot{\psi} + \frac{a}{I_{zz}} F_{yf}^{FB} \\ \ddot{\Delta\psi} &= \frac{b\eta_r C_r}{I_{zz} U_x} \dot{e}_{cop} - \frac{b\eta_r C_r}{I_{zz}} \Delta\psi - \frac{\dot{L}b\eta_r C_r}{I_{zz} U_x} \Delta\dot{\psi} + \frac{a}{I_{zz}} (-2\frac{bm}{L} \dot{e}_{cop} - 2\frac{bm}{L} e_{cop}) \\ \ddot{\Delta\psi} &= -\frac{b\eta_r C_r}{I_{zz}} \Delta\psi - \frac{\dot{L}b\eta_r C_r}{I_{zz} U_x} \Delta\dot{\psi}.\end{aligned}\quad (6.39)$$

From Routh's stability criterion [14], the internal dynamic of the heading error $\Delta\psi$ is stable if $b\eta_r C_r / I_{zz}$ and $\dot{L}b\eta_r C_r / I_{zz} U_x$ are positive. In these two terms, only η_r and U_x can change, and neither can have a negative value (assuming that the vehicle travels forward). Thus, the internal dynamics of the system are stable. However, compared to a mass-spring-damper model, the spring stiffness and the damping value of the internal dynamics approach zero when the rear tires are highly saturated ($\eta_r \rightarrow 0$). In addition, the system's damping reduces as the vehicle speed U_x increases.

Furthermore, using a linear analysis has limitations when considering the stability of the internal dynamics in (6.39). The coefficients η_r and U_x are not constant values; thus, the rates of change of these two values can influence the stability of the system.

Experimental results from output feedback linearization

The previous section showed that the gains derived from output feedback linearization should drive the e_{cop} down to zero and have stable internal dynamics. In Fig. 6.19 and Fig. 6.20, large tracking error is observed when using gains derived from output feedback linearization. This technique works well on a straight line, as shown in Fig. 6.19; however, when road curvatures are presented as disturbances injected into the system, the performance of the system degrades.

Figure 6.20 and 6.21 demonstrate how the controller behaves. The vehicle understeers during $t=43.6-45.2$ s and oversteers during $t=46.4-47.4$ s, as shown by the slip norms in Fig. 6.20e. The output feedback linearization has a countersteering characteristic even though the feedback controller does not contain any heading information

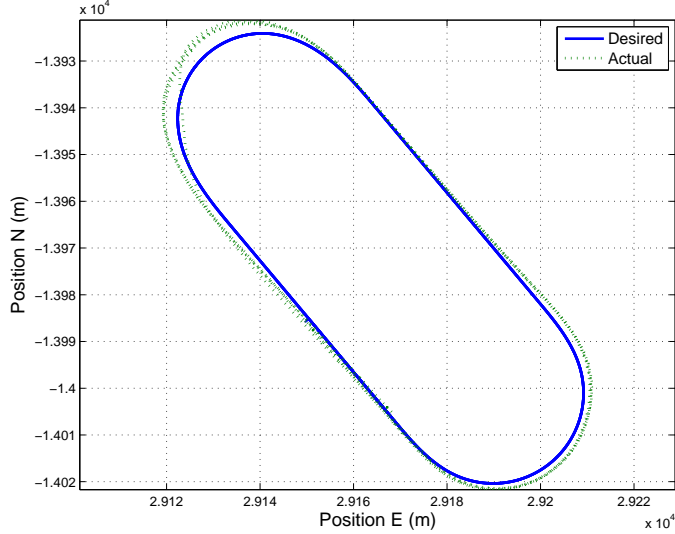


Figure 6.19: Showing tracking performance when using output feedback linearization

($\Delta\psi$ nor $\dot{\Delta\psi}$). During oversteering, the steering input δ reduces (see Fig. 6.21a). Although e_{cop} contains some information of the vehicle heading because it has a lookahead distance of x_{cop} , the feedback steering input did not provide any countersteering input in this case as F_{yf} remains positive (see Fig. 6.21b). The countersteering characteristic actually comes from a decrease in the vehicle's side slip (see Fig. 6.21c), which reduces the steering input δ in (6.19).

6.4.3 Linear Quadratic Regulator (LQR)

A Linear Quadratic Regulator (LQR) technique is employed to find a set of fixed gains for the steering controller. This technique finds a set of gains that minimize the tracking error states x and the actuator input u [14]. The algorithm minimizes a cost function J , where

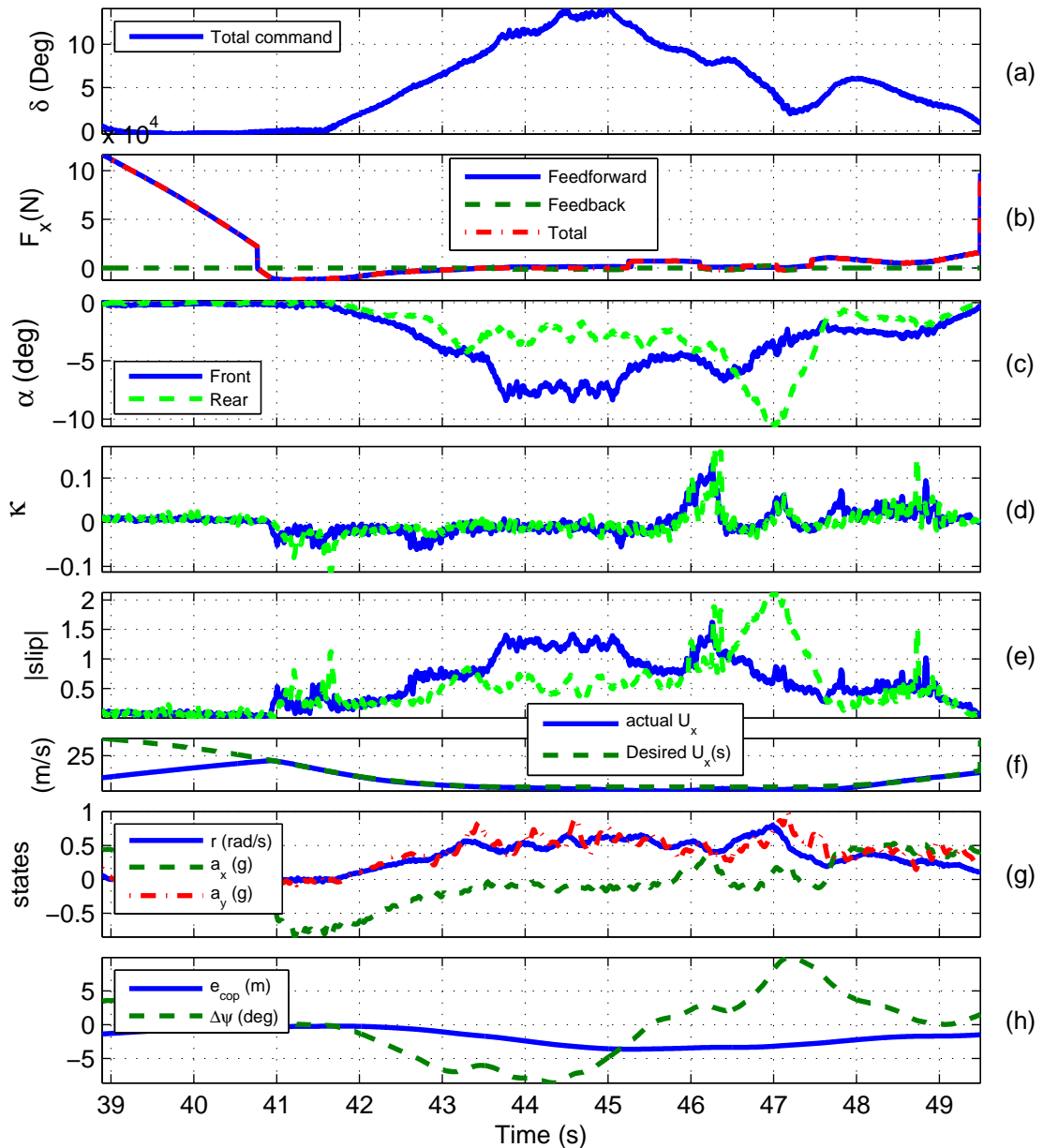


Figure 6.20: Controller commands (a-b) and vehicle states (c-h) when using output feedback linearization

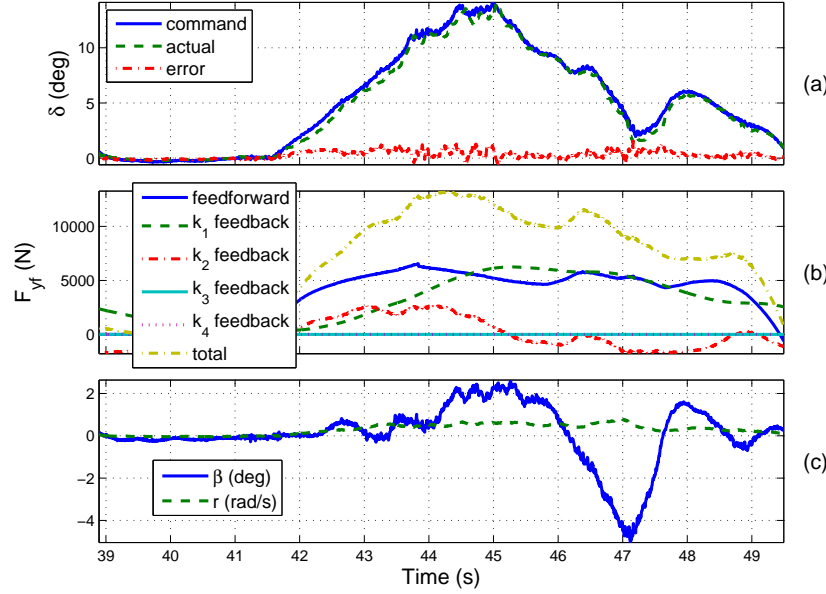


Figure 6.21: Steering controller command using output feedback linearization (a) road wheel angle (b) feedback commands from different states (c) vehicle states

$$\begin{aligned}
 J &= \int_0^{\infty} (x^T Q x + u^T R u) dt , \\
 Q &= \begin{bmatrix} q_{11} & 0 & 0 & 0 \\ 0 & q_{22} & 0 & 0 \\ 0 & 0 & q_{33} & 0 \\ 0 & 0 & 0 & q_{44} \end{bmatrix} ,
 \end{aligned} \tag{6.40}$$

q_{ii} is the scaling factor of each state x_i , and $R = 10^{-6}\text{N}^{-2}$ is the scaling factor of the steering input F_{yf} . The small value of R indicates that more emphasis is put on the tracking states at the expense of large control input. Choosing a different weight q_{ii} for each state affects the gains found by the algorithm. For the first iteration (set 1: LQR), a set of q_{ii} was defined from the inverse of the maximum acceptable value of x_i with additional scaling factors to add a relationship between each state x_i . Various weight factors and gains are shown in Table 6.3. The system matrix was used in Matlab LQR command [32] to find a set of gains that can cope with vehicle sliding

at high speed ($U_x = 50 \text{ m/s}$ and $\eta_r = 0.1$).

Different weights on q_{ii} are explored, and the method of finding a matrix P in Section 6.1.5 is used to check the system's stability. With gain set 1: LQR in Table 6.3, a matrix P was not found for the operating range of $30 \leq U_x \leq 50 \text{ m/s}$ and $0.15 \leq \eta_r \leq 1$. A matrix P was found only when a smaller operating region of the rear tires was used, i.e., when $0.4 \leq \eta_r \leq 1$ (see Fig.6.3) or when the rear tires are not highly saturated.

In order to find a matrix P that proves that the system is asymptotically stable for $30 \leq U_x \leq 50 \text{ m/s}$ and $0.15 \leq \eta_r \leq 1$, significant weight has to be put on $\Delta\psi$ (q_{33}) to produce high k_3 value. This high k_3 value is similar to a steering controller that has a long lookahead distance. As shown by Rossetter [66], a longer lookahead distance adds yaw stability into the system as the steering feedback becomes more sensitive to vehicle yaw. With high k_3 value in gain set 2: improve $\Delta\psi$ and 3: improve e_{cop} , a matrix P is found for the given operating condition. For gain set 3: improve e_{cop} , the gain for the lateral tracking error e_{cop} (k_1) is increased to improve the lateral tracking performance.

Experimental results from gains derived from LQR

Table 6.3 demonstrates the tracking performance of each set of gains. These numbers were deduced from the experimental data that resulted from the vehicle going around the same corner. Because of the variations on the testing surface, the tracking performance can vary between each lap.

Figures 6.22 to 6.24 show the performance of the controller when gain set 1 (LQR, Table 6.3) is used. The tracking performance is degraded when compared to the baseline lanekeeping controller, but this is expected since the gains are lower than the baseline lanekeeping controller, with the exception of k_2 .

The vehicle has some understeer during $t=54.6-55.5 \text{ s}$ as the front lateral slip grows in Fig. 6.22c, which causes a growing tracking error e_{cop} in Fig. 6.22h. The slip circle feedback controller reduces the longitudinal force to minimize this front slip in Fig. 6.22b, but the effect is small as the magnitude of the slip is not significant. The vehicle's acceleration still tracks the friction limits well, as shown Fig. 6.23.

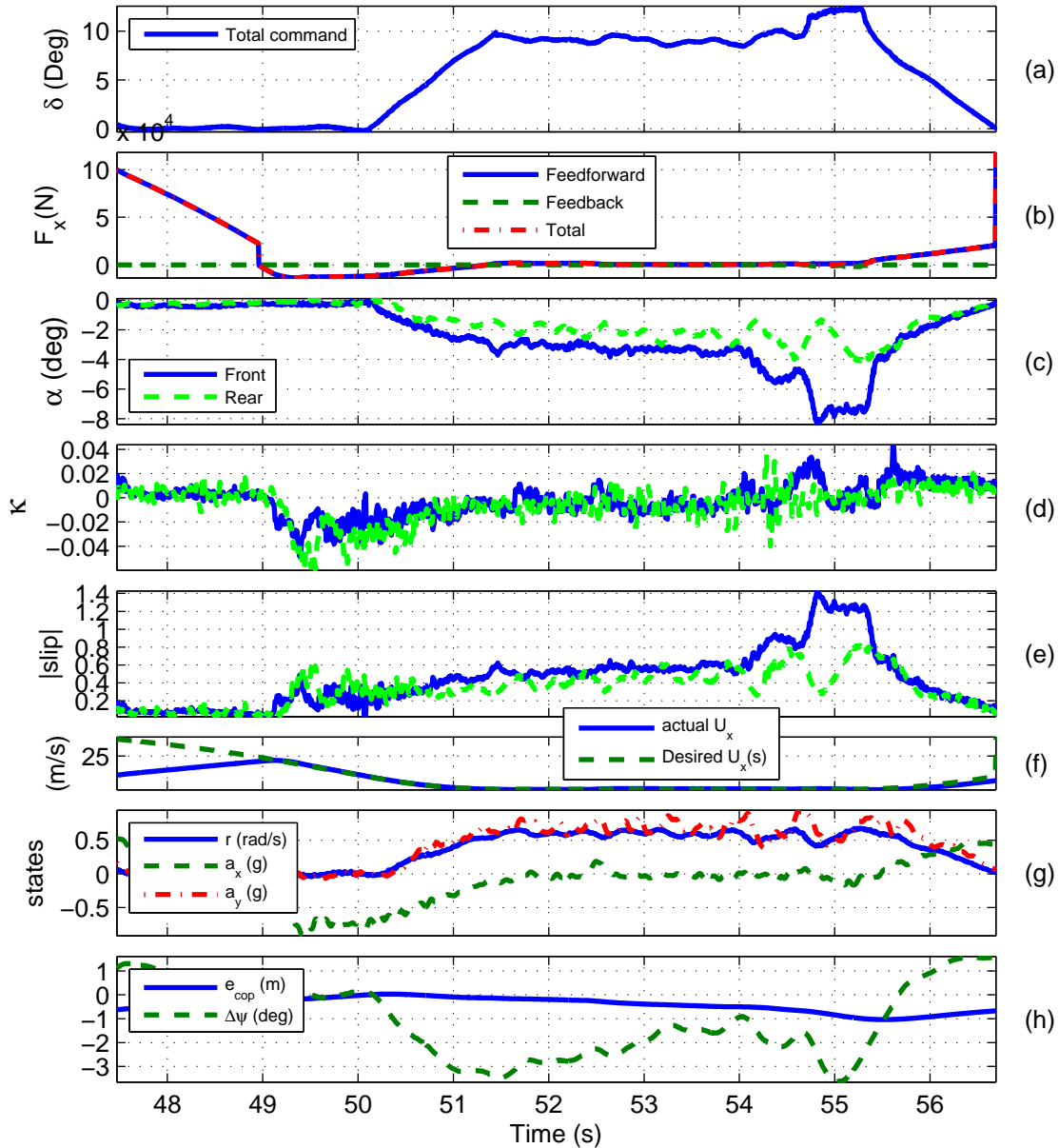


Figure 6.22: Controller commands (a-b) and vehicle states (c-h) using gain set 1: LQR

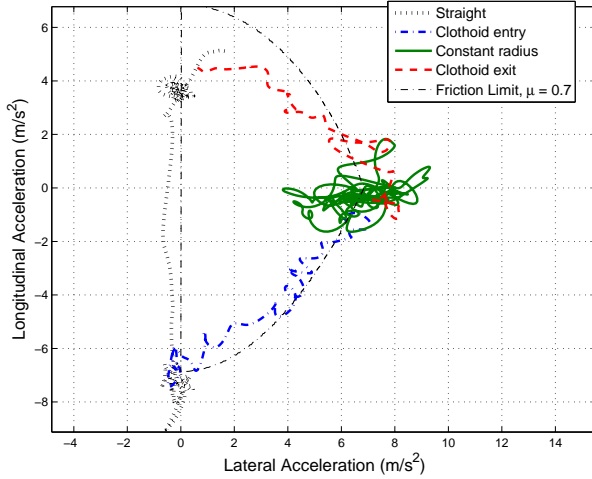


Figure 6.23: “ g - g ” diagram using gain set 1: LQR

Figure 6.24b provides an overview of how the feedforward and the feedback steering forces from each state contribute to the total steering force. There are discontinuities in the feedforward steering force at $t=51.5$ and 55.2 s (Fig. 6.24b). This is due to the discontinuity in the rate of curvature change $\dot{\mathcal{K}}$ inherited in the path when the segment changes from a clothoid curve to other types of segments (see Fig. 2.3), causing jumps in the feedforward steering force in (6.8). In addition, in Fig. 6.24b, most of the feedback steering force comes from the lateral tracking error (gain k_1).

With higher gain k_3 in gain set 2: improve $\Delta\psi$, the tracking error is reduced (Table 6.3). Nevertheless, the lateral tracking performance of gain set 2: improve $\Delta\psi$ is not as good as the tracking performance when using gains derived from lanekeeping in Section 6.1.3. To further improve the lateral tracking performance, gain set 3: improve e_{cop} , which has higher k_1 value, is explored.

In Fig. 6.25h, the tracking performance of the controller when using gain set 3: improve e_{cop} shows very good results as the maximum lateral error is less than 0.4 m, while the vehicle is driving at the friction limits, as shown in Fig. 6.26. Although the vehicle understeers during $t=52.6-52.8$ and $52-53.5$ s, from $|slip|_f > 1$ (Fig. 6.25e), the longitudinal slip circle controller reduces the amount of longitudinal force in Fig. 6.25b to minimize the understeer.

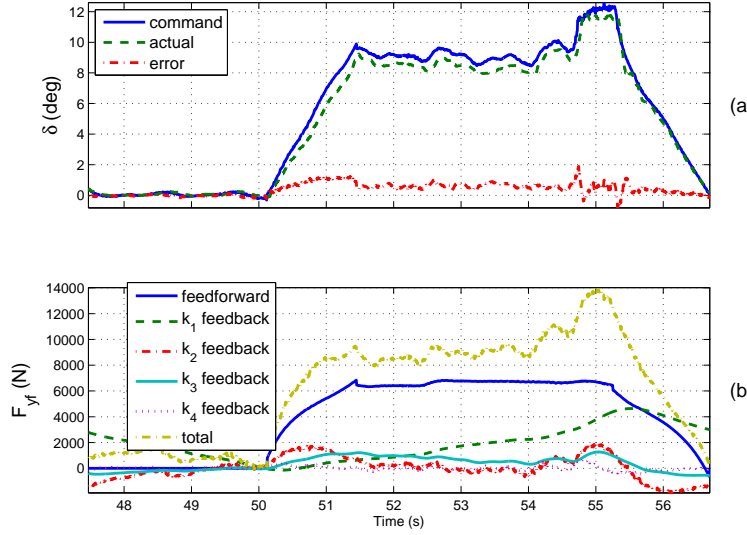


Figure 6.24: Steering controller command using gain set 1: LQR (a) road wheel angle (b) feedback commands from different states

Nevertheless, the issues associated with a high feedback controller gain appear in Fig. 6.25 to 6.27. The steering command in 6.27 is oscillatory as the feedback steering system becomes very sensitive to small tracking error, especially $\Delta\psi$ (gain k_3). In other words, the gains from LQR set 3: improve e_{cop} are too high.

The experimental results demonstrate that the gains derived from lanekeeping steering system in Section 6.1.3 perform well and no other gains derived from feedback linearization or LQR outperform the gains derived from lanekeeping system.

6.5 Conclusions

A steering controller that can provide path tracking ability as well as yaw stability was designed by incorporating the center of percussion. By eliminating the effect of dynamic rear tire force, the COP simplifies and provides robustness to the calculation of the feedforward steering controller. The COP also reduces the complexity of the state-space equation as the lateral tracking motion e_{cop} is decoupled from the vehicle's yaw motion $\Delta\psi$. A full-state feedback steering controller with constant gains was

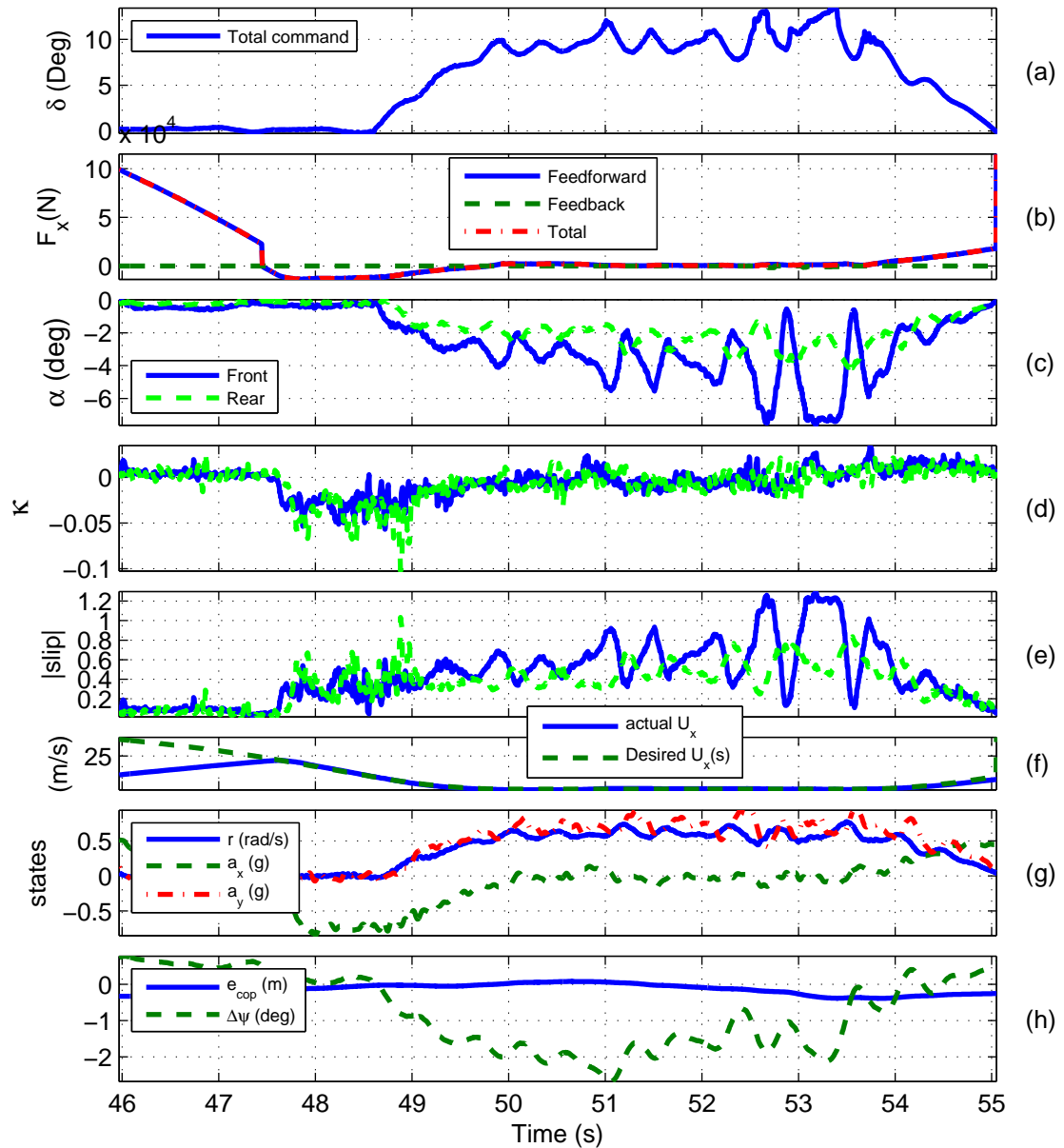


Figure 6.25: Controller commands (a-b) and vehicle states (c-h) using gain set 3: improve e_{cop}

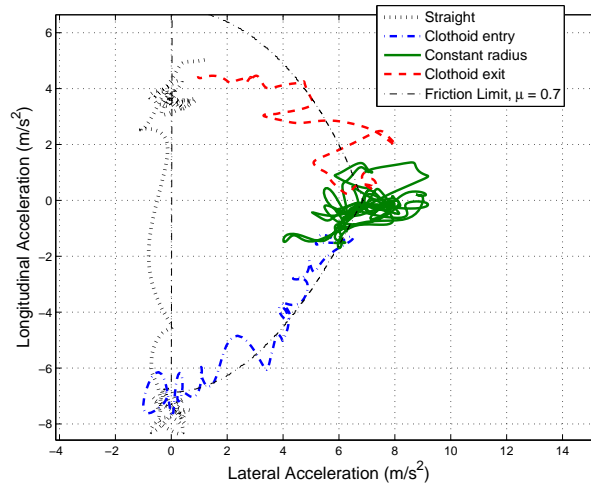


Figure 6.26: “g-g” diagram using gain set 3: improve e_{cop}

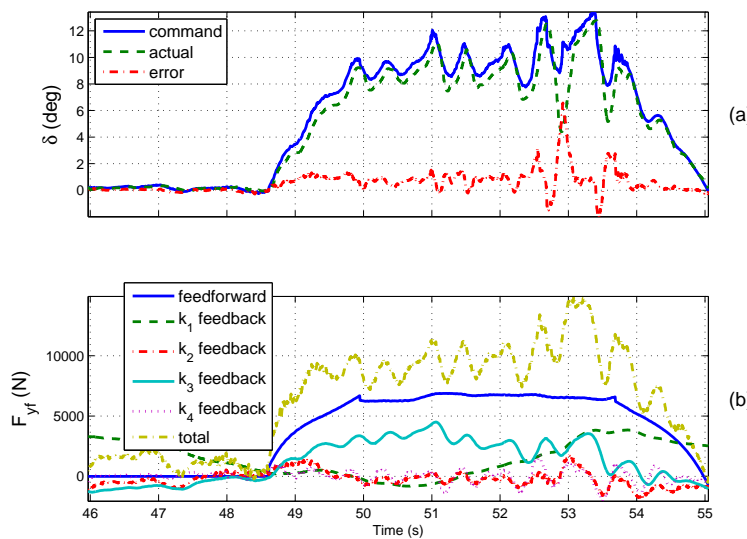


Figure 6.27: Steering controller command using gain set 3: improve e_{cop} (a) road wheel angle (b) feedback commands from different states

derived from the steering system in Chapter 3. By using Lyapunov theory, the system with this new steering controller structure is asymptotically stable even when the rear tires are highly saturated. The experimental results demonstrate the controller's ability to drive the autonomous vehicle to its friction limits with minimal tracking error. The steering controller also countersteers to maintain yaw stability when the vehicle oversteers.

A Matlab code is written to simulate the controller driving a vehicle at its friction limits. The simulation provides insights into the importance of the longitudinal weight transfer as well as the sensitivity of the controller to the available friction. After testing in a simulation environment, the new steering controller was tested in a paved surface with gravel on top. The results between the simulation and experiment correlate well, indicating that the controller behaves as expected.

Furthermore, various control techniques were used to find different sets of gains and to investigate if the controller's performance can be improved. The output feedback linearization was utilized to shape the dynamics of the lateral tracking error e_{cop} when the internal dynamics of $\Delta\psi$ is stable. A direct approach of finding a set of gains from an energy-like Lyapunov function was also explored, but it proves to be difficult to find a set of gains that works for a wide range of vehicle speeds and the state of the rear tires η_r . Finally, a Linear Quadratic Regulator (LQR) with various weights on the tracking states are used. The gains found from LQR also allow the vehicle to drive at the friction limits with small tracking errors. Nevertheless, none of the methods discussed in Section 6.4 outperforms the set of gains derived from lanekeeping with additional yaw damping in Section 6.1.3.

Chapter 7

Conclusions and Future Work

The autonomous racing controller presented in this dissertation demonstrates its ability to follow a desired path at the friction limits. Besides verified experimental results, the system was proven to be Lyapunov stable even when the rear tires are highly saturated. Combining the racing controller's ability with the path planning technology provides many exciting future opportunities for driver assistance systems and autonomous vehicles, where the systems can maximize the tire forces to track desired paths during emergency maneuvers.

Inspired by racecar drivers' behavior, the racing controller structure was separated into path information and path tracking at the limits. Besides a structure that is intuitive to understand, the path information in the racing controller can be updated in real-time to account for changes in tire-road friction or the presence of obstacles. To track a path at the limits, the racing controller was divided into steering and longitudinal (throttle and brake) controller modules, where each module consists of feedforward and feedback submodules. Mimicking racecar drivers, the controller executes trail-braking during corner-entry and throttle-on-exit during corner-exit by calculating a feedforward longitudinal input and a speed profile from a friction limit boundary on a “ $g-g$ ” diagram. When this feedforward longitudinal input is combined with the feedforward steering input, the racing controller will maximize the tire forces during cornering. To improve the system's tracking ability and stability, a longitudinal feedback submodule based on a slip circle was utilized to minimize tire slip, while

the fixed-gain full-state steering feedback submodule was added to minimize tracking error. This modular structure provides insights into the functionality of each submodule and how they work in conjunction to control a vehicle at the limits. Thus, future driver assistance systems could utilize some or all of these submodules to control a vehicle at the friction limits.

The final steering controller structure based on the center of percussion (COP) in Chapter 6 provides a systematic approach where both feedforward and feedback steering submodules track the same reference point at the COP. The main benefit of using the COP is that the rear tire forces, which are highly nonlinear at the limits and constantly changing, do not influence the lateral acceleration at the COP; thus, simplifying the feedforward steering calculation. Utilizing the COP also reduces the complexity of the system matrix used for designing a fixed-gain full-state feedback steering controller. Furthermore, the steering controller in Chapter 6 also incorporates tire nonlinearity and transient dynamics into the design. The system matrix also highlights the challenge of controlling two outputs (vehicle lateral and yaw motions) with a single front steering input, especially at the limits. Nevertheless, the system is Lyapunov stable for a wide operating range, even when the rear tires are highly saturated. This new steering controller structure was used in the final design because it provides an analytical framework that can be used to analyze all the steering controllers proposed in this dissertation and because of its proven stability at the limits.

Besides learning how each module performs together, testing an autonomous racing vehicle provides many insights into controlling a vehicle at the friction limits. At the limits, controlling a vehicle during a corner entry phase is much more challenging than a corner exit phase. If the corner entry speed is too high, no matter what the controller does, the vehicle will deviate from the desired path because there is insufficient friction forces for braking and cornering. In contrast, this dilemma does not exist in a corner exit phase. In addition, the experimental results indicate a shortfall of using a point mass assumption to design a controller that operates at the friction limits. Since a point mass model does not take longitudinal weight transfer into account, the vehicle will oversteer as the rear normal forces reduce during trail-braking.

Consequently, a quasi-static longitudinal weight transfer was proposed when calculating the feedforward longitudinal input from a “ $g-g$ ” diagram. Finally, when a complex map such as a path designed for Pikes Peak is used, employing the slip circle feedback gain (no-slip gain) to push the tires to the friction limits without monitoring vehicle speed could cause an overshoot of the entry-speed in the subsequent corner. Thus, to address this speed overshoot, the no-slip gain has been disabled, and the controller tracks a desired speed profile that looks ahead several segments in advance. Tracking the desired speed profile also ensures that the vehicle operates at the friction limits.

The experimental results from testing at the limits and discussing with racecar drivers prompt many exciting future research in vehicle control at the limits of handling. Although there are many possibilities for future research, four potential future work that could have profound impacts on the racing controller are recommended.

1. **Real-time friction estimation:** At present, the controller utilizes a priori knowledge of friction found from a ramp-steer maneuver. However, the surface friction can change and the initial friction value may not accurately represent a friction coefficient of the individual segment. Thus, using real-time friction estimation that predicts the friction value of each segment can improve the accuracy of the feedforward longitudinal controller command and minimize the tracking errors caused by overestimating friction.
2. **Smooth steering input:** Equation 6.19 is used for converting the desired front lateral force F_{yf} into the desired front steering angle command δ . From this equation, any changes in the desired lateral force directly translate into changes in the steering command, resulting in a rapid motion at the steering wheel. A smoother steering input is needed when operating at the friction limits.
3. **Recovery line:** When the controller approaches a corner at an excessive speed, large tire slip is observed as the vehicle tries to return to the desired path. However, when racecar drivers approach a corner with an excessive speed, they will generate a “recovery line” that widens the path from the intended racing line. If the controller can mimic this behavior, tracking a recovery line should

reduce tire slip. One potential approach is to utilize a slip circle to find a curvature of the recovery line that will regulate tire slip.

4. **Comparison with racecar drivers:** A comparison between the racing controller and racecar drivers driving the Audi TTS on the same track can provide directions for improvements as well as other potential future research. Moreover, other driving aspects that the current racing controller does not take into account can be learned from this comparison. For instance, racecar drivers often mention that they adjust their driving style according to the vehicle's behaviors (understeer or oversteer) as well as vehicle's types (front-wheel drive, rear-wheel drive or four-wheel drive). Although the feedback submodules in the current racing controller adjust their commands according to the vehicle's behaviors, the controller does not adjust its commands to cope with different vehicle's types. Thus, quantifying exactly what racecar drivers do in different types of vehicles and capture this behavior into the controller can prompt many interesting research questions.

A more detailed explanation of these recommendations can be found in Appendix C.

With promising results from this autonomous racing controller, I sincerely hope that this research will contribute to the future of vehicle safety systems that impact many lives.

Appendix A

Effects of Longitudinal Weight Transfer, Bank and Grade

This section explains how the longitudinal weight transfer, grade and bank change the longitudinal acceleration profiles a_x and correspondingly, the speed profile U_x described in Section 2.4 and the feedforward longitudinal force F_x^{FFW} in Section 4.1.

A.1 Effect of longitudinal weight transfer

When a point mass assumption is used to estimate the maximum acceleration a_x in Section 2.4, the effect of weight transfer is neglected and it is implied that all four tires reach their limits at once. This point mass assumption produces a friction limit circle on a “ $g-g$ ” diagram (see Fig. 2.1(b)) that can be used to calculate the acceleration and the speed profiles [43]. Thus, the combination of maximum longitudinal a_x and lateral a_y acceleration is dictated by a friction limit circle on a “ $g-g$ ” diagram with a radius given by the friction coefficient μ times by gravity g .

$$(\mu g)^2 = a_x^2 + a_y^2 , \quad (\text{A.1})$$

However, during braking or accelerating, there is longitudinal weight transfer, which influences the normal load of each axle. This difference in normal load causes

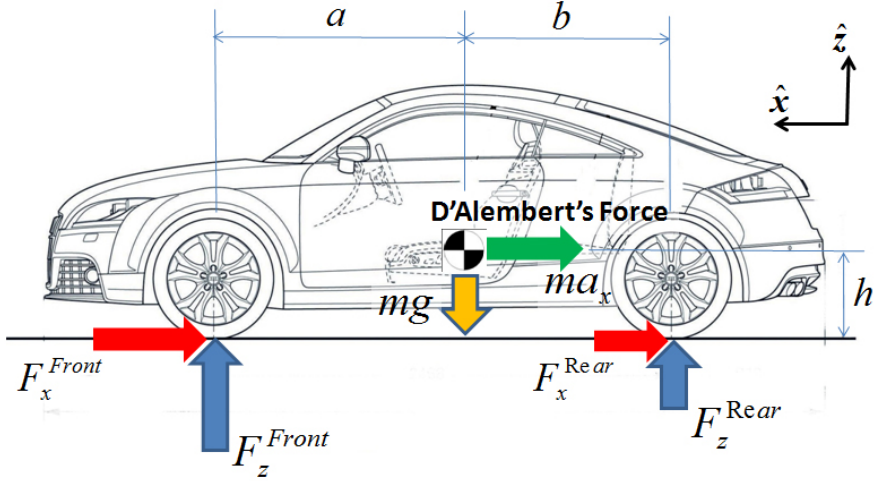


Figure A.1: Weight transfer during braking, \hat{x} and \hat{y} represent vehicle body-fixed coordinate (figure of Audi TTS, courtesy of www.audiusanews.com)

each axle to reach its limit at different times because the normal load dictates the amount of available friction force. For instance, during hard braking (see Fig. A.1), the front normal load F_{zf} increases while the rear normal load F_{zr} decreases. Thus, there is a tendency for the rear axle to slide before the front axle during braking because the rear axle has less cornering ability due to decreasing in the rear normal load. This breaks down the point mass assumption because the rear axle reaches its limits before the front axle. Rather than considering a single friction circle from a point mass model, the algorithm now considers the front and rear friction circles.

To understand how this longitudinal weight transfer changes the vehicle's cornering ability, a corner-entry phase where the controller trail-brakes is explained. In this case, the assumption that the rear axle dictates the cornering ability is made because of the decrease in rear normal load. First, the rear normal load F_{zr} during braking is determined from D'Alembert principal [54], which treats vehicle acceleration as a force in the opposite direction. From Fig. A.1,

$$\begin{aligned} F_{zr} &= \frac{a}{a+b}mg + \frac{h}{a+b}m\tilde{a}_x \\ F_{zr} &= \frac{1}{a+b}m(ag + h\tilde{a}_x) , \end{aligned} \quad (\text{A.2})$$

where h is the distance from vehicle center of gravity (CG) to the ground (see Fig. A.1 and Table B.1 for the value). Then the longitudinal acceleration on a flat surface \tilde{a}_x is calculated from the rear friction circle¹.

From F_{zr} in (A.2), the maximum force F_r that the rear axle can generate is equal to $F_r = \mu F_{zr}$. This F_r is the radius of the rear friction circle when an isotropic tire assumption is used. The goal of the feedforward longitudinal controller is to find the longitudinal acceleration \tilde{a}_x that produces the longitudinal rear axle force F_{xr} that once combined with the lateral rear axle force F_{yr} , places the tire on the edge of the rear friction circle.

$$(F_r)^2 = (F_{xr})^2 + (F_{yr})^2 \quad (\text{A.3})$$

The friction circle in (A.3) is rearranged to calculate the desired \tilde{a}_x . First, the value of F_{yr} is estimated, then the relationship between F_{xr} and a_x is determined. To find the rear axle force F_{yr} , this F_{yr} value has to balance with the front lateral axle force F_{yf} in order to prevent the vehicle from spinning [see (A.4)]. From Fig. 3.2, assuming that the rate of change in yaw rate ($\alpha \approx 0$) is small and using a small steering angle ($\delta \approx 0$) assumption, the rear lateral axle force F_{yr} that maintains yaw moment balance has to satisfy

$$\begin{aligned} \Sigma M_z &= I\alpha = 0 \\ F_{yf}a - F_{yr}b &= 0 . \end{aligned} \quad (\text{A.4})$$

When (A.4) is combined with Newton's second law in the lateral direction $\Sigma F_y = F_{yf} + F_{yr} = ma_y$, where F_y is the total lateral force, the rear lateral force F_{yr} that maintains the moment balance is equal to

$$F_{yr} = \frac{a}{a+b}ma_y = m_r a_y , \quad (\text{A.5})$$

where $m_r = \frac{a}{a+b}$ is an equivalent mass at the rear axle. The longitudinal rear axle force F_{xr} can be found from substituting F_{zr} in (A.2) and F_{yr} in (A.5) into the rear

¹This \tilde{a}_x value does not take the effect of grade into account and is the acceleration that is caused purely by the tire forces.

friction circle (A.3), and rearranging the equation to obtain

$$\left(\frac{\mu}{a+b}m(ag + h\tilde{a}_x)\right)^2 = (F_{xr})^2 + (m_r a_y)^2. \quad (\text{A.6})$$

The next step to solve for the longitudinal acceleration \tilde{a}_x is to find the relationship between \tilde{a}_x and F_{xr} . In an ideal case when there is no weight transfer, the braking force is split between the front and rear axle according to the static normal load, i.e. $F_{xr} = m_r a_x$. However, due to the weight transfer, a brake system in a vehicle has a proportioning valve that adjusts the brake bias (distribution) to prevent the rear axle from locking up. This brake proportioning value \tilde{f} is defined by

$$\tilde{f} = \frac{F_{xr}}{m_r \tilde{a}_x}. \quad (\text{A.7})$$

If there is no weight transfer, then $\tilde{f} = 1$; however, with the weight transfer, different value of \tilde{f} is used. For simplicity, a constant \tilde{f} is used² and the value of \tilde{f} will be discussed in the following section. With a constant \tilde{f} , the \tilde{a}_x can be found from (A.6) with $F_{xr} = \tilde{f} m_r \tilde{a}_x$

$$\left(\frac{\mu}{a+b}m(ag + h\tilde{a}_x)\right)^2 = (\tilde{f} m_r \tilde{a}_x)^2 + (m_r a_y)^2, \quad (\text{A.8})$$

which can be rearranged to

$$\begin{aligned} \left(\frac{\mu}{a+b}m(ag + h\tilde{a}_x)\right)^2 &= (\tilde{f} m_r \tilde{a}_x)^2 + (m_r a_y)^2 \\ (\mu(ag + h\tilde{a}_x))^2 &= (a\tilde{f}\tilde{a}_x)^2 + (aa_y)^2 \\ (a^2\tilde{f}^2 - \mu^2h^2)\tilde{a}_x^2 - 2\mu^2agh\tilde{a}_x + (a^2a_y^2 - \mu^2a^2g^2) &= 0. \end{aligned} \quad (\text{A.9})$$

Solving for \tilde{a}_x in (A.9) produces two possible solutions. However, in the braking case where weight is transferred to the front, \tilde{a}_x must be negative and only one solution exists from (A.9), which is

²Although it is possible to employ \tilde{f} that is directly proportional to the rear normal load, this produces a complex quadratic function that is difficult to solve.

$$\tilde{a}_x = \frac{2\mu^2 agh - \sqrt{(2\mu^2 agh)^2 - 4(a^2 \tilde{f}^2 - \mu^2 h^2)(a^2 a_y^2 - \mu^2 a^2 g^2)}}{2(a^2 \tilde{f}^2 - \mu^2 h^2)} . \quad (\text{A.10})$$

By using a numerical integration method as described in Section 2.4, the desired speed and longitudinal acceleration profiles along the segment are found.

A.1.1 Brake proportioning (\tilde{f})

As mentioned in the previous Section, the brake distribution between front and rear axle has to be adjusted to accommodate changes in the normal load. In production vehicles, manufacturers use brake proportioning valves to accommodate this change [17]. There are multiple production mechanical and electrical proportioning systems, where the Audi TTS uses the latter system. Unfortunately, the brake distribution \tilde{f} for the Audi TTS is unknown and some assumptions have to be made to estimate this constant \tilde{f} .

Before making any assumptions about \tilde{f} , (A.8) is rearranged to understand the function of \tilde{f} .

$$\tilde{f} = \frac{1}{|m_r \tilde{a}_x|} \sqrt{\left(\frac{\mu}{a+b} m(ag + h\tilde{a}_x)\right)^2 - (m_r a_y)^2} . \quad (\text{A.11})$$

Theoretically, if all the parameters, including μ , \tilde{a}_x and a_y are known, an ideal \tilde{f} that will ensure that the rear axle is braking at the limits at all time can be found. Nevertheless, to simplify the calculation of \tilde{a}_x in (A.10), a constant \tilde{f} that ensures continuous vehicle's deceleration on a "g-g" diagram is used. That is, at the corner entry (point A in Fig. 2.1(b)), both front and rear axles should produce maximum braking ($\tilde{a}_x = -\mu g$). Thus, at point A in Fig. 2.1(b), assuming that \tilde{f} is positive, substituting $\tilde{a}_x = -\mu g$ into (A.11) produces

$$\begin{aligned} \tilde{f} &= \frac{1}{|-m_r \mu g|} \sqrt{\left(\frac{\mu}{a+b} m(ag - h\mu g)\right)^2} \\ \tilde{f} &= \frac{1}{a}(a - h\mu) . \end{aligned} \quad (\text{A.12})$$

Consequently, \tilde{f} in (A.12) is used for finding the desired longitudinal acceleration \tilde{a}_x in (A.8).

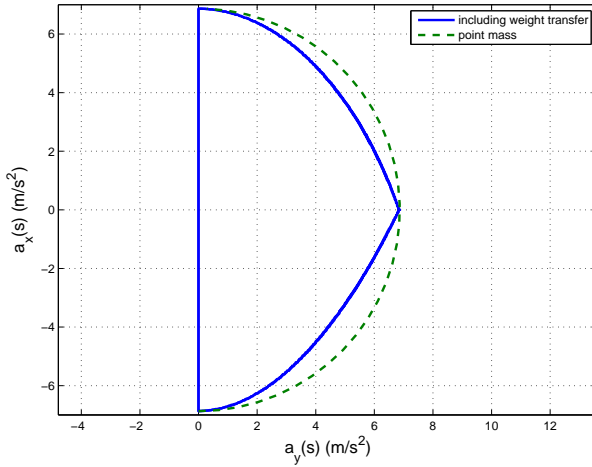


Figure A.2: Effect of longitudinal weight transfer on maximum acceleration, using $\mu = 0.7$ and vehicle parameters from Table B.1, assuming no acceleration limitation from engine torque

After including the effect of longitudinal weight transfer, the vehicle's friction limit on a “*g-g*” diagram is no longer a circle and is shown in Fig. A.2 (re-plot of Fig. 2.6).

A.2 Effect of grade

Besides the longitudinal weight transfer, bank and grade also affect the maximum acceleration of the vehicle. Before explaining these effects in detail, the coordinate system used in this analysis is explained (Figs. A.3 and A.5). A vehicle body-fixed frame is used for the analysis, where a bank angle θ_{bank} and a grade angle θ_{grade} are measured relative to the earth frame. That is, the θ_{bank} and θ_{grade} are measured from the angle between the z-axis of the earth frame that points outward from the center of the earth and the z-axis of the vehicle frame that points outward from the top of the inertial measurement unit (IMU). In addition, the calculation uses a quasi-static assumption and assumes that the effects of bank and grade are decoupled and can be superimposed³.

³The bank and grade angles depend on the topography of the track and the vehicle heading. For instance, on a 45 degree inclined surface, the vehicle could have zero bank with 45 degree grade or

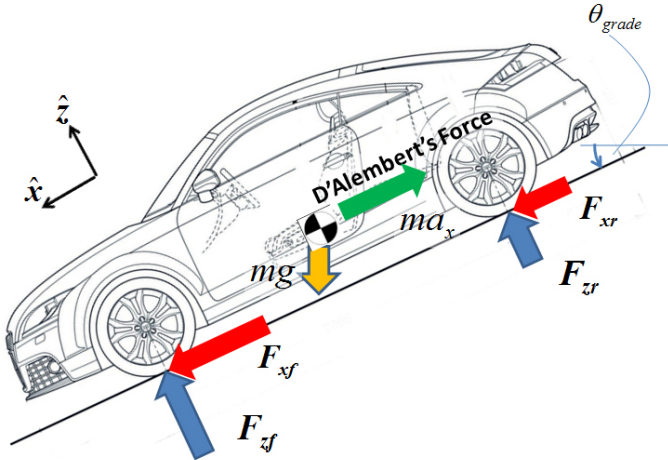


Figure A.3: Effect of grade (figure of Audi TTS, courtesy of www.audiusanews.com)

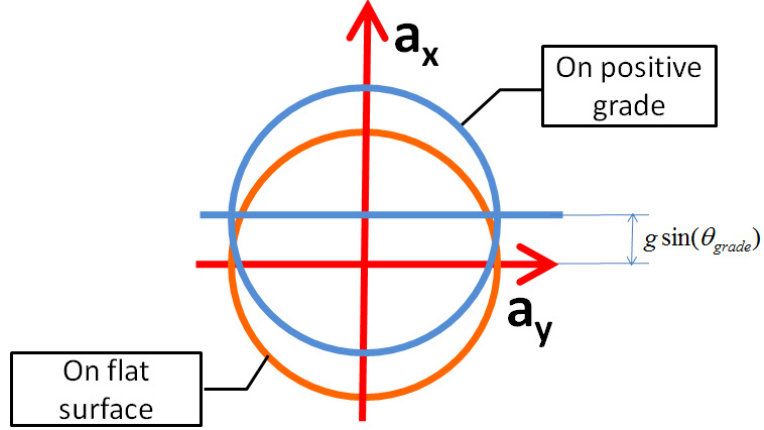
Figure A.3 demonstrates the effect of grade on the vehicle. If the grade is positive, the vehicle is traveling down the hill. The additional force from the vehicle's weight ($mg \sin \theta_{grade}$) accelerates the vehicle and reduces the rear normal load as will be explained in the following sections.

A.2.1 Shifting “g-g” diagram

The additional acceleration due to the grade shifts the acceleration limits on a “g-g” diagram. If the tires generate zero forces, the vehicle would still accelerate due to gravity (when grade is positive); thus, creating an offset on the “g-g” diagram as shown in Fig. A.4.

To quantify the amount of offset on a “g-g” diagram in Fig. A.4, a point mass assumption is used. From Fig. A.3, the longitudinal acceleration a_x can be found

vice versa, depends on the heading of the vehicle. However, in this analysis, the same bank and grade angles are utilized regardless of the vehicle heading.

Figure A.4: Effect of grade on a “ $g-g$ ” diagram

from

$$\begin{aligned} F_{xf} + F_{xr} + mg \sin \theta_{grade} &= ma_x \\ a_x &= \frac{F_x}{m} + g \sin \theta_{grade}, \end{aligned} \tag{A.13}$$

where F_x , F_{xf} and F_{xr} are total, front and rear longitudinal forces respectively.

Thus, there is an additional acceleration ($g \sin \theta_{grade}$) due to the grade that acts on the body of the vehicle in addition to the tire forces. Therefore, the longitudinal acceleration a_x that a vehicle could achieve is modified from (A.10) to

$$a_x = \frac{2\mu^2 agh - \sqrt{(2\mu^2 agh)^2 - 4(a^2 \tilde{f}^2 - \mu^2 h^2)(a^2 a_y^2 - \mu^2 a^2 g^2)}}{2(a^2 \tilde{f}^2 - \mu^2 h^2)} + g \sin \theta_{grade}. \tag{A.14}$$

Since the $g \sin \theta_{grade}$ term comes from the gravity acting on the vehicle body, and not from the tire forces, the feedforward longitudinal force required from the tires in Section 4.1 does not include this grade effect. This $g \sin \theta_{grade}$ term is canceled out by the drag compensation in Section 4.1.2.

A.2.2 Reduction in normal load

Besides creating an offset due to gravity, grade also changes the axles' normal loads, (see Fig. A.3). For a positive grade, the higher the grade, the higher the front normal load and the lower the rear normal load. By using a moment balance around the vehicle's y-axis at front and rear contact patches, and neglecting the pitch dynamics, the normal load of each axle can be found from

$$\begin{aligned} F_{zr}(a+b) &= mg \cos \theta_{grade} a - mg \sin \theta_{grade} h + ma_x h \\ F_{zf}(a+b) &= mg \cos \theta_{grade} b + mg \sin \theta_{grade} h - ma_x h . \end{aligned} \quad (\text{A.15})$$

Thus, the maximum forces that the rear axle could generate changes from $F_r = \mu m_r g$ to

$$\begin{aligned} F_r &= \mu(mg \cos \theta_{grade} \frac{a}{a+b} - mg \sin \theta_{grade} \frac{h}{a+b} + ma_x \frac{h}{a+b}) \\ F_r &= \mu(m_r g \cos \theta_{grade} - \frac{m_r h}{a} g \sin \theta_{grade} + m_r a_x \frac{h}{a}) . \end{aligned} \quad (\text{A.16})$$

The effect of grade on the normal load will be used in Section A.4, where additional longitudinal weight transfer and the effect of bank are included.

A.3 Effect of bank

In contrast to grade, the vehicle normal load changes according to the vehicle's lateral force when a vehicle is cornering on a banked road (see Fig. A.5). Furthermore, some amount of lateral force from the tires are required to prevent the vehicle from sliding laterally on a bank. These effects are taken into consideration and the effect of bank on the required lateral forces is discussed first.

A.3.1 Effect of bank on lateral forces

This section describes the amount of forces required to prevent the vehicle from sliding on a bank. A vehicle frame along the y-axis is used, where a_y shown in Fig. A.5 is approximated by a steady-state assumption $a_y \approx U_x^2/R$. Thus, the lateral force from

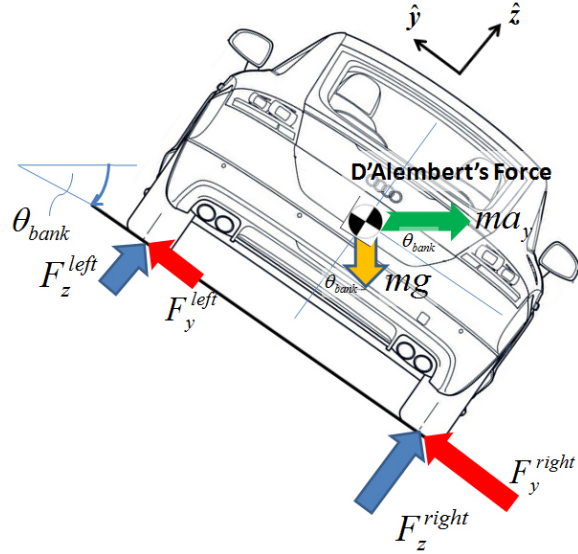


Figure A.5: Effect of bank, vehicle is turning left (figure of Audi TTS, courtesy of www.audiusanews.com)

the tires F_y that prevents the vehicle from sliding is derived from the zero sum of all forces along the vehicle's y-axis.

$$\begin{aligned} F_y - mg \sin \theta_{bank} - ma_y \cos \theta_{bank} &= 0 \\ F_y &= mg \sin \theta_{bank} + ma_y \cos \theta_{bank} \end{aligned} \quad (\text{A.17})$$

If an assumption that the front and rear lateral forces are distributed according to the weight distribution $F_{yr} = m_r a_y$ (i.e. the vehicle is turning with a small α) is used, then

$$F_{yr} = m_r g \sin \theta_{bank} + m_r a_y \cos \theta_{bank} . \quad (\text{A.18})$$

Thus, this effect from the bank will be incorporated in the rear friction circle in (A.3), when calculating a_x in the following section.

A.3.2 Effect of bank on normal load

From Fig. A.5, the cornering ability changes according to the bank angle θ_{bank} . In this case, the vehicle is turning left and the bank is positive. From the direction of D'Alembert's force, the vehicle's cornering ability reduces due to a decrease in the normal load. Since the sum of all forces along the \hat{z} -axis of the vehicle frame is equal to zero, the total normal load F_z decreases as follows

$$\begin{aligned} F_{zr} &= m_r g \cos \theta_{bank} - m_r a_y \sin \theta_{bank} \\ F_{zr} &= m_r (g \cos \theta_{bank} - a_y \sin \theta_{bank}) \end{aligned} \quad (\text{A.19})$$

Note that from (A.19), the rear axle normal load F_{zr} also depends on the lateral acceleration a_y .

If the effects of weight transfer in (A.2), grade in (A.15) and bank in (A.19) on the rear normal load F_{zr} are superimposed, the maximum rear friction force can be found from $F_r = \mu F_{zr}$.

$$\begin{aligned} F_r &= \mu (m_r g \cos \theta_{grade} \cos \theta_{bank} + m \tilde{a}_x \frac{h}{a+b} - m g \sin \theta_{grade} \frac{h}{a+b} - m_r a_y \sin \theta_{bank}) \\ F_r &= \mu (m_r g \cos \theta_{grade} \cos \theta_{bank} + m_r \tilde{a}_x \frac{h}{a} - m_r g \sin \theta_{grade} \frac{h}{a} - m_r a_y \sin \theta_{bank}) \\ F_r &= \mu' m_r g , \end{aligned} \quad (\text{A.20})$$

where $\mu' = (\cos \theta_{grade} \cos \theta_{bank} + \frac{\tilde{a}_x h}{g a} - \sin \theta_{grade} \frac{h}{a} - \frac{a_y}{g} \sin \theta_{bank}) \mu$.

Thus, the equation of the rear friction circle in (A.3) when including the effect of bank (A.17, A.19) and grade (A.20) becomes

$$\begin{aligned} (F_r)^2 &= (F_{xr})^2 + (F_{yr})^2 \\ (\mu' m_r g)^2 &= (\tilde{f} m_r \tilde{a}_x)^2 + (m_r g \sin \theta_{bank} + m_r a_y \cos \theta_{bank})^2 \\ (\mu' g)^2 &= (\tilde{f} \tilde{a}_x)^2 + (g \sin \theta_{bank} + a_y \cos \theta_{bank})^2 . \end{aligned} \quad (\text{A.21})$$

This equation will be used to find longitudinal acceleration a_x in the following section.

A.4 Calculating desired longitudinal acceleration for each section

After incorporating the effects of longitudinal weight transfer, bank and grade into account, this section explains how the desired acceleration a_x of each segment is calculated.

A.4.1 Calculating a_x for straight section

Finding the longitudinal acceleration a_x on a straight segment is straightforward as there is no lateral tire force required from turning. The only lateral force required from the tires are used for preventing the vehicle from sliding laterally on a banked road (see Section A.3.1). Furthermore, when lateral forces are not present, all four tires can reach their limit at once because there is no requirement for the front and rear lateral forces to balance each other out to prevent the vehicle from spinning (see Section A.1). Thus, assuming that the brake proportioning \tilde{f} ensures that both front and rear axles are braking at their friction limits, a point mass assumption on bank and grade can be used. This is possible because the effect of weight transfer cancels each other out. For instance, the decrease in rear axle normal load is equal to the increase in front axle normal load and vice versa. Consequently, the total sum of this effect on the normal loads is equal to zero.

Thus, assuming that all tires reach their limits at once, the longitudinal acceleration a_x can be derived from the friction circle that incorporates all the effects of bank and grade into the normal load.

$$\begin{aligned} F^2 &= F_x^2 + F_y^2 \\ ((\cos \theta_{grade} \cos \theta_{bank}) \mu mg)^2 &= (ma_x - mg \sin \theta_{grade})^2 + (mg \sin \theta_{bank})^2 \quad (\text{A.22}) \\ a_x &= -\sqrt{(\cos \theta_{grade} \cos \theta_{bank} \mu g)^2 - (g \sin \theta_{bank})^2} + g \sin \theta_{grade}, \end{aligned}$$

where F is the maximum tire forces from all four wheels (radius of the friction circle).

A.4.2 Calculating a_x for corner entry section

In contrast to a straight segment, the balance between the front and rear lateral force is required to prevent the vehicle from spinning in a corner-entry segment. Thus, during trail-braking, the rear axle could reach its limits before the front axle due to longitudinal weight transfer. Starting from the friction circle of the rear axle in (A.21), where all the effects of longitudinal weight transfer, bank and grade are taken into account, a new brake proportioning \tilde{f} has to be calculated to satisfy the continuity requirement at the beginning of a clothoid-entry segment (similar to Section A.1.1). That is when $a_y = 0$, a_x^{limit} has to equal \tilde{a}_x [which is a_x in (A.22) without the $g \sin \theta_{grade}$ term].

$$\begin{aligned} (\mu' g)^2 &= (\tilde{f} \tilde{a}_x)^2 + (g \sin \theta_{bank} + a_y \cos \theta_{bank})^2 \\ ((\cos \theta_{grade} \cos \theta_{bank} + \frac{\tilde{a}_x}{g} \frac{h}{a} - \sin \theta_{grade} \frac{h}{a}) \mu g)^2 &= (\tilde{f} a_x^{limit})^2 + (g \sin \theta_{bank})^2 \end{aligned} \quad (\text{A.23})$$

After rearranging (A.23), a positive constant \tilde{f} that will create a smooth transition when $\tilde{a}_x = a_x^{limit}$) can be found from

$$\tilde{f} = \frac{1}{|a_x^{limit}|} \sqrt{((\cos \theta_{grade} \cos \theta_{bank} + \frac{a_x^{limit}}{g} \frac{h}{a} - \sin \theta_{grade} \frac{h}{a}) \mu g)^2 - (g \sin \theta_{bank})^2}. \quad (\text{A.24})$$

After \tilde{f} is found, the longitudinal acceleration a_x in (A.21) when lateral acceleration a_y is present can be calculated from a second-order polynomial equation.

$$\begin{aligned} ((\cos \theta_{grade} \cos \theta_{bank} + \frac{\tilde{a}_x}{g} \frac{h}{a} - \sin \theta_{grade} \frac{h}{a} - \frac{a_y}{g} \sin \theta_{bank}) \mu m_r g)^2 &\\ = (\tilde{f} m_r \tilde{a}_x)^2 + (m_r g \sin \theta_{bank} + m_r a_y \cos \theta_{bank})^2 & \end{aligned} \quad (\text{A.25})$$

To simplify the calculation process, new constants are introduced to solve (A.25).

$$(A + Ba_x)^2 = (\tilde{f}a_x)^2 + C^2 ,$$

where

$$\begin{aligned} A &= (\cos \theta_{grade} \cos \theta_{bank} - \sin \theta_{grade} \frac{h}{a} - \frac{a_y}{g} \sin \theta_{bank}) \mu g \\ B &= \frac{h}{a} \mu \\ C &= g \sin \theta_{bank} + a_y \cos \theta_{bank} \end{aligned} \quad (A.26)$$

Rearrange a_x into a second order polynomial function:

$$(\tilde{f}^2 - B^2)a_x^2 - 2ABa_x + (C^2 - A^2) = 0 ,$$

where the negative solution of a_x (braking) when $B > 0$ is equal to

$$\begin{aligned} a_x &= \frac{2AB - \sqrt{(2AB)^2 - 4(\tilde{f}^2 - B^2)(C^2 - A^2)}}{2(\tilde{f}^2 - B^2)} , \quad A \geq 0 \\ a_x &= \frac{-2AB - \sqrt{(2AB)^2 - 4(\tilde{f}^2 - B^2)(C^2 - A^2)}}{-2(\tilde{f}^2 - B^2)} , \quad A < 0 \end{aligned} \quad (A.27)$$

Thus, the longitudinal acceleration a_x is found and the method in Section 2.4 can be used to find the desired speed profile.

A.4.3 Calculating a_x for constant radius section

In a constant radius segment, the vehicle is traveling at a constant speed while cornering at the limits. Thus, the desired longitudinal acceleration when grade is not present is equal to $\tilde{a}_x = 0$. Nevertheless, the desired speed U_x is needed for the vehicle to track and could be estimated from the maximum lateral acceleration a_y , $U_x = \sqrt{a_y R}$. On a flat surface, the front and rear axle will reach their limits at once. However, the effect of grade could change the normal loads of the front and rear axle, causing the front and rear axle to reach their limits at different times. Thus, the algorithm has to individually calculate which axle will reach its limits first and at what a_y . From (A.21), with $\tilde{a}_x = 0$, the maximum lateral acceleration when the front axle a_{yf} and rear axle a_{yr} are sliding are calculated and compared.

$$\begin{aligned}
(\mu'g)^2 &= (\tilde{f}\tilde{a}_x)^2 + (g \sin \theta_{bank} + a_y \cos \theta_{bank})^2 \\
((\cos \theta_{grade} \cos \theta_{bank} - \frac{h}{a} \sin \theta_{grade} - \frac{a_{yr}}{g} \sin \theta_{bank})\mu g)^2 &= (g \sin \theta_{bank} + a_{yr} \cos \theta_{bank})^2 \\
((\cos \theta_{grade} \cos \theta_{bank} + \frac{h}{b} \sin \theta_{grade} - \frac{a_{yf}}{g} \sin \theta_{bank})\mu g)^2 &= (g \sin \theta_{bank} + a_{yf} \cos \theta_{bank})^2
\end{aligned} \tag{A.28}$$

The maximum lateral acceleration a_y is chosen according to the direction of the cornering. When cornering left, a_y is positive; thus, the lower lateral acceleration is chosen.

$$\begin{aligned}
a_{yr} &= \frac{\cos \theta_{grade} \cos \theta_{bank} \mu g - \frac{h}{a} \sin \theta_{grade} \mu g - g \sin \theta_{bank}}{\cos \theta_{bank} + \mu \sin \theta_{bank}} \\
a_{yf} &= \frac{\cos \theta_{grade} \cos \theta_{bank} \mu g + \frac{h}{b} \sin \theta_{grade} \mu g - g \sin \theta_{bank}}{\cos \theta_{bank} + \mu \sin \theta_{bank}} \\
a_y &= \min(a_{yf}, a_{yr})
\end{aligned} \tag{A.29}$$

when cornering right, a_y is negative; thus, the higher lateral acceleration is chosen.

$$\begin{aligned}
a_{yr} &= \frac{-\cos \theta_{grade} \cos \theta_{bank} \mu g + \frac{h}{a} \sin \theta_{grade} \mu g - g \sin \theta_{bank}}{\cos \theta_{bank} - \mu \sin \theta_{bank}} \\
a_{yf} &= \frac{-\cos \theta_{grade} \cos \theta_{bank} \mu g - \frac{h}{b} \sin \theta_{grade} \mu g - g \sin \theta_{bank}}{\cos \theta_{bank} - \mu \sin \theta_{bank}} \\
a_y &= \max(a_{yf}, a_{yr})
\end{aligned} \tag{A.30}$$

After a_y is found, the vehicle speed along the constant radius segment is calculated from $U_x = \sqrt{a_y R}$.

A special case arises in this segment if the entry-speed of the following clothoid-exit is lower than the speed of the constant radius segment. In this case, the vehicle has to brake in a constant radius segment and the amount of deceleration a_x is found using the method in Section A.4.2, but with a constant curvature value.

A.4.4 Calculating a_x for clothoid-exit section

Similar to a clothoid-entry phase where the rear normal load reduces, the controller applies throttle during a corner-exit, which reduces the front normal load. Thus, the maximum acceleration a_x that includes the effects of longitudinal weight transfer, bank and grade into account is dictated by the friction limitation of the front axle.

Using the same approach as (A.20) to find the front normal load F_{zf} produces

$$\begin{aligned}
F_{zf} &= \mu' m_f g \\
&\text{where} \\
\mu' &= (\cos \theta_{grade} \cos \theta_{bank} - \frac{\tilde{a}_x}{g} \frac{h}{b} + \sin \theta_{grade} \frac{h}{b} - \frac{a_y}{g} \sin \theta_{bank}) \mu.
\end{aligned} \tag{A.31}$$

Thus, the friction circle of the front axle becomes

$$\begin{aligned}
F_f^2 &= F_{xf}^2 + F_{yf}^2 \\
(\mu' m_f g)^2 &= (\tilde{t} m_f \tilde{a}_x)^2 + (m_f g \sin \theta_{bank} + m_f a_y \cos \theta_{bank})^2 \\
(\mu' g)^2 &= (\tilde{t} \tilde{a}_x)^2 + (g \sin \theta_{bank} + a_y \cos \theta_{bank})^2,
\end{aligned} \tag{A.32}$$

where \tilde{t} is the drive-torque proportioning to the front axle. Similar to the brake proportioning value \tilde{f} , the drive torque value has to ensure continuity in the longitudinal acceleration when the curve transitions from a corner exit to a straight. That is, the longitudinal acceleration when grade is not present \tilde{a}_x is equal to a_x^{limit} when $a_y = 0$, assuming that the engine has unlimited torque. Thus, a constant \tilde{t} can be found from rearranging (A.32).

$$\begin{aligned}
((\cos \theta_{grade} \cos \theta_{bank} - \frac{a_x^{limit}}{g} \frac{h}{b} + \sin \theta_{grade} \frac{h}{b}) \mu g)^2 &= (\tilde{t} a_x^{limit})^2 + (g \sin \theta_{bank})^2 \\
\tilde{t} &= \frac{1}{a_x^{limit}} \sqrt{((\cos \theta_{grade} \cos \theta_{bank} - \frac{a_x^{limit}}{g} \frac{h}{b} + \sin \theta_{grade} \frac{h}{b}) \mu g)^2 - (g \sin \theta_{bank})^2}
\end{aligned} \tag{A.33}$$

Substituting \tilde{t} in (A.33) into (A.32) to solve for a_x .

$$\begin{aligned}
((\cos \theta_{grade} \cos \theta_{bank} - \frac{\tilde{a}_x}{g} \frac{h}{b} + \sin \theta_{grade} \frac{h}{b} - \frac{a_y}{g} \sin \theta_{bank}) \mu g)^2 &= (\tilde{t} \tilde{a}_x)^2 + (g \sin \theta_{bank} + a_y \cos \theta_{bank})^2 \\
(A - B a_x)^2 &= (\tilde{t} \tilde{a}_x)^2 + C^2,
\end{aligned} \tag{A.34}$$

where constant $A = (\cos \theta_{grade} \cos \theta_{bank} + \sin \theta_{grade} \frac{h}{b} - \frac{a_y}{g} \sin \theta_{bank}) \mu g$, $B = \frac{h}{b} \mu$, and $C = g \sin \theta_{bank} + a_y \cos \theta_{bank}$. Rearranging (A.34) into a polynomial form to solve for a_x produces

$$(\tilde{t}^2 - B^2)a_x^2 + 2ABa_x + (C^2 - A^2) = 0 . \quad (\text{A.35})$$

Because a_x is positive during accelerating and $B = \frac{h}{b}\mu > 0$, the longitudinal acceleration a_x is found.

$$\begin{aligned} a_x &= \frac{-2AB + \sqrt{(2AB)^2 - 4(\tilde{t}^2 - B^2)(C^2 - A^2)}}{2(\tilde{t}^2 - B^2)} , \quad A \geq 0 \\ a_x &= \frac{2AB + \sqrt{(2AB)^2 - 4(\tilde{t}^2 - B^2)(C^2 - A^2)}}{-2(\tilde{t}^2 - B^2)} , \quad A < 0 \end{aligned} \quad (\text{A.36})$$

Similar to the constant radius phase in Section A.4.3, there is a special case when the vehicle has to brake in a clothoid-exit phase to achieve the desired entry-speed of the next segment. By using the similar approach mentioned in Section A.4.2 with a clothoid exit curvature, the desired a_x can be found.

The calculated longitudinal acceleration a_x and the desired speed U_x are then used in Chapter 4 to calculate the longitudinal inputs.

Appendix B

Autonomous Audi TTS (Shelley)

A 2009 Audi TTS was modified to receive the driving commands from the controller. The vehicle's parameters can be found from Tab. B.1. A Passat CC power steering system is used for the steering by-wire system, while a production brake booster from a vehicle with an adaptive cruise control is utilized for the brake by-wire system. The throttle system already has a by-wire interface from a production vehicle. All of the communications between the controller and the actuators use CAN (Controller Area Network) interface.

Table B.1: Shelley's parameters

mass	m	1,648	kg
distance from CG to front axle	a	1.04	m
distance from CG to rear axle	b	1.42	m
distance from CG to ground	h	0.75	m
yaw moment of inertia about CG ^a	I_{zz}	2,452	kg.m ²
track width		1.55	m
effective wheel radius	R_e	0.33	m

^aApproximated from $I_{zz} \approx mab$.

B.1 Steering system

The electronic power steering in the Audi TTS is configured to receive a torque command T , rather than the steering angle command δ . Thus, a low-level steering controller is designed to calculate the torque required from the desired steering angle δ in (6.19). The low-level steering controller consists of a feedforward module that estimates the required steering torque, while a lead controller is used in the steering feedback module.

B.1.1 Steering system dynamics

Before designing a low-level steering controller, the steering system dynamics are explained. When a steering torque T is applied to the steering system, in addition to rotating the steering system, it has to overcome coulomb friction in the steering system $T_{friction}$, viscous torque $T_{viscous}$, the jacking torque $T_{jacking}$, and the aligning moment T_{align} . Thus, in order to design a feedforward controller for the low-level steering system, the steering system parameters and these resisting torques in (B.1) have to be identified.

$$I_{st}\dot{\omega}_{st} = T - T_{friction} - T_{viscous} - T_{jacking} - T_{align} , \quad (\text{B.1})$$

where I_{st} is the inertia and ω_{st} is the angular speed of the steering system respectively. The following sections explain how different system identification techniques are used to identify the parameters in (B.1).

Steering friction and jacking torque

The friction force in the steering system $T_{friction}$ comes from coulomb friction while the jacking torque $T_{jacking}$ comes from the restoring torque that jacks the vehicle up when turning, which creates an on-center steering feel. To identify $T_{friction}$ and $T_{jacking}$ for the feedforward low-level steering controller, the Audi TTS was put on radius plates and a slow saw-tooth steering input was used. Figure B.1 plots the results of the steering torque required to turn the steering system on radius plates at

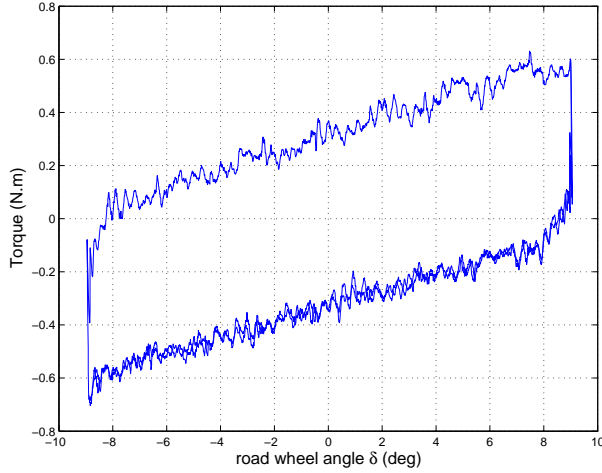


Figure B.1: Identifying jacking torque in the steering system

a slow speed, which minimizes the dynamic effects of the steering system ($\dot{\omega}_{st} \approx 0$ and $T_{viscous} \approx 0$). Since the vehicle is on the radius plates, there is no restoring force from the tires $T_{align} \approx 0$. Thus, the only torque presents in Fig. B.1 is the combination of $T_{friction}$ ¹ and $T_{jacking}$.

The Coulomb friction in the steering system $T_{friction}$ is assumed to be constant and only depends on the direction of the rotation $T_{friction} = -\text{sgn}(\dot{\omega}_{st})F_{st}$, where F_{st} is the magnitude of the coulomb friction. Consequently, the thickness of the hysteresis loop in Fig. B.1 is equal to $2F_{st}$ and $F_{st} \approx 0.3 \text{ Nm}$. The slope $k_{jacking} \approx 1/30 \text{ Nm/deg}$ in Fig. B.1 indicates the additional steering torque required for additional road wheel angle $T_{jacking} = k_{jacking}\delta$.

Aligning moment

The restoring force from the tires generates an aligning moment T_{align} , which tends to return the steering wheel to the center. The difference between the jacking torque and the aligning moment is that the jacking torque comes from the suspension geometry and the value does not depend on the dynamic (cornering) force, while the aligning

¹ $T_{friction}$ in this setup will measure the combination of friction from the steering system and the radius plates, but it is assumed that the friction from the radius plates is negligible.

moment comes from tire forces and the value is constantly changing according to the tire forces and pneumatic trails. Rather than using system identification techniques to identify the aligning moment, an approximation approach described in the following section is used to compensate for T_{align} in the feedforward steering calculation.

B.1.2 Low-level feedforward steering controller

The low-level feedforward steering controller predicts the steering torque required to turn the steering system to the desired angle and compensates for the resisting torques in the system. From (B.1), the feedforward steering controller provides torque:

$$T_{FW} = I_{st}\dot{\omega}_{st} + T_{friction} + T_{viscous} + T_{jacking} + T_{align} \quad (\text{B.2})$$

in order to track the desired steering angle. However, in practice, the first three terms $I_{st}\dot{\omega}_{st} + T_{friction} + T_{viscous}$ are not used because of the following reasons. Compensating for $I_{st}\dot{\omega}_{st}$ and $T_{viscous}$ terms involve differentiating the desired steering angle δ , which can introduce high frequency noise. Similarly, the friction compensation $T_{friction} = -\text{sgn}(\dot{\omega}_{st})F_{st}$ injects high frequency torque into the steering system every time the system changes its direction. Consequently, to avoid injecting high frequency torque into the system, these first three terms are not incorporated into the low-level feedforward steering controller.

The jacking torque is compensated in the low-level feedforward steering controller, and the value is calculated by using the slope $k_{jacking}$ derived from Fig. B.1 in Section B.1.1.

$$T_{jacking} = k_{jacking}\delta \quad (\text{B.3})$$

The last term of the low-level feedforward steering controller is the aligning moment T_{align} . The aligning moment is the product of front lateral tire force F_{yf} times its pneumatic trail [60], where both values constantly change through the tire's non-linearity. To simplify the feedforward of the aligning moment, the algorithm uses

$$T_{align} = k_{align}F_{yf}, \quad (\text{B.4})$$

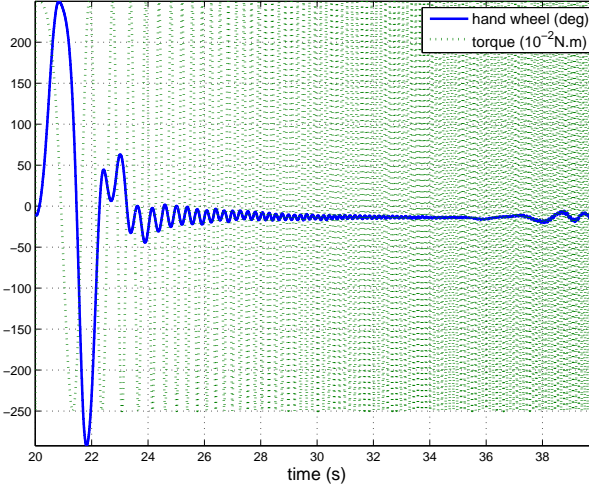


Figure B.2: Time history of the steering torque input and the hand wheel output, using a chirp input

where F_{yf} is the required front lateral forces calculated in Chapter 6 and k_{align} is a constant value chosen to simplify the representation of the pneumatic trail. This k_{align} is hand-tuned in the field by using a ramp-steer maneuver, and the tracking performance of the steering controller is observed to see if there is any over compensation from T_{align} .

B.1.3 Frequency response of the steering system

A system identification based on frequency response is used for comparing the steering system to a mass-spring damper system. The parameters from the system identification are then used for designing a lead feedback compensator in Matlab SISO tool [33].

A chirp torque input that sweeps from 0.05 to 10 Hz is used for system identification to find the transfer function of the system, while the steering angle at the handwheel is measured as an output², see Fig. B.2.

The frequency contents of the input, output and the transfer function of the

²Note that in implementation, care must be taken to ensure that the low-level steering controller uses the correct angle, either at the handwheel or at the road wheel.

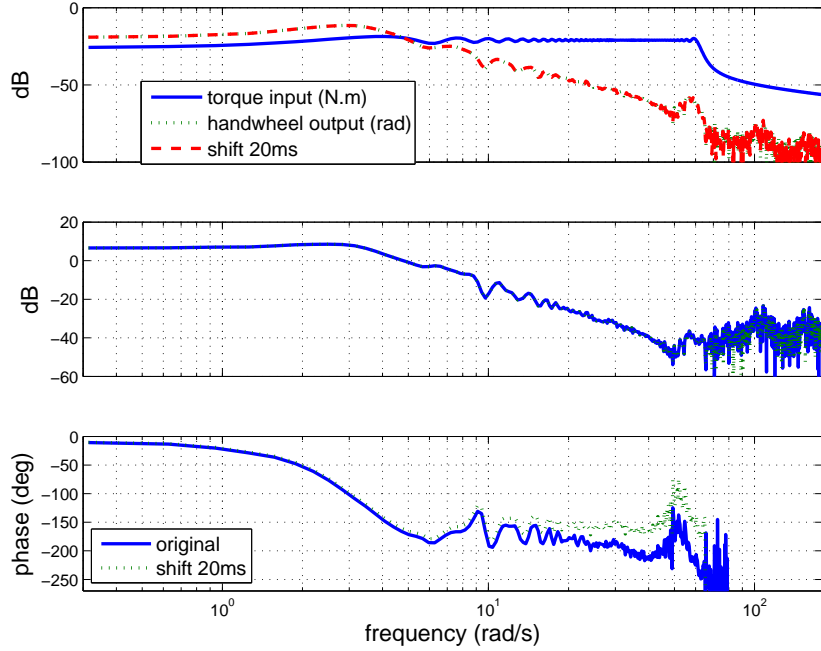


Figure B.3: Frequency response from the steering system identification, using chirp input. The handwheel output was shifted 20 ms forward to compensate for communication delay

steering system are shown in Fig. B.3. The transfer function of the steering system G_{st} is assumed to be a second-order mechanical system:

$$G_{st}(\mathfrak{s}) = \frac{\mathbb{K}*\omega_n^2}{\mathfrak{s}^2 + 2*\zeta*\omega_n*\mathfrak{s} + \omega_n^2} , \quad (\text{B.5})$$

where \mathfrak{s} is a Laplace variable, ω_n is the natural frequency, \mathbb{K} is an offset at zero frequency (DC offset) and ζ is the damping ratio of the system³. From comparing the transfer function in (B.5) with Fig. B.3, the peak resonance ω_n is approximately equal to 2.8 rad/s with a constant $\mathbb{K} = 2.1$ rad/N.m and $\zeta = 0.40$. These parameters from the transfer function are then used for designing the feedback compensator in Matlab SISO tool.

³The inertia of the system comes from I_{st} , the viscous damping comes from $T_{viscous}$ and the jacking torque provides stiffness to the system. Although these values are used for designing a feedback compensator, not for designing a feedforward controller.

From the phase of the transfer function in Fig. B.3, the system appears to have 20 ms of time delay because the phase roll off quickly at high frequency. After the output was shift by 20 ms, the phase plot flattens out at 180 degree, which is the expected behavior of a mass-spring-damper system. This 20 ms time delay came from the communication through CAN. In order to minimize this time delay, a new low-level steering controller is implemented in a micro-controller at the steering actuator, which reduces the time delay down to 10 ms.

B.1.4 Low-level feedback steering controller

The low-level feedback steering controller minimizes the tracking error due to modeling error and disturbances in the system. A simple lead compensator is used for the low-level feedback steering controller.

$$D(\mathfrak{s}) = K_{st} \frac{\mathfrak{s}+z}{\mathfrak{s}+p}, \quad (\text{B.6})$$

where K_{st} is the gain of the lead compensator, z is the zero location of the lead and p is the pole location of the lead. A Matlab SISO tool [33] was used to analyze the root locus and Bode plot of the system when a lead compensator was used with the steering system G_{st} in (B.5).

The lead compensator derived from SISO tool was then tested on the steering system, and the parameters were re-tuned to account for the 8 Nm torque limitation of the actuator and the 10 ms delay in the system. The value K_{st} was chosen to compromise between the tracking performance and the system's oscillation. Since there is a delay in the system, high K_{st} can cause the system to become unstable. The zero location z influences the damping response of the system: a low zero frequency increases damping frequency range but will slow the system response. The pole location p filters the high frequency noise out from the system. A higher pole frequency increases damping frequency range but allows the high frequency noise to pass through to the command signal. The final values of the lead compensator are $K_{st} = 8$, $z = 0.05$ and $p = 0.01$. The lead compensator was then converted into a digital domain for implementation in the micro controller.

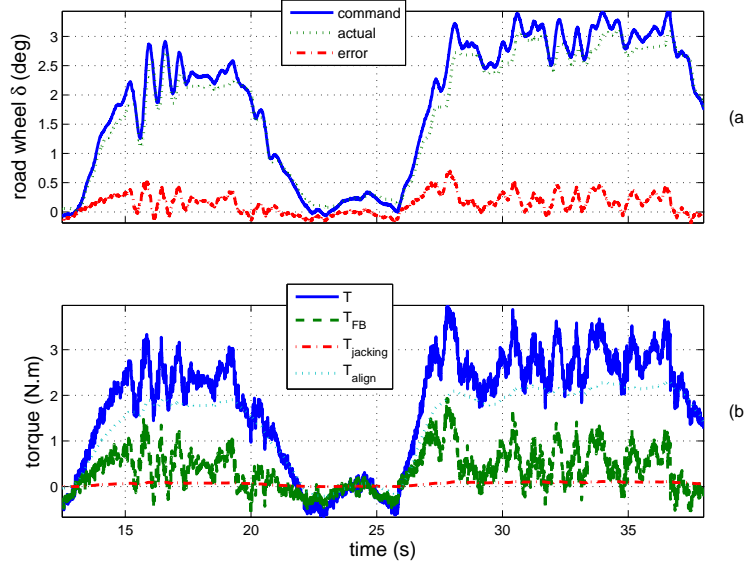


Figure B.4: Steering plots, showing a) tracking performance b) steering torque input T , steering torque feedback T_{FB} , jacking torque compensation $T_{jacking}$ and aligning moment compensation T_{align}

Figure B.4a shows the tracking performance of the low-level steering controller where the error remains within one degree, when the vehicle was driven autonomously on a paved surface with gravel on top at Santa Clara Fairground. The torque command T from the low-level steering controller, which is a combination of feedforward steering torque ($T_{jacking}$ and T_{align}) and feedback steering torque T_{FB} , is shown in Fig. B.4b.

B.2 Throttle system

The throttle by-wire system in the Audi TTS receives the throttle percentage command through CAN. The throttle command in percent is calculated from the longitudinal force command F_x (4.8) in Chapter 4, where the Audi TTS engine map is used. This engine map is found from carrying out a system identification at Bonneville Salt Flat in Utah, where different throttle percentages at different engine RPMs were used to identify the longitudinal force produced by the engine. Thus, the engine map,

where the inputs are engine RPM and F_x and the output is the throttle percentage, was found. The time delay from turbo lag was not taken into account in this engine map.

B.3 Brake system

The brake by-wire system in the Audi TTS uses a vacuum booster that comes from a vehicle with an adaptive cruise control. The brake system receives a brake pressure command, which is calculated from the longitudinal force F_x in (4.8) via a lookup table. The lookup table was found using a brake system identification at Bonneville Salt Flat in Utah, where different brake pressure commands were applied while the vehicle was coasting in neutral to identify the braking force.

B.4 Gear shift system

With the DSG (Direct-Shift Gearbox) system in the Audi TTS, the controller sends shift up or down commands through CAN to control the gear position. The controller selects the gear to ensure that the engine is operating within its power band of 3,000-6,250 RPM.

B.5 xPC target, a.k.a. “Peak Box”

The detail of how to setup the controller hardware called “Peak Box” that runs xPC [35] can be found from

<https://ddlweb.stanford.edu/vehicles/PikesPeak/TTSvehicleData/xPC> through SVN. This SVN folder contains the registered address of each PC-104 board in the xPC, the process for setting up the xPC boot disk and the process of communicating with the xPC.

Appendix C

Future Work in Details

C.1 Real-time friction estimation

An accurate real-time friction estimation can improve the accuracy of the feedforward longitudinal command. Since the desired speed profile is derived from the estimated friction value, accurate friction information will ensure that the vehicle will operate at its friction limits.

The controller can estimate the friction coefficient in real-time by observing front and rear tire slip. From the slip circle in Section 4.2, if both front and rear slip are inside the unit circle, then the vehicle is not operating at its friction limits. Thus, the controller can increment the estimated friction value by a small amount, which increases the desired speed profile. On the contrary, if the front or rear slip is outside the unit circle, then the vehicle operates beyond its friction limits. The controller can then reduce the estimated friction value by a small amount.

The controller can do this friction estimation in real-time and store the estimated friction value for each segment of the path. Since the vehicle is driven on the same path multiple times, similar to a racecar driver practicing driving around a race track, the estimated friction coefficient can converge over this time period.

Estimating the friction coefficient from tire slip is straightforward in this situation as the vehicle operates at or close to its limits; thus, the signal to noise ratio is large as the slip signal is large. The friction estimation should be active during cornering and

braking, but not during accelerating as the limited engine torque could prevent the tires from fully utilizing their friction limits. If the controller has access to an aligning moment measurement (i.e., a steering torque measurement), the method proposed by Hsu et al. [26] can be used to estimate the friction value in real-time.

C.2 Converting front lateral force to steering input

The issue of small local cornering stiffness when the front tires operates close to the friction limits is discussed in Section 6.1.4. This causes the steering input δ to change significantly even when the lateral input force F_{yf} changes by only a small amount in (6.19). This abrupt change in the steering input at the limits is undesirable when operating at the limits. To minimize this problem, future work will look into how to minimize this steering input δ when the vehicle is operating close or at the limits. One potential solution is to take into account that only minimal additional lateral force is gained when turning the road wheels at the limits. In fact, changing the direction of the tire force with a large steer angle can actually decrease the effective lateral force.

$$\delta = \frac{U_y + ar}{U_x} - \alpha_f^{des} \quad (6.19)$$

The other aspect associated with using (6.19) to convert F_{yf} to δ is that the measured lateral speed U_y and the yaw rate r can be corrupted by measurement noise, which will propagate into the steering input. The measurement noise is exacerbated at slow speed due to small denominator value of U_x in (6.19). Further improvement can be made by integrating filters into the measurement or introducing a filter at the steering output δ based on tire relaxation length. However, this resulting phase delay of the steering input could affect the performance of the steering controller.

C.3 Path modification

When a vehicle approaches a corner at an excessive speed, the vehicle will deviate from the desired path as there is not sufficient tire forces to turn the vehicle. As mentioned in Section 2.1.3, racecar drivers will modify their path to create a “recovery line” [3]. Blank et al. [4] and Klomp [41] investigated various methods of coming back to the original path, although their approach does not include redesigning a new path to follow. Currently, the controller does not have an ability to generate a recovery line and if the vehicle is entering a corner at an excessive speed, all the feedback inputs will try to bring the vehicle back to the original desired path. This may not be an optimized solution because by using a “recovery line” line, which widens the desired path, the controller may have a high chance of successfully following this alternate line without extreme steering input or excessive corrections.

One approach of creating a “recovery line” is to coordinate the longitudinal and lateral controllers via a modified slip circle controller. Currently, the longitudinal feedback controller uses the distance between the measured slip and the desired slip along the y-axis $\Delta\bar{\kappa}$, see (4.5). Consequently, the longitudinal feedback controller does not take any lateral slip (from the steering controller) into account. Instead of using $\Delta\bar{\kappa}$, if we restructure the problem by using the radial distance from the unit circle $\Delta\bar{\chi}$:

$$\begin{aligned}\bar{\chi} &= \sqrt{\bar{\alpha}^2 + \bar{\kappa}^2} \\ \Delta\bar{\chi} &= \bar{\chi} - 1 ,\end{aligned}\tag{C.1}$$

the steering input is now incorporated into this new slip circle controller. Then, we can use sliding mode control [70] to structure this problem as

$$\Delta\dot{\bar{\chi}} = -k_{sliding}\Delta\bar{\chi} + \Delta f ,\tag{C.2}$$

where $k_{sliding}$ is the feedback gain and Δf is the robust term to ensure that $\Delta\bar{\chi}$

reaches the sliding surface.

The benefit of structuring the problem as shown in (C.2) emerges when differentiating $\Delta\bar{\chi}$ in (C.1) because both lateral and longitudinal inputs appear in the equation:

$$\Delta\dot{\bar{\chi}} = \frac{1}{\sqrt{\bar{\alpha}^2 + \bar{\kappa}^2}}(\bar{\alpha}\dot{\bar{\alpha}} + \bar{\kappa}\dot{\bar{\kappa}}) = -k_{sliding}\Delta\bar{\chi} + \Delta f . \quad (\text{C.3})$$

The controller can control $\dot{\bar{\alpha}}$ through the steering input δ and $\dot{\bar{\kappa}}$ through the torque at the road wheel T . For instance, consider the term $\dot{\bar{\kappa}}$ from (4.3),

$$\begin{aligned} \dot{\bar{\kappa}} &= \frac{1}{\kappa^{ref}} \frac{d}{dt} \left(\frac{R_e \omega - V}{V} \right) \\ &= \frac{1}{\kappa^{ref}} \frac{R_e \dot{\omega} V - \dot{V} R_e \omega}{V^2} , \end{aligned} \quad (\text{C.4})$$

where $\dot{\omega}$ is controlled through the wheel dynamics with the input from the longitudinal torque at the road wheel T :

$$J\dot{\omega} = T - R_e F_x^{tire} , \quad (\text{C.5})$$

where J is the wheel inertia and F_x^{tire} is the reaction friction force acting on the tire.

Instead of modifying the steering controller to control $\dot{\bar{\alpha}}$, we can use the lanekeeping steering in Chapter 3 and modify the desired path to control $\dot{\bar{\alpha}}$. Doing so avoids the need to design a new steering controller because the stability of the lanekeeping steering system is already proven by Talvala et al. [77].

To define a “recovery line” that controls $\dot{\bar{\alpha}}$, one potential solution is to find the curvature of this “recovery line”. First the relationship between $\dot{\bar{\alpha}}$ and the steering input δ is found from vehicle kinematics, using a small angle approximation:

$$\begin{aligned} \alpha_f &= \beta + \frac{ar}{U_x} - \delta \\ \dot{\alpha}_f &= \frac{1}{\alpha_f^{ref}} \frac{d}{dt} \left(\beta + \frac{ar}{U_x} \right) - \frac{1}{\alpha_f^{ref}} \dot{\delta} , \end{aligned} \quad (\text{C.6})$$

where $\dot{\delta}$ can be found from (3.10) when the lanekeeping steering is used with a small angle approximation. Using the coordinate transformation in (6.3), the curvature of the “recovery line” appears in the equation.

$$\begin{aligned}\dot{\delta}_{control} &= -\frac{2k_p}{C_f}(\dot{e} + (a + x_{la})\Delta\dot{\psi}) \\ &= -\frac{2k_p}{C_f}(\dot{e} + (a + x_{la})(r - K\dot{s})) .\end{aligned}\tag{C.7}$$

Consequently, we can control the dynamics of $\Delta\bar{\chi}$ in (C.3) by using a combination of longitudinal and lateral inputs to control $\dot{\kappa}$ and $\dot{\alpha}$ respectively. The torque at the road wheel T controls $\dot{\kappa}$ in (C.4) while the new curvature of the “recovery line” K controls $\dot{\alpha}$ in (C.6). This provides a framework to calculate a “recovery line” when the vehicle approaches a corner at an excessive speed by coordinating lateral and longitudinal controllers.

Appendix D

Driving P1 at the limits

D.1 Preliminary work on P1

Before the controller was test on the Audi TTS in Fig. 1.2, most of the controller development was done on P1 in Fig. D.1. This section shows some of the initial development work on P1, which provides an history of the controller development. The first part of this section explain how the first controller is put together, using the steering controller in Chapter. 3 and a simple longitudinal controller to control the speed [42].



Figure D.1: Stanford P1 by-wire research vehicle

D.1.1 Speed controller

Similar to the steering controller, both feedforward and feedback speed controllers are used. Feedforward speed estimates the maximum speed that the vehicle could go through a corner, while speed feedback is introduced to imitate a racecar driver feathering the throttle or modulating the brake during cornering.

Feedforward speed controller

The feedforward speed is calculated to ensure that the vehicle operates at the limits of tire adhesion during cornering. Theoretically, this speed would result in a vehicle cornering with the maximum available lateral tire forces. This maximum lateral acceleration is estimated from the available friction. By using a steady state cornering assumption, the feedforward speed is found.

$$F_y^{maximum} = \mu mg = m \frac{U_x^2}{R} \quad (D.1)$$

$$U_x^{feedforward} = \sqrt{\mu R g} \quad (D.2)$$

Slip angle plots and “g-g” diagrams [49] are used in the experimental results section to demonstrate that the vehicle actually reached its limits of handling.

Feedback speed controller

Friction variations could potentially cause the tires to operate beyond their static peak forces, causing the tires to start sliding. Since the feedback steering controller is based on a linear tire assumption, if the front tires start sliding (understeer scenario) the lanekeeping controller commands additional steering. However, since the front tires are already saturated, additional steering does not increase the front lateral forces. Thus, speed feedback control is necessary in order to slow the vehicle down and reduce the sliding of the front tires. This is similar to a racecar driver modulating the throttle to control the vehicle understeer. Alternatively, if the vehicle could generate large driving torque to spin only the rear wheels, then the controller could also use the

throttle to turn the vehicle (throttle steer). This method has not been explored at this stage due to the limited available torque at the rear wheels on the experimental vehicle.

Two feedback parameters for the proportional speed controller were investigated, namely the lookahead error (e_{la}) and the heading error ($\Delta\psi$). From Fig. 3.2.1, the lookahead error is the combination of lateral error e and heading error as shown in (3.9).

As e_{la} is a combination of both e and $\Delta\psi$, and the objective of the feedback controller is to minimize these two values, using a proportional controller based on

$$\Delta U_x^{feedback} \propto -e_{la} \quad (D.3)$$

seems like a logical choice. Moreover, when a vehicle goes through a corner with excessive speed, e_{la} should increase and cause the controller to reduce the speed.

A speed feedback based on heading error ($\Delta\psi$) was also investigated. Since the experimental vehicle is inherently limit understeer, the heading error tends to grow when the front tires enter the nonlinear region. In this situation, the speed feedback controller will command the vehicle to slow down, which is the desired behavior.

$$\Delta U_x^{feedback} \propto -\Delta\psi \quad (D.4)$$

D.1.2 Experimental setup

The Stanford P1 by-wire research vehicle [44], shown in Fig. D.1, was used for testing on a gravel surface. The vehicle is equipped with a Differential Global Positioning System (DGPS) and inertial sensors (INS), from which vehicle position and other states can be obtained. This DGPS and INS experimental setup determines path tracking errors and is described in [66].

The vehicle tracks the desired speed (calculated from the feedforward and feedback speed commands) by controlling the motor torques, which are proportional to the

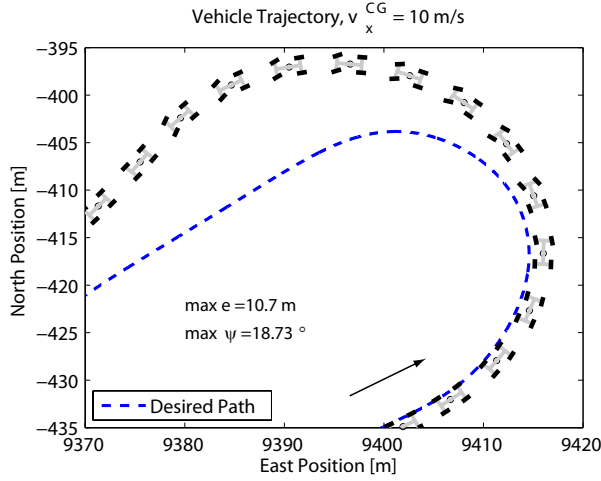


Figure D.2: Vehicle trajectory: with feedback steering only

difference between the desired speed and the vehicle speed. As the motors have regenerative braking functions, negative braking torques can be applied to the driven rear wheels.

The testing area was a large parking lot with gravel over asphalt. The inconsistent surface provided varying friction in the range of 0.4 to 0.6 and therefore presented a control challenge.

D.1.3 Experimental results

Baseline controller

Figure D.2 demonstrates the vehicle trajectory when only the lanekeeping steering feedback was used with an arbitrarily chosen constant throttle input. The lack of a suitable speed control as well as proper feedforward steering caused the vehicle to generate large tracking errors ($\max e=10.7\text{ m}$, $\max \Delta\psi=18.73^\circ$). This was expected due to the excessive speed and also because the lanekeeping steering feedback controller was designed to work with driver input, which was set to zero in this test. Without feedforward steering, the vehicle must deviate from the desired path and generate tracking errors before the lanekeeping system commands the vehicle to steer back towards the desired path. Nevertheless, the steering controller is very robust [24]

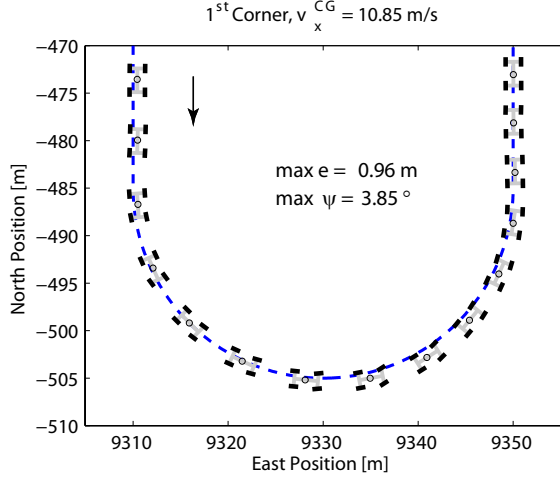


Figure D.3: Vehicle trajectory: with completed steering control and feedforward speed

and the vehicle does not lose stability.

Adding feedforward controllers

By adding feedforward steering and feedforward speed, significant reduction in tracking errors can be observed as demonstrated in Fig. D.3. The maximum lateral error was decreased from 10.7 m to less than 1 m, while the maximum heading error was decreased from 18.73° to 3.85° . These results suggest that adding the speed feedback controller could perhaps further improve the performance.

To check that P1 is operating at its limit, a plot between the front wheels slip angle and the lateral acceleration is depicted in Fig. D.4. The figure demonstrates that even though the slip angle decreases beyond -6° , the lateral acceleration reaches its plateau at 6 m/s^2 (around $0.6g$, which corresponds to $\mu = 0.6$). This indicates that increasing magnitude of the slip angle could not generate any additional lateral force and shows that the front tires are saturated (sliding). Thus demonstrating that the feedforward speed controller brings the vehicle up to its limits.

In addition, a small deviation from the desired path in Fig. D.3 and large front slip angle in Fig. D.4 indicate that the vehicle exceeds its limit for a short period of time, around the apex of the curve. As mentioned in the speed controller section, introducing a speed feedback controller should minimize the tire saturation while

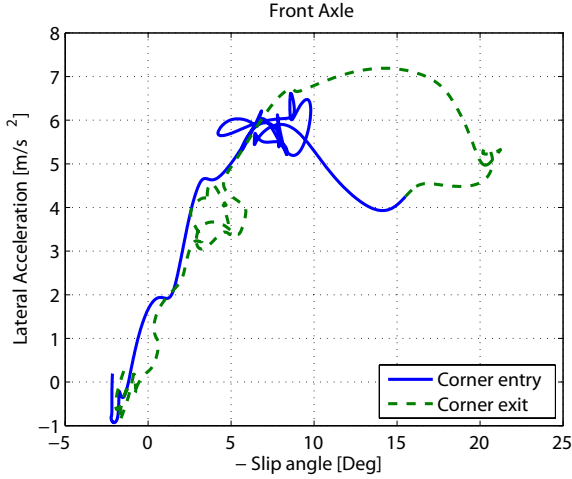


Figure D.4: Front tire slip angle: with completed steering control and feedforward speed

ensuring that the vehicle stays at its limits.

Adding lookahead error speed feedback controller

The speed feedback controller based on lookahead error (e_{la}) was added to the experiment. Figure D.5 shows that the tracking performance actually deteriorated. Furthermore, the speed feedback controller exhibited a counterintuitive behavior, as the vehicle accelerated into the corner, indicated by the grey bars next to the vehicle, and braked hard at the corner exit, indicated by the black bars. This behavior is opposite to what a racecar driver would typically do when going through a corner.

Accelerating into the corner increased understeer and caused the vehicle to deviate from the path. Yet, the lookahead error was unable to detect this understeer because the lookahead error is the combination of lateral error (e) and heading error ($\Delta\psi$). During the experiment, the heading error increased, but because the vehicle started from the inside of the path, the lateral error was negative. Combining the negative lateral error and positive heading error results in a near-zero lookahead error (3.9), demonstrating the ineffectiveness of using lookahead error as a feedback state.

In addition to the vehicle trajectory plot, a “ $g-g$ ” diagram is shown in Fig. D.6. Most of the cornering maneuver occurs on the right hand side of the “ $g-g$ ” diagram,

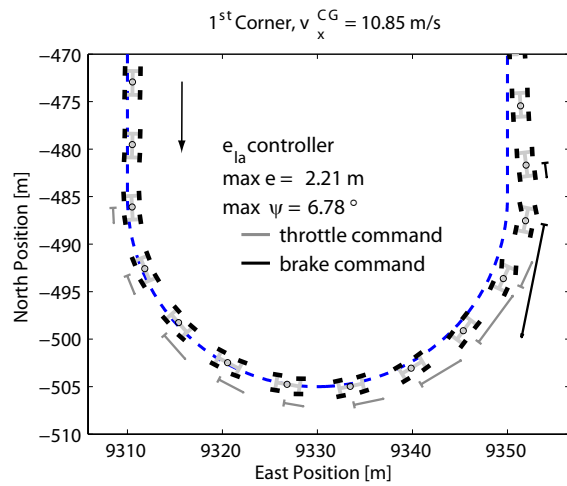


Figure D.5: vehicle trajectory: adding lookahead error speed feedback

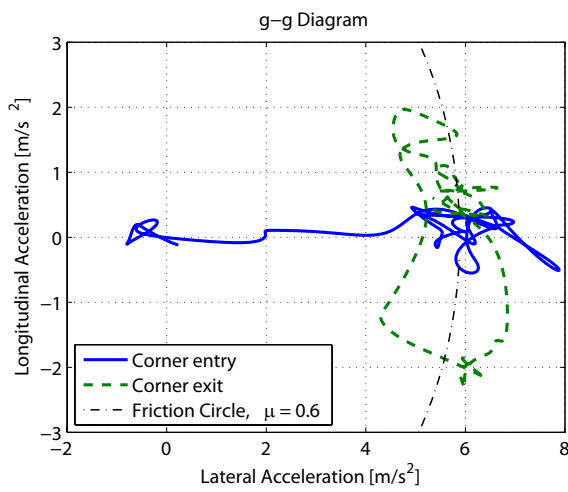


Figure D.6: “g-g” diagram: adding lookahead error speed feedback

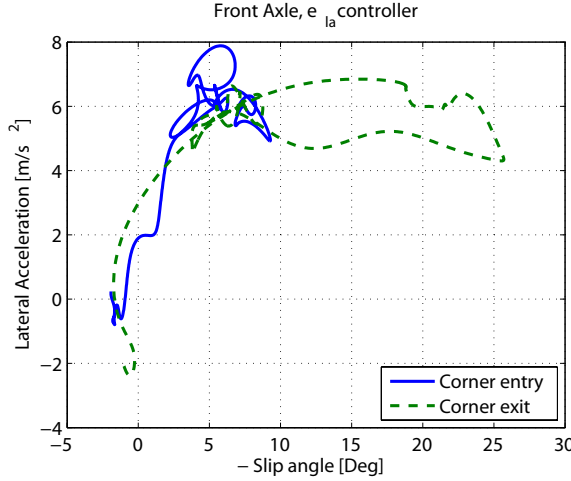


Figure D.7: Front tire slip angle: adding lookahead error speed feedback

between 4 to 8 m/s^2 . The vehicle tried to accelerate during corner entry, indicated by a small positive acceleration in the diagram. This acceleration caused the vehicle to slide out from the intended path, but the lookahead error could not observe this deviation until it was at the corner exit, where the error was already large. Consequently, the controller applied significant brake while the lateral acceleration was close to its limits, causing the front tires to saturate and start understeering. This results in the large slip angles shown in Fig. D.7, which are even larger than the slip angles of the experiment with no speed feedback controller in Fig. D.4. The trace on the “g-g” diagram also shows sudden change in the longitudinal acceleration, as it rapidly decreases to -2 m/s^2 . The abrupt change in the speed feedback command and the large front tire saturation clearly demonstrates the limitation of this controller.

Adding heading error speed feedback controller

Using heading error as a feedback state provided the best result ($\max e = 0.36 \text{ m}$, $\max \Delta\psi = 1.62^\circ$), as depicted in Fig. D.8. The $\Delta\psi$ speed feedback commands were significantly less than the e_{la} speed feedback commands in Fig. D.5, as well as less abrupt.

Furthermore, the $\Delta\psi$ speed feedback controller mimicked the behavior of a racecar driver by slowing the vehicle down during corner entry and accelerating the vehicle

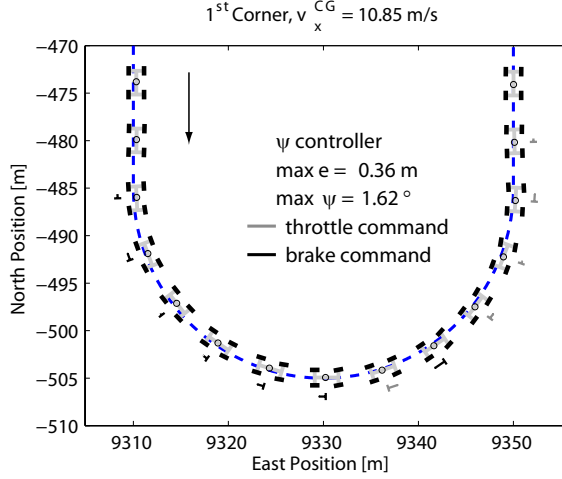


Figure D.8: Vehicle trajectory: adding heading error speed feedback

out from the turn after passing the corner apex. The brake command during corner entry reduced the vehicle understeer and allowed the vehicle to track the path with minimal error.

The $\Delta\psi$ speed controller also ensured that the vehicle stayed at its limits as most of the cornering maneuvers were concentrated around the edge of the “g-g” diagram in Fig. D.9. Moreover, the feedback controller also modulated the speed to avoid front tire saturation, as Fig. D.10 shows the smallest plateau and smallest maximum slip angle, when compared to other controllers in Fig. D.4 and D.7. In summary, the vehicle equipped with the $\Delta\psi$ speed controller has the least amount of front tire slip, and travels through the corner at its limits with the best tracking performance.

Time through the corner was roughly comparable. The vehicle with the $\Delta\psi$ controller took 7.70 s to go through the corner compared to 7.74 s with the e_{la} speed feedback controller. This difference is in the range of friction variation from the gravel surface.

From the “g-g diagram” in Fig. D.9, faster time through the corner is possible if the vehicle spends more time on the edge of the friction circle. For instance, the $\Delta\psi$ speed controller does not fully utilize the friction circle when the lateral acceleration is below 4 m/s^2 , as neither the longitudinal nor the lateral accelerations are at their limits. The “g-g” diagram suggests that the vehicle could enter the corner at a higher

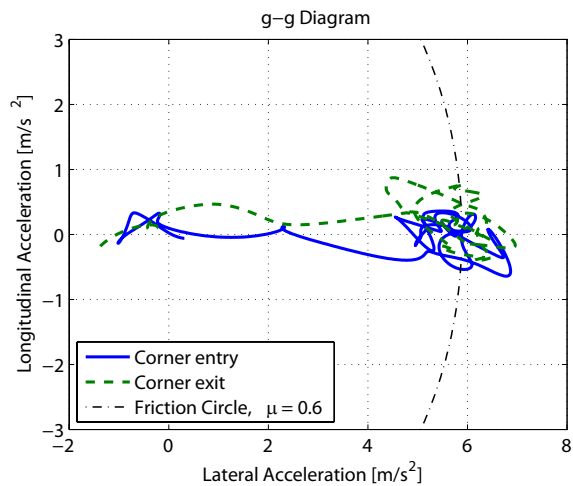


Figure D.9: “g-g” diagram: adding heading error speed feedback

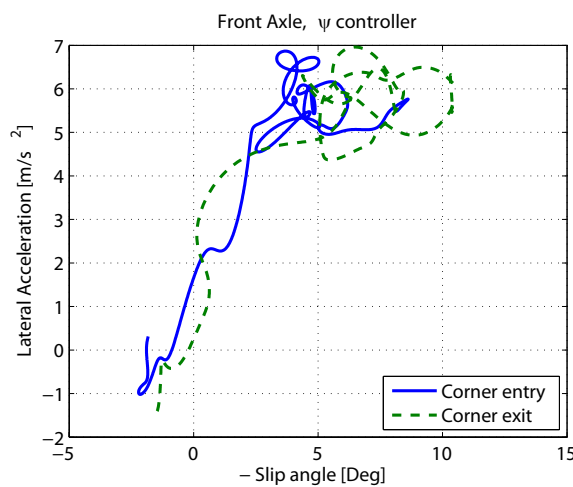


Figure D.10: Front tire slip angle: adding heading error speed feedback

Table D.1: Summary of each controller's tracking performance

Controller	Feed-forward ¹	Speed feedback	Maximum e [m]	$\Delta\psi$ [°]	time [s]
baseline	No	No	10.7	18.73	-
feedforward	Yes	No	0.96	3.85	7.90
e_{la} feedback	Yes	e_{la}	2.21	6.78	7.74
$\Delta\psi$ feedback	Yes	$\Delta\psi$	0.36	1.62	7.70

speed than the calculated feedforward speed, which was derived from the steady state assumption. The controller could then gradually trail brake from the maximum braking at the corner entry to zero braking at the apex, to trace along the edge of the friction circle in the fourth quadrant. After passing the apex, the controller could then gradually apply the throttle from zero to the maximum throttle at the corner exit, to progress along the edge of the friction circle in the first quadrant. Future work will focus on exploring a feedforward trail braking strategy during corner entry and applying throttle during corner exit.

D.1.4 Conclusions for section D.1

Table D.1 summarizes the performance of each controller. By introducing feedforward steering and feedforward speed (feedforward controller in Tab. D.1), the tracking performance significantly improved from the baseline controller that used only the steering feedback. To further reduce the tracking errors, proportional speed feedback was introduced. However, the lookahead speed feedback reduced the tracking performance due to its inability to detect vehicle understeer. By summing lateral and heading errors to calculate lookahead error in (3.9), certain vehicle states could be overlooked. As heading error can detect the inherent limit understeer of the vehicle, the $\Delta\psi$ speed feedback controller performed the best. Moreover, it also demonstrated similar behavior to a racecar driver, by modulating the throttle and brake during cornering to control the vehicle understeer.

¹For both steering and speed

In addition to vehicle trajectory plots, “*g-g*” diagrams and vehicle slip angle plots were used in the analysis. The “*g-g*” diagrams demonstrate how each controller operates at the limits, while slip angle plots indicate how much the vehicle exceeds its limits. Both of these diagrams also portray the benefit of using the $\Delta\psi$ speed feedback controller as the vehicle operated at its limits without much front tire saturation, unlike the e_{la} speed feedback controller for which a significant amount of tire saturation was observed.

This paper demonstrated that using a combination of feedforward and feedback controllers could stabilize the vehicle at its limits with good tracking performance. Nevertheless, the result from the “*g-g*” diagram suggested that a faster time through a corner is possible if the vehicle operates along the edge of the “*g - g*” diagram during cornering. As a consequence, the next logical step of this research is to introduce feedforward trail braking during corner entry and throttle during corner exit to fully utilize the vehicle’s potential.

D.2 Using a “*g-g*” diagram to design a feedforward longitudinal control for P1

In this section, P1 used the same steering controller as described in Chapter. 3 and used the feedforward longitudinal controller as explained in Chapter. 2.1.2. However, the feedback longitudinal controller is much simpler and is described in the following section.

Clothoid entry:

Furthermore, because the research vehicle available for testing uses regenerative braking, which cannot generate any braking forces lower than -1.8 m/s^2 , equation (2.9) must be modified:

$$U_x(s_{n+1}) \approx U_x(s_n) + \frac{\Delta s}{U_x(s_n)} |a_x^{regen}|$$

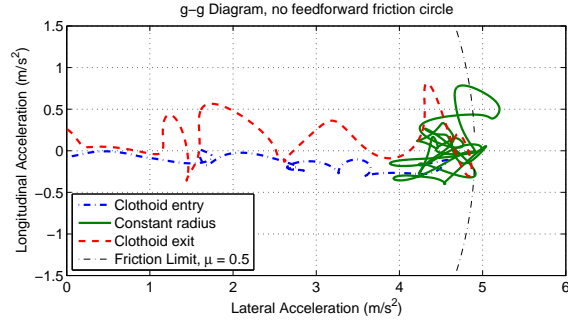


Figure D.11: “*g-g*” diagram: without trail-braking and throttle-on-exit

whenever the calculated feedforward a_x is less than the regenerative braking limit a_x^{regen} . Note that s in this case is progressing backward along the path.

D.2.1 Longitudinal feedback algorithm

The longitudinal feedback imitates racecar drivers feathering their throttle and brake during cornering to minimize tracking error and time.

The longitudinal feedback uses proportional feedback based on the absolute value of the heading error $\Delta\psi$ (see Fig. 3.2.1). Previous work showed that $\Delta\psi$ increased when the vehicle was going too fast because of the limit-understeer characteristic of the vehicle [42]. Thus, using the absolute value of $\Delta\psi$ will ensure that the feedback will command braking force whenever $\Delta\psi$ deviates from zero.

$$F_x^{feedback} \propto -|\Delta\psi| \quad (\text{D.5})$$

D.2.2 Experimental results

P1 research vehicle in Fig. D.1 is used again for this experiment. To convert from the feedforward longitudinal acceleration a_x in Section 4.1 to a motor drive torque command, a lookup table is used.

In previous work, the feedforward longitudinal command was set to maintain a

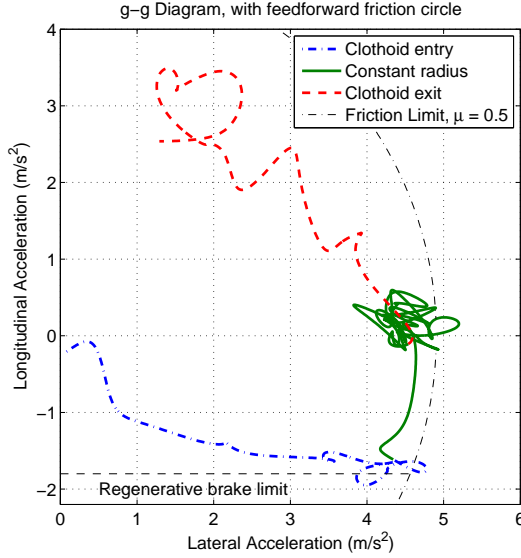


Figure D.12: “*g-g*” diagram: with trail-braking and throttle-on-exit

Table D.2: Demonstrating feedforward longitudinal controller performance

Trail-braking & throttle-on-exit	Time Duration (s)				Exit speed (m/s)
	Entry	Mid	Exit	Lap	
No	1.674	3.316	1.720	18.588	7.50
Yes	1.434	3.448	1.516	16.674	10.17

constant speed so that the car could corner at the maximum lateral acceleration. The “*g-g*” diagram of this approach is shown in Fig. D.11. As expected, the vehicle operated at its limit during the mid corner section where the curvature was constant. However, during the transient maneuvers, such as corner entry and corner exit, the results demonstrated that the vehicle did not fully utilize the available friction. Lack of feedforward trail-braking during corner entry and acceleration out from the exit prevented the vehicle from maximizing its potential.

After adding the feedforward trail-braking and throttle-on-exit described in this paper, the “*g-g*” diagram in Fig. D.12 shows a better utilization of the friction limits. The vehicle reaches the regenerative braking limit during corner entry and uses

the friction limit at the mid corner section, similar to the ideal trajectory shown in Fig. 2.1(b). During the corner exit, the vehicle accelerates out from the corner with some deviation in a_x from the friction limit. This deviation could be caused by the motors only driving the two rear wheels (not all four wheels), or because the motors are incapable of accelerating the vehicle at μg . In addition, note that the lookup table that mapped the desired a_x to the motor commands could have some error, which caused the actual a_x to deviate from the desired a_x .

A significant time improvement is observed in table D.2 when feedforward trail-braking and throttle-on-exit are added. When analyzing each section of the corner, considerable time improvement from maximizing the acceleration can be observed during the entry and exit sections. Note that when using feedforward trail-braking and throttle-on-exit, the section time in the mid corner is slower by a small amount, which could be caused by friction variation from the gravel surface. Another critical aspect that affects the lap time is the corner exit speed. When using throttle-on-exit, a much faster exit speed was achieved. This significantly reduces the time of the following straight section.

To understand how the controller operates, the results from each corner section are analyzed.

Clothoid Entry: As shown in Fig. D.13, during 27.6-29 s, the vehicle is trail-braking into a corner while increasing the steering angle. The speed of the vehicle U_x reduces while the yaw rate, front slip angle, and rear slip angle increase simultaneously. Notice that the -0.9 Volt of the longitudinal command corresponds to the regenerative braking limit of -1.8 m/s^2 .

Furthermore, notice that in Fig. D.12, the vehicle did not enter the corner with full braking (point A in Fig. 2.1(b)). Although the feedforward longitudinal controller commanded large braking at the beginning of the corner entry, there was a delay in the regenerative system. Full braking was not achieved until after 28 s. Hence, the vehicle was cornering at a speed higher than the desired speed $U_x(s)$. Moreover, even though the feedforward longitudinal controller was supposed to command zero braking at the end of corner entry (point B in Fig. 2.1(b)), there was a delay between the longitudinal command and the actual torque at the road wheels. Consequently, the trace of the

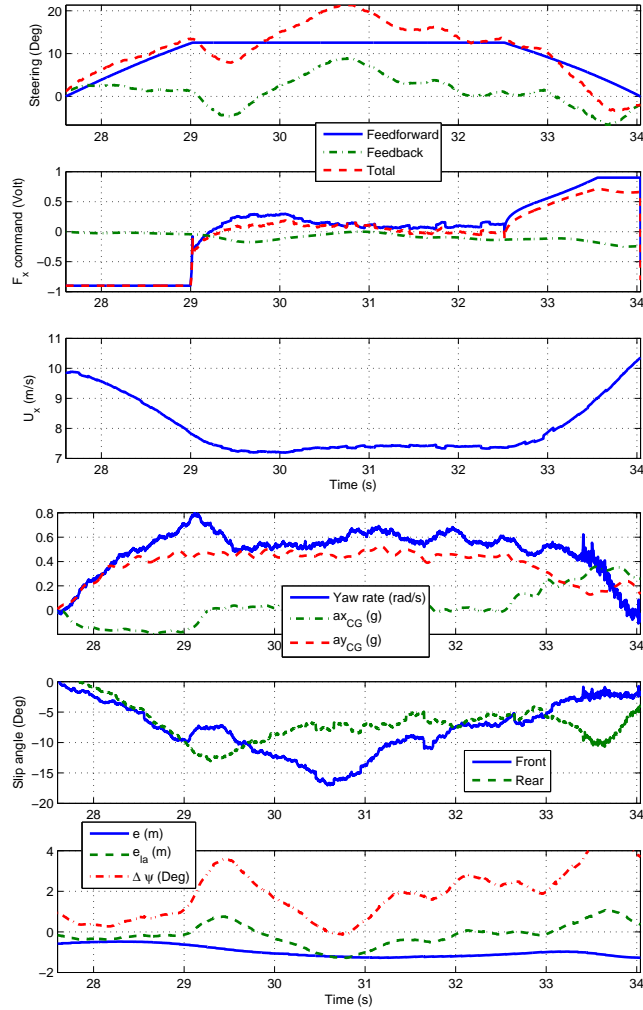


Figure D.13: Plots of input commands and vehicle states

clothoid entry in Fig. D.12 did not end with zero longitudinal acceleration.

Constant Radius: Between 29-32.5 s, the feedforward longitudinal controller tried to track a constant speed of $\sqrt{\mu R(0)g}$. As the vehicle entered the mid section with excessive speed, the longitudinal controller commanded braking while cornering and as a result, the plot traces the circle to the maximum a_y point. In order to trace the circle, all four tires have to operate at their friction limits. This means that some of the tires are sliding, as indicated by the axle slip angles plot in Fig. D.13. After the vehicle tracked the desired speed and a_x became zero, the maneuver was concentrated at the maximum cornering a_y , as expected.

At around 29 s, the vehicle starts to oversteer because the regenerative braking was only applied to the rear wheels. The lanekeeping steering reacted by counter steering, which promptly reduced the front slip angle and the yaw rate, while the rear slip angle slowly decreased through the vehicle dynamics. Between 29.7-30.7 s, the front slip angle grows, demonstrating that the vehicle starts to understeer. Note that in this case, the heading error ($\Delta\psi$) actually reduces; thus, the longitudinal feedback based on $\Delta\psi$ did not try to slow the vehicle down. As the front tires saturated, lanekeeping steering could not generate any additional force at the front wheels to pull the vehicle back to the path and to reduce the lateral error e .

Clothoid Exit: During 32.5-34 s, the feedforward longitudinal controller applied throttle during corner exit. The rear slip angle increases because a large amount of longitudinal force was commanded to the rear wheels. The vehicle starts to oversteer and causes $\Delta\psi$ to increase. Longitudinal feedback based on $\Delta\psi$ detects this and commands the vehicle to slow down. It is also interesting to point out that the vehicle exited the corner while still generating lateral acceleration. Although this may lead to some tracking error, it could be beneficial not to let off the throttle to achieve faster time.

Although there is a noticeable lateral error (e) in Fig. D.13, it must be noted that the objective of the lanekeeping steering feedback is to minimize the lookahead error (e_{la}), see equation (3.11). Better tracking performance in e can be achieved by incorporating tire saturation into the feedforward steering command and by minimizing tires sliding through a better longitudinal feedback controller.

The results demonstrate that the feedforward longitudinal controller tries to utilize the friction force from the tires. Because the feedforward calculation is based on the assumption that all four tires are operating at their friction limits, in practice, this occasionally results in some of the tires sliding. Thus, the controller relies on a good longitudinal feedback to ensure that there is no excessive slip on each tire. Although using a simple heading error ($\Delta\psi$) as a state for longitudinal feedback works well when there is no significant change in the vehicle speed, the result in the mid corner section indicates that $\Delta\psi$ could not detect that the front tires were sliding. Thus, future work will involve more complex longitudinal feedback based on a slip circle. With this new approach, the longitudinal feedback will always try to push the tires to the limits without exceeding them. Operating the front tires within their limits will prevent the front tires from sliding. Consequently, this will ensure that the lanekeeping system has control authority via the front tires, which should result in better tracking performance. In addition, the authors will start exploring the tradeoff between minimizing the tracking error and time.

D.2.3 Conclusion for section D.2

By incorporating feedforward trail-braking and throttle-on-exit into the longitudinal controller, the results showed a better lap time as well as a faster corner exit speed. Plotting the vehicle's acceleration on a “ g - g ” diagram demonstrated that the acceleration traced the acceleration limit circle. Further refinement will involve testing the same algorithm on a different vehicle to investigate the effects of actuator limitations. Experimental results also indicated a limitation of using the heading error as a state for the longitudinal feedback. Thus, future work will involve designing a longitudinal feedback controller based on a slip circle that will work efficiently with the feedforward trail-braking and throttle-on-exit.

Bibliography

- [1] AASHTO. *AASHTO Green Book: A Policy on Geometric Design of Highways and Streets*. American Association of State Highway and Transportation Officials, 444 North Capitol Street, N.W., Suite 249, Washington, D.C. 20001, 5th edition, 2004.
- [2] Ilya Baran, Jaakko Lehtinen, and Jovan Popovi. Sketching clothoid splines using shortest paths. *Computer Graphics Forum*, 29(2):655–664, May 2010.
- [3] Ross Bentley. *Speed Secrets: Professional Race Driving Techniques*. Number ISBN-10: 0760305188. Motorbooks; 1st edition, Wisconsin, USA, 1998.
- [4] Matthew Blank and Donald Margolis. Minimizing the path radius of curvature for collision avoidance. *Vehicle System Dynamics*, 33:183–201, 2000.
- [5] Carrie G. Bobier and J. Christian Gerdes. Envelope control: Stabilizing within the limits of handling using a sliding surface. *Proceedings of the International Federation of Automatic Control (IFAC) Symposium on Advances in Automotive Control, Munich, Germany*, 2010.
- [6] F. Braghin, F. Cheli, S. Melzi, and E. Sabbioni. Race driver model. *Computers & Structures*, 86:1503 – 1516, 2008.
- [7] D L Brayshaw and M F Harrison. A quasi steady state approach to race car lap simulation in order to understand the effects of racing line and centre of gravity location. *Proceedings of the Institution of Mechanical Engineers, Part D: Journal of Automobile Engineering*, 219(6):725–739, June 1 2005.

- [8] Luigi Cardamone, Daniele Loiacono, Pier Luca Lanzi, and Alessandro Pietro Bardelli. Searching for the optimal racing line using genetic algorithms. *Computational Intelligence and Games (CIG), 2010 IEEE Symposium on*, pages 388–394, August 2010.
- [9] D. Casanova, R.S. Sharp, and P. Symonds. Minimum time manoeuvring: The significance of yaw inertia. *Vehicle System Dynamics*, 34(2):77–115, 2000.
- [10] National Automated Highway System Consortium. National automated highway system consortium technical feasibility demonstration summary report. Technical report, 1998.
- [11] Jennifer N. Dang. Statistical analysis of the effectiveness of electronic stability control (esc) systems final report. Technical report, NHTSA, July 2007. DOT HS 810 794.
- [12] Ernest D. Dickmanns. Vehicles capable of dynamic vision. *Proceedings of the Fifteenth International Joint Conference on Artificial Intelligence*, pages 1577–1592, August 1997.
- [13] Paolo Falcone, Francesco Borrelli, Eric Tseng, and Davor Hrovat. On low complexity predictive approaches to control of autonomous vehicles. In Luigi del Re, Frank Allgöwer, Luigi Glielmo, Carlos Guardiola, and Ilya Kolmanovsky, editors, *Automotive Model Predictive Control*, volume 402 of *Lecture Notes in Control and Information Sciences*, pages 195–210. Springer Berlin / Heidelberg, 2010.
- [14] Gene F. Franklin, J. David Powell, and Abbas Emami-Naeini. *Feedback Control of Dynamic Systems*. Pearson Prentice Hall, 5th edition edition, 2005.
- [15] Marco Gadola, David Vetturi, Danilo Cambiaghi, and Luca Manzo. A tool for lap time simulation. *SAE Technical Papers*, (962529):153–157, 1996.
- [16] Matthias Gerdts, Simon Karrenberg, Bernhard Mueller-Bessler, and Gregor Stock. Generating locally optimal trajectories for an automatically driven car. *Optimization and Engineering*, 10(4):439–463, 2009.

- [17] Thomas D. Gillespie. *Fundamentals of Vehicle Dynamics*. Society of Automotive Engineers, Inc, 1992. SAE Order No. R-114.
- [18] T J Gordon, M C Best, and P J Dixon. An automated driver based on convergent vector fields. *Proceedings of the Institution of Mechanical Engineers, Part D: Journal of Automobile Engineering*, 216(4):329–347, 2002.
- [19] Yoshimasa Goto and Anthony Stentz. Mobile robot navigation: The cmu system. *IEEE Expert*, 2(4):44–54, January 1987.
- [20] Alfred Gray. *Modern differential geometry of curves and surfaces with Mathematics*, 2nd ed. CRC Press, Boca Raton, Florida, USA, 1997.
- [21] Jürgen Guldner, Wolfgang Sienel, Han-Shue Tan, Jürgen Ackermann, Satyajit Patwardhan, and Tilman Bünte. Robust automatic steering control for look-down reference systems with front and rear sensors. *Control Systems Technology, IEEE Transactions on*, 7(1):2–11, January 1999.
- [22] Jürgen Guldner, Han-Shue Tan, and Satyajit Patwardhan. Analysis of automatic steering control for highway vehicles with look-down lateral reference systems. *Vehicle System Dynamics*, 26:243–269, 1996.
- [23] Gary J. Heydinger, Ronald A. Bixel, W. Riley Garrott, Michael Pyne, J. Gavin Howe, and Dennis A. Guenther. Measured vehicle inertial parameters-NHTSA’s data through November 1998. *SAE World Congress*, (1999-01-1336), 1999.
- [24] Rami Y. Hindiyeh, Kirstin L. R. Talvala, and J. Christian Gerdes. Lanekeeping at the handling limits. International Symposium on Advanced Vehicle Control (AVEC), Kobe, Japan, 2008.
- [25] Pushkar Hingwe and Masayoshi Tomizuka. Experimental evaluation of a chatter free sliding mode control for lateral control in ahs. pages 3365–3369. Proceeding of the American Control Conference, Albuquerque, New Mexico, June 1997.

- [26] Yung-Hsiang Judy Hsu, Shad M. Laws, and J. Christian Gerdes. Estimation of tire slip angle and friction limits using steering torque. *IEEE Transactions of Control Systems Technology*, 18(4):896–907, July 2010.
- [27] <http://archive.darpa.mil/grandchallenge04/>.
- [28] <http://archive.darpa.mil/grandchallenge05/>.
- [29] <http://archive.darpa.mil/grandchallenge/index.asp>.
- [30] <http://director.usacracing.com/ppihc/files/pdfs/map.pdf>.
- [31] http://wardsauto.com/ar/world_vehicle_population_110815/.
- [32] <http://www.mathworks.com/help/toolbox/control/ref/lqr.html>.
- [33] <http://www.mathworks.com/help/toolbox/control/ref/sisotool.html>.
- [34] <http://www.mathworks.com/help/toolbox/robust/ref/feasp.html>.
- [35] <http://www.mathworks.com/products/xpctarget/>.
- [36] <http://www.nissan global.com/EN/TECHNOLOGY/OVERVIEW/ldp.html>.
- [37] <http://www.path.berkeley.edu/>.
- [38] <http://www.path.berkeley.edu/nahsc/>.
- [39] Prasanth Jeevan, Frank Harchut, Bernhard Mueller-Bessler, and Burkard Huhnke. Realizing autonomous valet parking with automotive grade sensors. *Intelligent Robots and Systems (IROS), 2010 IEEE/RSJ International Conference on*, ISSN: 2153-0858(11689410):3824 – 3829, December 2010.
- [40] Alan Jeffrey and Hui-Hui Dai. *Handbook of Mathematical Formulas and Integrals*. Academic Press, 30 Corporate Drive, Suite 400, Burlington, MA 01803, USA, 4th edition, 2008.

- [41] Matthijs Klomp. *Longitudinal Force Distribution and Road Vehicle Handling*. PhD thesis, Department of Applied Mechanics, Chalmers University of Technology, Gothenburg, Sweden, 2010.
- [42] Krisada Kritayakirana and J. Christian Gerdes. Controlling an autonomous racing vehicle: Using feedforward and feedback to control steering and speed. ASME 2009 Dynamic Systems and Control Conference, 2009.
- [43] Krisada Kritayakirana and J. Christian Gerdes. Autonomous cornering at the limits: Maximizing a “g-g” diagram by using feedforward trail-braking and throttle-on-exit. IFAC Symposium Advances in Automotive Control, July 2010.
- [44] S. Laws, C. Gadda, S. Kohn, P. Yih, J. C. Gerdes, and J. C. Milroy. Steer-by-wire suspension and steering design for controllability and observability. In *IFAC World Congress, Prague, Czech Republic*, 2005.
- [45] Carl Lopez. *Going Faster! Mastering the Art of Race Driving*. Bentley Publishers, Bentley Publishers, Robert Bentley, Inc., 1734 Massachusetts Avenue, Cambridge, MA 02138-1804 USA, 2001.
- [46] Markus Maurer and E. D. Dickmanns. Advanced control architecture for autonomous vehicles. *Advanced control architecture for autonomous vehicles, Proc. SPIE 3087*, (94), 1997.
- [47] Markus Maurer and E. D. Dickmanns. A system architecture for autonomous visual road vehicle guidance. *Intelligent Transportation System, 1997. ITSC '97., IEEE Conference on*, pages 578 –583, November 1997.
- [48] David R. McLellan, Joseph P. Ryan, Edmund S. Browaiski, and John W. Heinrichy. Increasing the safe driving envelope - abs, traction control and beyond. In *Vehicle Electronics Meeting Society's Needs: Energy, Environment, Safety: Proceedings of the 1992 International Congress on Transportation Electronics*, pages 103-124, SAE 92C014, Warrendale, PA, USA, October 1992. Society of Automotive Engineers, Inc.

- [49] William F. Milliken and Douglas L. Milliken. *Race Car Vehicle Dynamics*, pages 345–359. SAE International, 400 Commonwealth Drive, Warrendale, PA 15096-0001 U.S.A., 1995.
- [50] William F. Milliken and Douglas L. Milliken. *Chassis Design: Principles and Analysis*. Society of Automotive Engineers, Warrendale, PA USA, 2002.
- [51] Bill Mitchell. Driving simulator. <http://www.mitchellsoftware.com/Driving%20Simulator.htm>.
- [52] William C. Mitchell. The line king. *Racecar Engineering V14 N3*, 14(3):56–62, 2004.
- [53] Wm. C. Mitchell, Roger Schroer, and Dennis B. Grisez. Driving the traction circle. *SAE*, (2004-01-3545), 2004.
- [54] Paul Mitiguy. *Advanced Dynamics for Mechanical, Aerospace, and Biomechanical Engineers*. 2007.
- [55] Michael Montemerlo, Jan Becker, Suhrid Bhat, Hendrik Dahlkamp, Dmitri Dolgov, Scott Ettinger, Dirk Haehnel, Tim Hilden, Gabe Hoffmann, Burkhard Huhnke, Doug Johnston, Stefan Klumpp, Dirk Langer, Anthony Levandowski, Jesse Levinson, Julien Marcil, David Orenstein, Johannes Paefgen, Isaac Penny, Anna Petrovskaya, Mike Pflueger, Ganymed Stanek, David Stavens, Antone Vogt, and Sebastian Thrun. Junior: The stanford entry in the urban challenge. *Journal of Field Robotics*, 25(9):569597, 2008.
- [56] Bernhard Mueller-Bessler, Gregor Stock, and Juergen Hoffmann. Customer oriented safety and handling evaluation via adjusted driver model using real vehicle. *ATZonline*, (F2008-12-014):1–8, 2008.
- [57] Martin Mühlmeier and Norbert Müller. Optimization of the driving line on a race track. *SAE Technical Paper Series*, (2002-01-3339):1–16, 2002.
- [58] Bernhard Müller-Beßler, Roman Henze, and Ferit Kucukay. Reproducible transverse dynamics vehicle evaluation in the double lane change. *ATZ worldwide*, 110(ATZ 0412008):44–49, 2008.

- [59] U.S. Department of Transportation National Highway Traffic Safety Administration. *Traffic Safety Facts 2009, A Compilation of Motor Vehicle Crash Data from the Fatality Analysis Reporting System and the General Estimates System*. Number DOT HS 811 402. 2011.
- [60] Hans B. Pacejka. *Tire and Vehicle Dynamics*. Society of Automotive Engineers, Inc, 400 Commonwealth Dr. Warrendale, PA 15096-0001, 2002.
- [61] Steven C. Peters, Emilio Frazzoli, and Karl Iagnemma. Differential flatness of a front-steered vehicle with tire force control. *IEEE/RSJ International Conference on Intelligent Robots and Systems, San Francisco, California, September 2011*, 2011.
- [62] Hung Pham, Karl Hedrick, and Masayoshi Tomizuka. Combined lateral and longitudinal control of vehicles for ivhs. Number TA1 - 10:20, pages 1205–1206. Proceedings of the American Control Conference, Baltimore, Maryland, June 1994.
- [63] Günther Prokop. Modeling human vehicle driving by model predictive online optimization. *Vehicle System Dynamics*, 35(1):19–53, 2001.
- [64] R. S. Rice. Measuring car-driver interaction with the g-g diagram. *Society of Automotive Engineers, Warrendale, PA*, (730018):1–19, 1973.
- [65] E. J. Rossetter. *A Potential Field Framework for Active Vehicle Lanekeeping Assistance*. PhD thesis, Stanford University, Stanford, California, USA, 2003.
- [66] E. J. Rossetter, J. P. Switkes, and J. C. Gerdes. Experimental validation of the potential field lanekeeping system. *International Journal of Automotive Technology*, 5(2):95–108, 2004.
- [67] Dieterich J. Schuring, Wolfgang Pelz, and Marion G. Pottinger. A model for combined tire cornering and braking forces. *SAE Technical Paper Series*, (960180):61–73, 1996.

- [68] R S Sharp, D Casanova, and P Symonds. A mathematical model for driver steering control, with design,tuning and performance results. *Vehicle System Dynamics*, 33(5):289–326, 2000.
- [69] Dong Hun Shin and Sanjiv Singh. Path generation for robot vehicles using composite clothoid segments. Technical Report CMU-RI-TR-90-31, Robotics Institute, Carnegie Mellon University, Pittsburgh, PA, December 1990.
- [70] Jean-Jacques E. Slotine and Weiping Li. *Applied nonlinear control*. Prentice-Hall, 1991.
- [71] Carroll Smith. *Drive to Win: The Essential Guide to Race Driving*. SAE International; First Edition edition, 1996.
- [72] Joshua P. Switkes. *Handwheel Force Feedback with Lanekeeping Assistance: Combined Dynamics, Stability and Bounding*. PhD thesis, Stanford University, Stanford, California, USA, 2006.
- [73] Joshua P. Switkes and J. Christian Gerdes. Guaranteeing lanekeeping performance with tire saturation using computed polynomial lyapunov functions. *Proceedings of IMECE2005, ASME International Mechanical Engineering Congress and Exposition, Orlando, Florida, USA, 2005*, 2005.
- [74] Joshua P. Switkes, Eric J. Rossetter, Ian A. Coe, and J. Christian Gerdes. Handwheel force feedback for lanekeeping assistance: Combined dynamics and stability. *Journal of Dynamic Systems, Measurement, and Control*, 128(3):532–542, September 2006.
- [75] Junya Takahashi, Makoto Yamakado, Shinjiro Saito, and Atsushi Yokoyama. A new hybrid stability-control system with understeer-prevention control based on g-vectoring concept. pages 867–872. 10th International Symposium on Advanced Vehicle Control, 2010.
- [76] Kirstin L. R. Talvala and J. Christian Gerdes. Lanekeeping at the limits of handling: Stability via lyapunov functions and a comparison with stability control. *ASME Conference Proceedings*, 2008(43352):361–368, 2008.

- [77] Kirstin L. R. Talvala, Krisada Kritayakirana, and J. Christian Gerdès. Pushing the limits: From lanekeeping to autonomous racing. *Annual Reviews in Control*, 35(1):137–148, April 2011.
- [78] Piero Taruffi. *The Technique of Motor Racing*. Robert Bentley, Inc, Cambridge MA 02138-1804 USA, 1959.
- [79] Paul A. Theodosis and J. Christian Gerdès. Generating a racing line for an autonomous racecar using professional driving techniques. *4th Annual Dynamic Systems and Control Conference*, 2011. Arlington, VA, USA.
- [80] M. Thommyppillai, S. Evangelou, and R. S. Sharp. Car driving at the limit by adaptive linear optimal preview control. *Vehicle System Dynamics*, 47(12):1535 – 1550, December 2009.
- [81] Mark Thommyppillai, S. Evangelou, and Robin S. Sharp. Advances in the development of a virtual car driver. *Multibody System Dynamics*, 22:245–267, 2009. 10.1007/s11044-009-9164-4.
- [82] Sebastian Thrun. What we’re driving at. <http://googleblog.blogspot.com/2010/10/what-were-driving-at.html>, 2010.
- [83] Sebastian Thrun, Mike Montemerlo, Hendrik Dahlkamp, David Stavens, Andrei Aron, James Diebel, Philip Fong, John Gale, Morgan Halpenny, Gabriel Hoffmann, Kenny Lau, Celia Oakley, Mark Palatucci, Vaughan Pratt, Pascal Stang, Sven Strohband, Cedric Dupont, Lars-Erik Jendrossek, Christian Koenen, Charles Markey, Carlo Rummel, Joe van Niekerk, Eric Jensen, Philippe Alessandrini, Gary Bradski, Bob Davies, Scott Ettinger, Adrian Kaehler, Ara Nefian, and Pamela Mahoney. Stanley: The robot that won the DARPA Grand Challenge. *Journal of Field Robotics*, 23(9):661–692, 2006.
- [84] Julian P. Timings and David J. Cole. Minimum manoeuvre time of a nonlinear vehicle at constant forward speed using convex optimisation. *Proc 10th International Symposium on Advanced Vehicle Control, AVEC 2010, Loughborough, August 2010*, pages 1–6, 2010.

- [85] Julian P. Timings and David J. Cole. Efficient minimum manoeuvre time optimisation of an oversteering vehicle at constant forward speed. *2011 American Control Conference, San Francisco, CA, USA*, pages 5267–5272, 2011.
- [86] H. E. Tseng, J. Asgari, D. Hrovat, P. van der Jagt, A. Cherry, and S. Neads. Evasive manoeuvres with a steering robot. *Vehicle System Dynamics*, 43(3):199–216, March 2005.
- [87] Christopher Urmson, Joshua Anhalt, J. Andrew (Drew) Bagnell, Christopher R. Baker, Robert E. Bittner, John M. Dolan, David Duggins, David Ferguson, Tugrul Galatali, Hartmut Geyer, Michele Gittleman, Sam Harbaugh, Martial Hebert, Thomas Howard, Alonzo Kelly, David Kohanbash, Maxim Likhachev, Nick Miller, Kevin Peterson, Raj Rajkumar, Paul Rybski, Bryan Salesky, Sebastian Scherer, Young-Woo Seo, Reid Simmons, Sanjiv Singh, Jarrod M. Snider, Anthony (Tony) Stentz, William (Red) L. Whittaker, and Jason Ziglar. Tartan racing: A multi-modal approach to the darpa urban challenge. Technical Report CMU-RI-TR-, Robotics Institute, Carnegie Mellon University, April 2007.
- [88] Anton van Zanten. Evolution of electronic control systems for improving vehicle dynamic behavior. 2002.
- [89] Anton T. van Zanten, Rainer Erhardt, Georg Pfaff, Friedrich Kost, Uwe Hartmann, and Thomas Ehret. Control aspects of the Bosch-VDC. In *International Symposium on Advanced Vehicle Control (AVEC), Aachen University of Technology, Germany*, pages 573–608, 1996.
- [90] E. Velenis, P. Tsiotras, and J. Lu. Optimality properties and driver input parameterization for trail-braking cornering. *European Journal of Control*, 14(4):308–320, July-August 2008.
- [91] Efstathios Velenis and Panagoitis Tsiotras. Minimum-time travel for a vehicle with acceleration limits: Theoretical analysis and receding-horizon implementation. *Journal of Optimization Theory and Applications*, 138(2):275–296, 2008.

- [92] Efstathios Velenis, Panagoitis Tsiotras, and Jianbo Lu. Modeling aggressive maneuvers on loose surfaces: The cases of trail-braking and pendulum-turn. In *European Control Conference, Kos, Greece, July 2-5, 2007*. European Control Conference, July 2007.
- [93] Dr.-Ing. Peter Waldmann and Dipl.-Ing. Daniel Niehues. Der BMW Track-Trainer - automatisiertes Fahren im Grenzbereich auf der Nürburgring Nordschleife. *Tagung aktive Sicherheit, Lehrstuhl für Fahrzeugtechnik, Technische Universität München*, 2010.
- [94] D.J. Walton and D.S. Meek. A controlled clothoid spline. *Computers & Graphics*, 29:353–363, 2005.
- [95] Chieh-Chih Wang, Charles Thorpe, and Sebastian Thrun. Online simultaneous localization and mapping with detection and tracking of moving objects: theory and results from a ground vehicle in crowded urban areas. *Robotics and Automation, 2003. Proceedings. ICRA '03. IEEE International Conference on*, 1:842–849, September 2003.
- [96] M. Yamakado and M. Abe. An experimentally confirmed driver longitudinal acceleration control model combined with vehicle lateral motion. *Vehicle System Dynamics*, 46:129–149, 2008.
- [97] Erik Zapletal. Trail blazing. *Racecar Engineering V14 N8*, 14(8):54–62, August 2004.